Università degli Studi di Padova

DIPARTIMENTO DI INGEGNERIA INDUSTRIALE
Corso di Laurea Magistrale in Ingegneria Aerospaziale

Tesi di laurea magistrale

Numerical investigation of aerodynamic effects of distributed propulsion

Laureando:
Pierpaolo Toniato
1043585

Relatore:
Prof. Ernesto Benini

Correlatore:
Olivier Atinault

Anno Accademico 2013–2014

ACKNOWLEDGEMENTS

CONTENTS

LIST OF FIGURES

LIST OF TABLES

ABSTRACT

Large jet-powered transport aircraft have been designed till nowadays by placing thrust engines either under wings or on the fuselage to minimize aerodynamic interactions. However, advances in simulation tools and new technologies for materials are enabling a high degree of integration between the airframe and propulsion system.

The concept of distributed propulsion is to integrate the propulsion system with the airframe to exploit synergies and coupling effects of such a configuration.

This report describes a CFD study of the aerodynamic effect of distributed propulsion. As a first step, a preliminary design model is established and studied. Several configurations of 2D model of distributed propulsion have been analyzed, using a new kind of boundary condition to model the engine. A comparison has been done to evaluate and identify key aspects of each configuration. Finally a 3D model of an aircraft equipped with a distributed system is studied, and compared to 2D studies.

INTRODUCTION

This is the final report of the internship concerning "Aerodynamic effects of the distributed propulsion" performed at Onera, that has been done under the supervision of Olivier Atinault,research eng. Applied Aerodynamics department. The structure of the report is as follow:

IN THE FIRST CHAPTER we will introduce "distributed propulsion", its possible interests and the objective of this work.

IN THE SECOND CHAPTER we will carry out a preliminary analysis (0-D model) that will serve as a base for the subsequent CFD analysis.

THE THIRD CHAPTER will introduce the four 2D-models that we have studied, along with the study and critical discussion of the boundary condition that has been used to model the propulsive system in all configurations

IN THE FOUR CHAPTER we will present the results of the CFD analysis of the different configurations, and relative discussion.

IN THE LAST CHAPTER we will study a 3D-model of a futurist aircraft and present briefly the result that we obtained.

1

THE DISTRIBUTED PROPULSION

In this chapter we will introduce the main aspects of the distributed propulsion and its possible advantages, also, I will briefly introduce the objective of this work.

1.1 AN OVERVIEW OF DISTRIBUTED PROPULSION

The European Union has proposed an array of emission goals to be implemented by the year 2050 under the "Flighpath 2050" agenda. This program aims to stipulate a reduction of 90 % in NO_x emission and 75 % in CO_2 emission, relative to capabilities of typical aircraft in-service during year the 2000.

These objectives are very ambitious considering the current technologies: to meet these goals drastic changes in propulsion and airframe systems are required. New engine technologies, system architectures and engine/airframe integrations need to be investigated and proposed.

To be more specific,the proposed concept is the so-called "distributed propulsion". It can be explained as follows: instead of increasing the size of the engines to achieve better performance, it could be possible to imagine a propulsion system made up of small engines, which could be -for example- distributed along the wing of the aircraft. This break up of the classical separation of airframe and engine could exploit possible synergy effects by coupling the propulsion jet flow with airframe. Such effects may cover aerodynamics (reduction of flow dissipation by wake filling, reduction of wetted area), propulsion system aspects (boundary layer injection) and structural improvements.

This concept is also supported by the current foreseen performance of electric components which may enable real benefits for power system hybridization or complete electrification.

However, the definition of a distributed propulsion system for aircraft is not clear (i.e., any aircraft with more than one propulsor could be classified as such) following Hyun Dae Kim, 2010 we adopt the following definition:

Distributed propulsion in aircraft application is the span-wise distribution of the propulsive net thrust stream such that overall vehicle benefits in terms of aerodynamics, propulsive, structural and/or other efficiencies are mutually maximized to enhance the vehicle mission.

Considering this description, different concepts of distributed propulsion have been proposed:

1. Jet flaps (blowing engine exhaust gas out of the wing trailing edge)

2. Cross-flow fan (2D propulsor integrated within the wing trailing edge)

3. Distributed multi-fans driven by a limited number of engines cores

4. Multiple discrete engines (driven by their own power source)

1

1.2 BENEFITS OF DISTRIBUTED PROPULSION

There are several aspects related to the use of distributed propulsion that could improve aircraft performance and reduce noise. They have been detected through recent research (see Hyun Dae Kim, 2010):

- Better integration of the propulsion system with the airframe for noise reduction through airframe shielding

- Reduction of installation weight through engine/nacelle structure integration

- Possible elimination of aircraft control surfaces through differential and vectoring thrust for pitch, roll and yaw moments

- High production rates and easy replacement of engines or propulsor that are small and light

- Increased propulsive efficiency through filling in the wake generated by the airframe with the distributed engine (see 1.2.1)

- A further increase in efficiency and decrease in fuel consumption through **Boundary Layer Ingestion (BLI)** because of reduction in overall drag

1.2.1 Propulsion efficiency, wake filling and BLI

The propulsion efficiency is strictly related to the principle of wake filling and boundary layer ingestion, as shown in this paragraph.

The Froude propulsion efficiency, η_p is defined as the ratio of usable power $T \cdot V_\infty$ compared to the kinetic power P added to the flow. For a jet engine isolated from an aircraft wing, it is:

$$\eta_P = \frac{T \cdot V_\infty}{P} = \frac{\dot{m}\left(V_{jet} - V_\infty\right) \cdot V_\infty}{\frac{\dot{m}}{2}\left(V_{jet}^2 - V_\infty^2\right)} = \frac{2V_\infty}{V_{jet} + V_\infty} \tag{1}$$

Equation 1 indicates that the reduction of V_{jet} implies an increase in the propulsive efficiency, requiring an augmentation of $\dot{m}$ for a fixed thrust T. This is the basic principle of the distributed propulsion: multiplying the engines it is possible to reduce V_{jet} because the mass flow rate is greater. The propulsion efficiency could be improved by distributed propulsion and boundary layer ingestion since a jet flowing near the exit of the trailing edge of a wing profile "fills in" the wake directly behind the wing. Propulsion efficiency loss is a consequence of any kinetic energy left in the wake (i.e., non-uniformities in the velocity profile) compared to that of a uniform velocity profile. For example, naval engineers implement this concept on ships by installing the propeller directly behind a streamlined body.

These non-uniformities cause fluid friction, and dissipation of energy in the trailing wake, until the velocity field is uniform again. The friction losses can be reduced by designing an integrated propulsion system that fills in these non-uniformities. Figure 1 on page 4 illustrates the basic principle of wake filling.

To explain this principle, let's analyse the configuration of a podded engine (no BLI) and an engine designed for BLI. The engine accelerates the flow to a velocity u_e such that the created momentum balances the drag of the airframe D_A. In the wake of the podded configuration let's consider a slower velocity u_w

$$F_{\text{engine}} = \dot{m}(u_e - u_\infty) = \dot{m}(u_\infty - u_w) = D_A \tag{2}$$

The power given to flow by the engine is:

$$P_{\text{podded}} = \frac{\dot{m}}{2}(u_e^2 - u_\infty^2) = \frac{F}{2}(u_\infty + u_j) \tag{3}$$

The power required for flight is:

$$P_{\text{useful}} = D_A u_\infty = \dot{m}(u_e - u_\infty)u_\infty \tag{4}$$

Let's suppose now that the boundary layer is completely ingested and the engine re-accelerates the wake back to the free-stream. The force provided by the engine is, since $u_j = u_\infty$:

$$F_{\text{engine}} = \dot{m}(u_e - u_w) = \dot{m}(u_\infty - u_w) = D_A \tag{5}$$

The power given to the flow in this case corresponds to:

$$P_{\text{BLI}} = \frac{\dot{m}}{2}(u_e^2 - u_w^2) = \frac{\dot{m}}{2}(u_\infty^2 - u_w^2) = \frac{F}{2}(u_\infty + u_w) \tag{6}$$

The power required, P_{useful}, is the same. So, it is self-evident that

$$P_{\text{podded}} > P_{\text{BLI}} \tag{7}$$

Less power is required to sustain the same drag force on the airframe with boundary layer ingestion. In other words, the difference in energy input between the two situations occurs because of a specific force, less power needs to be added to the flow that enters the engine with a lower velocity.

1.2.2 Embedded versus podded engines

BLI cannot be achieved with podded engines which are far away from the boundary layer. It is necessary to use engines that are partially buried in the airframe. The advantages of BLI-engine's configurations are numerous, and have already been enumerated in 1.2. Though, they have some drawbacks such as the problem of a non uniform flow and S-duct shaped conducts that could lead to flow separation and degradation of the performance; the distortion of flow at the fan face may cause vibration, noise and structural problems; a more integrated design is necessary. Podded engines represent a proven technology which has been in use for more than 60 years in the aviation. The main advantage of the podded technology over the BLI-configuration is the possibility to capture a uniform flow in the inlet of the engines, at the price of a larger wetted area, larger structural weight (pylons and nacelles) and the interference of the pylon to the wing aerodynamics.
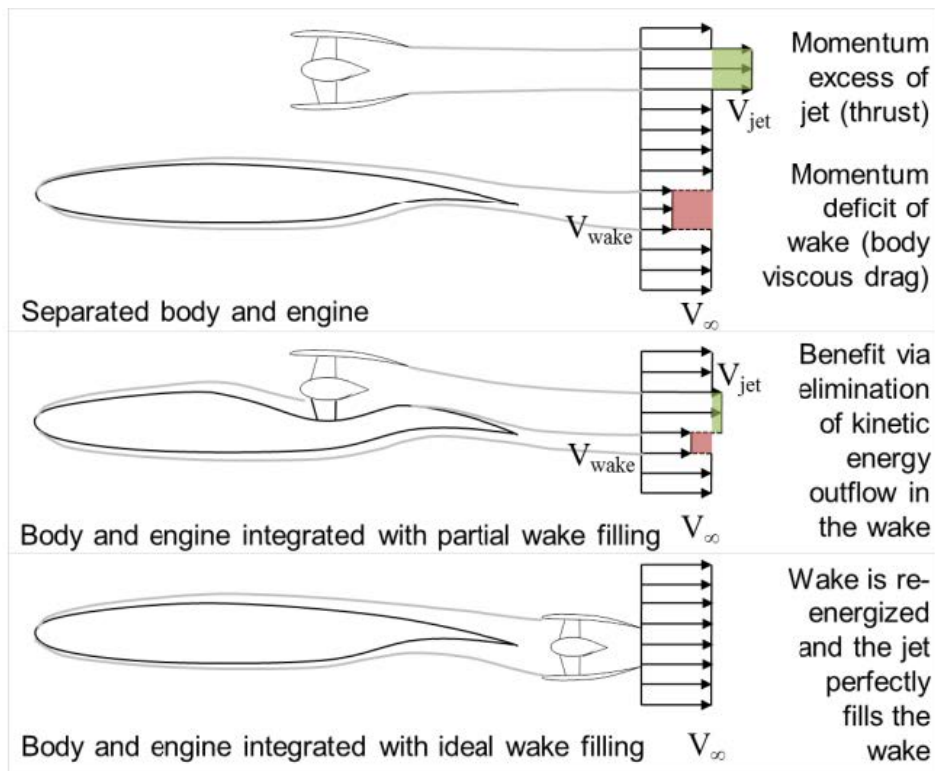
Figure 1: Illustration of the basic principle for wake filling. From Steiner et al., 2012

1.2.3 BLI and power estimation in embedded configurations

The simple proposition that thrust is the force applied by the propulsion system to the airframe is not particularly helpful in the analysis of the performance of an aircraft even for podded configuration, since a significant part of the total thrust can be distributed over the airframe surfaces which are the exterior part of the engine: for example the external surfaces of the nacelle are part of the engine, but do generate some friction drag. It has been necessary to set up a conventional and consistent definition for the various component of thrust and drag, so that no component is overlooked or none is counted twice. This structure is known as "thrust and drag bookkeeping".

For classical configuration of aircraft propulsion systems an agreement between engine manufacturers and aircraft builder has been drawn up in order to specifically define what is responsible for drag and thrust, referring themselves, for example, to the quantity "standard net thrust".

In distributed propulsion, thrust and drag are ambiguous and it is difficult to tell apart because of the strict integration: the airframe flow is modified by the presence of the engine within the airframe itself. Therefore, it is impossible to agree on a standard norm to define surfaces and volumes for engine and airframe. The classical approach of estimating power and momentum through the definition of a control volume and subsequent integration of the fluxes over the delimiting surfaces is inherently limited by the impossibility to define differences between thrust and drag. A possible approach is given by [Drela, 2009] that proposes an
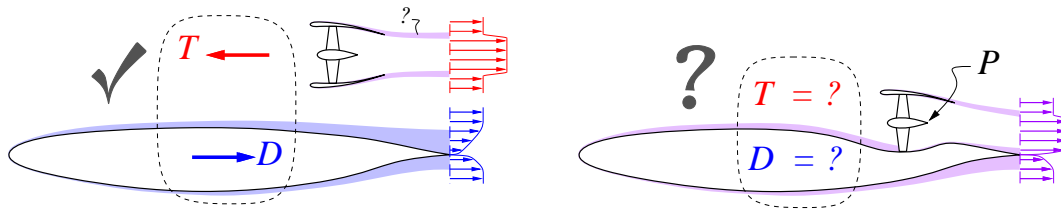
Figure 2: Illustration of the problem of the thrust-drag bookkeeping for distributed propulsion

energy-based integral balance to estimate the power in such configuration. The application of such energy-based approach is beyond the scope of this internship (which focus on the aerodynamics effects of the distributed propulsion), however, some configurations that we are going present will be analysed through an energy based approach in other works of the department.

1.2.4 Some concepts of distributed propulsion

Current research has focused on distributed multi-fans driven by limited numbers of engines. Fox example, fans could be driven by turbo-shaft core engines, either mechanically or electrically.
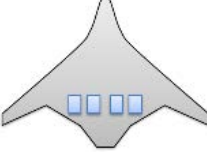
One of the main drivers for such an investigation is the possibility to achieve a very low specific thrust (i.e. FPR, Fan Pressure Ratio), without increasing the nacelle drag, as for standard configurations (see Hall and Crichton, 2005). Moreover, a lower FPR leads to an increase in propulsive efficiency (see 2 on page 7).Also, boundary layer ingestion could be easily implemented for this configuration. Neglecting the power system and focusing only at the propulsion system, a certain number of configurations has been proposed. See Hyun Dae Kim, 2010 and Steiner et al., 2012. In the table 1 on the next page a synthesis of these concepts is illustrated.

1.3 THE DISPURSAL PROJECT

The DisPURSAL project (Distributed Propulsion and Ultra-high Bypass Rotor Study at Aircraft Level) is an EU-funded project of the 7th Framework Programme for Research and it was kicked off in 2013. The international project consortium consists in the EADS Innovation Works, ONERA, Bauhaus Luftfahrt (BHL) and the Central Institute for Aviation Motors (CIAM, Russia). The project aims to explore the efficiency potential of distributed propulsion and propulsive fuselage concepts for aircraft motive over through multi-disciplinary numerical experimentation and optimisation at aircraft level.

The key aspects that have to be addressed include aircraft design and optimisation, airframe-propulsion integration, power-train system design and advanced flow field simulation. Detailed analysis will elucidate the implication of using hybrid power architectures through combinations of different power sources like, for example, gas turbines, advanced batteries or fuel cells.

Table 1: Distribution propulsion concepts based on a multi-fans system

Concept	Description
	Aft mounted fans covering the cylindrical fuselage
	Blended wing body with embedded fans on top of the lifting body trailing edge. See for specific details: Felder, Huyn Dae Kim, et al., 2011
	Tube and wing configuration with fans integrated within a split-wing.
	Tube and wing concept with fans mounted on the upper wing side.
	Cylindrical fuselage with circumferential fan at the aft section.
	Cross-flow fan embedded into the trailing edge of the wing

1.4 OBJECTIVE OF THIS INTERNSHIP

This internship takes place under the framework of this project. The main objectives of this internship could be resumed as follows:

- To do a preliminary design assessment of the feasibility of distributed propulsion, identifying the main parameters, through a 0D preliminary model

- To study and analyse a new kind of boundary condition to model a propulsive system (we will see later, an actuator disk surface)

- To study different 2D-model to analyze the aerodynamics effect of those configuration

- An attempt to model distributed propulsion in a 3D model

This work can be used, if necessary, as a base for subsequent studies related to distributed propulsive system that could be carried on in the future in the department.

2 | PRELIMINARY DESIGN AND MODELS

Distributed propulsion is a quite new subject in ONERA, and there is no relevant experience in simulating such phenomena. Therefore, it is necessary to identify and to delimit the main parameters of the problem. The first step is to develop a 1-D model through basic equations of compressible gas-dynamics and compare it to real data. In addition, in this chapter also we will introduce a first CFD model that will be used for analysis in the next chapter.

2.1 A MONODIMENSIONAL MODEL

Following figure 3, we model a distributed propulsion system as a fan within a convergent conduct where 2 and 13 are the planes just before and after the fan, the section 0 is the section corresponding to the stream-tube to infinity, and 9 is the exit section of our conduct. According to our hypothesis based on neglecting the power system, it is possible to model the fan as an object that introduces a jump in the total pressure of the fluid flow. The fan is therefore modelled by the FPR, Fan Pressure Ratio defined as:

$$FPR = \frac{P_{i_{13}}}{P_{i_2}} \tag{8}$$

We assume the fluid being as a perfect gas and we impose that $P_9 = P_0$, (adapted nozzle). The thrust has therefore the usual expression, $T = \dot{m}(V_9 - V_0)$, with $\dot{m} = \rho_i A_i V_i$. Boundary conditions pressure and temperature, P_0 , T_0, are fixed since they are functions of the altitude (we use the ISA, International standard atmosphere model), that in our model is fixed too. The Mach number M_0 is assumed.
For this preliminary study we also assume an iso-entropic flow in the conduct
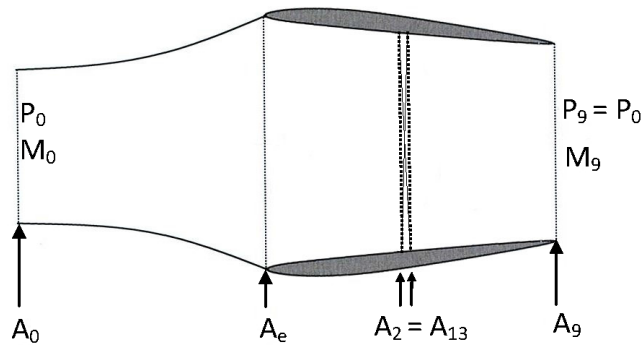
Figure 3: Model for preliminary study. Notation for different sections

(but not for the fan) and, using classical compressible gas-dynamics relations, we obtain:

$$M_9^2 = \left[\frac{P_{i_9}}{P_9}^{\frac{\gamma-1}{\gamma}} - 1 \right] = \left[\frac{P_{i_{13}}}{P_0}^{\frac{\gamma-1}{\gamma}} - 1 \right] \frac{2}{\gamma - 1} \tag{9}$$

because $P_{i_9} = P_{i_{13}}$ deriving from iso-entropic flow hypothesis.

$$\frac{P_{i_{13}}}{P_0} = \frac{P_{i_{13}}}{P_{i_2}} \cdot \underbrace{\frac{P_{i_2}}{P_{i_0}}}_{=1} \frac{P_{i_0}}{P_0} = FPR \cdot \left(1 + \frac{\gamma - 1}{2} M_0^2 \right)^{\frac{\gamma}{\gamma-1}} \tag{10}$$

In conclusion:

$$M_9^2 = \frac{2}{\gamma - 1} \left[\left(1 + \frac{\gamma - 1}{2} M_0^2 \right)^{\frac{\gamma}{\gamma-1}} FPR^{\frac{\gamma-1}{\gamma}} - 1 \right] = f(M_0, FPR) \tag{11}$$

We pose $\beta = \frac{V_9}{V_0}$, remembering that $c = \sqrt{\gamma R T}$ so we get:

$$\beta = \frac{M_9}{M_0} \sqrt{\frac{T_9}{T_0}} \tag{12}$$

Let's introduce η_f as the polytropic efficiency of transformation operated by the fan (which for an iso-entropic transformation is equal to 1). We can write:

$$\frac{T_9}{T_0} = \underbrace{\frac{T_9}{T_{i_9}}}_{=\frac{1}{p(M_9)}} \cdot \underbrace{\frac{T_{i_9}}{T_{i_{13}}}}_{=1} \cdot \underbrace{\frac{T_{i_{13}}}{T_{i_2}}}_{=\left(\frac{P_{i_{13}}}{P_{i_2}} \right)^{\frac{\gamma-1}{\gamma\eta_f}}} \cdot \underbrace{\frac{T_{i_2}}{T_{i_0}}}_{=1} \underbrace{\frac{T_{i_0}}{T_0}}_{=p(M_0)}$$

$$= \frac{P_{i_{13}}}{P_{i_2}}^{\frac{\gamma-1}{\gamma\eta_f}} \cdot \frac{p(M_0)}{p(M_9)} \tag{13}$$

$$= FPR^{\frac{\gamma-1}{\gamma\eta_f}} \cdot \frac{\left(1 + \frac{\gamma-1}{2} M_0^2 \right)}{\left(1 + \frac{\gamma-1}{2} M_9^2 \right)}$$

With $p(M_i) = \left(1 + \frac{\gamma-1}{2} M_i^2 \right)$.

Remembering 11, $\frac{T_9}{T_0}$ is a function of M_0, FPR only, and therefore we can deduce, from 12 and 13, that β is a function of M_0, FPR only.

To individuate the surface section we impose the thrust, or equally, the c_d, that is the drag coefficient. Indeed we attain, substituting the definition of T and $\dot{m}$:

$$\frac{T}{\frac{1}{2} \rho_0 V_0^2 A_{ref}} = c_d = 2 \frac{\rho_9}{rho_0} \frac{A_9}{A_{ref}} \frac{V_9 (V_9 - V_0)}{V_0^2} \tag{14}$$

Since $P_9 = P_0$, then $\frac{\rho_9}{\rho_0} = \frac{T_0}{T_9}$. Expressing velocity and temperature as functions of β and Mach number, it yields:

$$\frac{A_9}{A_{ref}} = c_D \cdot \left(\frac{M_0}{M_9} \right)^2 \cdot \frac{\beta}{\beta - 1} \tag{15}$$

Propulsive efficacity as
a function of FPR, Mach=0.87, h= 11000
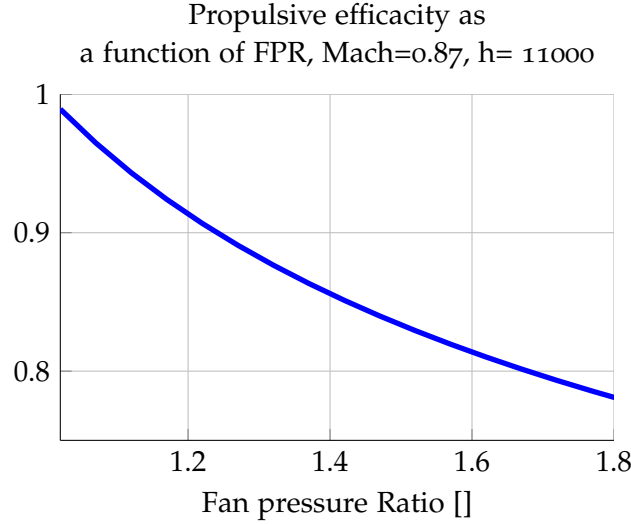
Figure 4: Propulsive efficiency as a function of Fan Pressure Ratio

that is, the exit surface of the conduct is a function of FPR, M_0, c_D. It means that in our simplified model the three main parameters are the required thrust, the fan pressure ration and the cruise Mach number. Moreover, we emphasize that the propulsive efficiency is a function of FPR and M_0 only. Indeed:

$$\eta_p = \frac{2V_0}{V_9 + V_0} = \frac{2}{\beta + 1} \tag{16}$$

As we can see from fig. 4, in order to increase the propulsive efficiency it is necessary to decrease FPR.

Once identified the main parameters, it is essential to understand which range of values is really significant as to them. We will analyze two different configurations for the disposition of distributed propulsion:

- A series of fans that are disposed along the wing (that is representative also of a BWB aircraft with equivalent wingspan). All engines are assumed to be circular and each one tangent to the next one.

- A series of fans that are around the fuselage, except for the lower quarter. It would not be reasonable to put some engines there because of the aircraft inclination during the taking-off.

2.1.1 Fans on the wings

We can express A_{ref} as a function of the wingspan $2 * b$ and the aspect ratio λ. Being $\lambda = (2b)^2 / A_{ref}$,

$$A_{ref} = \frac{(2b)^2}{\lambda} \tag{17}$$

If we impose a condition for the maximum number N of fans on the wing (with diameter d), such as:

$$N \cdot d \leq 2 \cdot b \tag{18}$$

FPR fixed, max number of engines on the wings
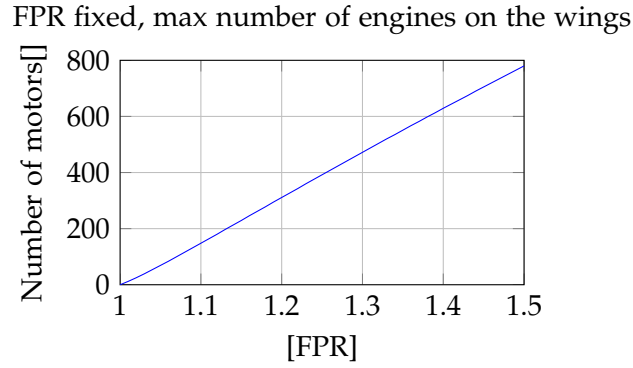
Figure 5: Max N of propulsors on the wings as a function of *FPR*. Cruise Mach Number: $M = 0.8$, configuration similar to a Boeing 777.

After substituting for A_{ref}, d, N in equation ,it is possible to find a simple expression for the maximum number of fans that we could put along the wings:

$$N \leq \frac{\pi \lambda}{4K} \quad \text{with} \quad K = c_D \cdot \left(\frac{M_0}{M_9}\right)^2 \cdot \frac{\beta}{\beta - 1} \tag{19}$$

In figure 5 we show the maximum number of engines that could be put over the wings of an aircraft similar to a Boeing 777 (in term of aspect-ratio, wing span, cruise speed), for a given c_D, as a function of *FPR*. We observe that the configuration we have chosen for our simplified model is not limited by geometric considerations. The same trend can be found in different aircrafts, such as Airbus A320.

Figure is significant because it points out the boundaries for our parameters. Indeed, for a given configuration (in this case, Boeing 777), it shows us that there are some areas that are not worth studying: for a relatively high number of fans/engines the increase in term of performance is very low (i.e. equivalent to a reduction of FPR, see fig.). The historic evolution of standard engines can be observed in the same figure: there is an increase in terms of diameter in order to obtain an increase in propulsive efficiency. It is recognized that we are attaining a maximal size for an aircraft turbo-fan propulsor, because of structural limits. Bigger and bigger turbofans are required to obtain very low *FPR*. Distributed propulsion becomes interesting for this reason: it is possible to obtain very low *FPR*, (up to 1.05) with engines of reasonable size. It is worth to remark that the curves are very sensible to cruise Mach number: they are subjected to a (reasonable) scale effect. In this figure, $M = 0.8$: reducing it to $M = 0.2$ leads to a much smaller possible field of variation for the main parameters (in the chart, the rectangle in the lower left corner).

Diameter of propulsors for different FPR
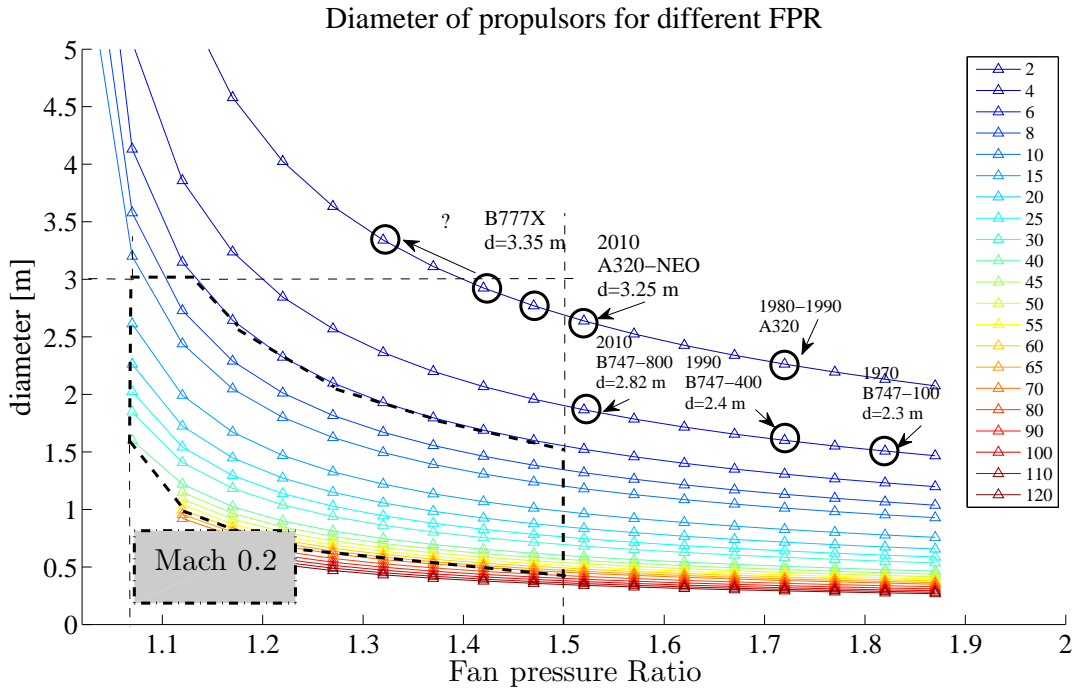
Figure 6: Size of the propulsor on the wings as a function of *FPR*. Cruise Mach Number: $M = 0.8$, configuration Boeing 777. Each curve is at constant N. The bold dotted lines represent the boundary for the values of FPR and N of interest. The rectangle in the lower corner is the size of the equivalent plot for $M = 0.2$: scale effect.

2.1.2 Fans around the fuselage

A geometric limiting condition for propulsor around the fuselage can be found: considering the figure 7, we have:

$$2r = 2(R + r)\sin\alpha \tag{20}$$

with r, R being the radius of the propulsors and the fuselage. The condition that we need to use is:

$$2\sin\alpha \cdot N \le \frac{3}{2}\pi \tag{21}$$

where we imposed $\frac{3}{2}\pi$ to limit the disposition of propulsor in the upper part of the fuselage. The inequality is no- linear and has to be solved numerically:

$$2N \arcsin\frac{\frac{r}{R}}{1 + \frac{r}{R}} \le \frac{3}{2}\pi \quad \text{with} \quad \frac{r}{R} = \frac{d}{D} = \sqrt{\frac{16K}{\pi\lambda N}} \cdot \frac{b}{D} \tag{22}$$

Figure 7: Description of the geometry and associated notation.

with K defined as in equation 19 on the facing page. In figure 8 on the next page we can observe that the maximum number of engines that we can put around the fuselage is considerably low: geometry represents a limiting factor for this configuration. The figure 9 on the following page is the equivalent of figure 6 for

FPR fixed,max number of engines on the fuselage
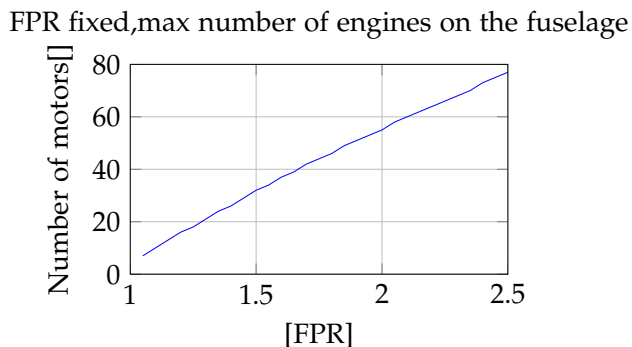
Figure 8: Max N of propulsors on the fuselage as a function of *FPR*. Cruise Mach number: $M = 0.8$, configuration similar to a Boeing 777, fuselage diameter $\simeq 6.5m$.

this configuration. The fields of variation for the distributed propulsion study are, in this case, very restrictive. Because of geometric limitations, it is not possible to obtain FPR lower than 1.2. It means that such a configuration could be utilized only in a mixed configuration with the first one. For lower Mach number, it is indeed possible to use such a configuration with fans at very low FPR, because of the scale effect due to the Mach number. The impossibility to exploit this configuration at higher Mach number has lead to the proposal of a radical, different configuration: a single, large, circumferential fan rotating around the fuselage (see Steiner et al., 2012).
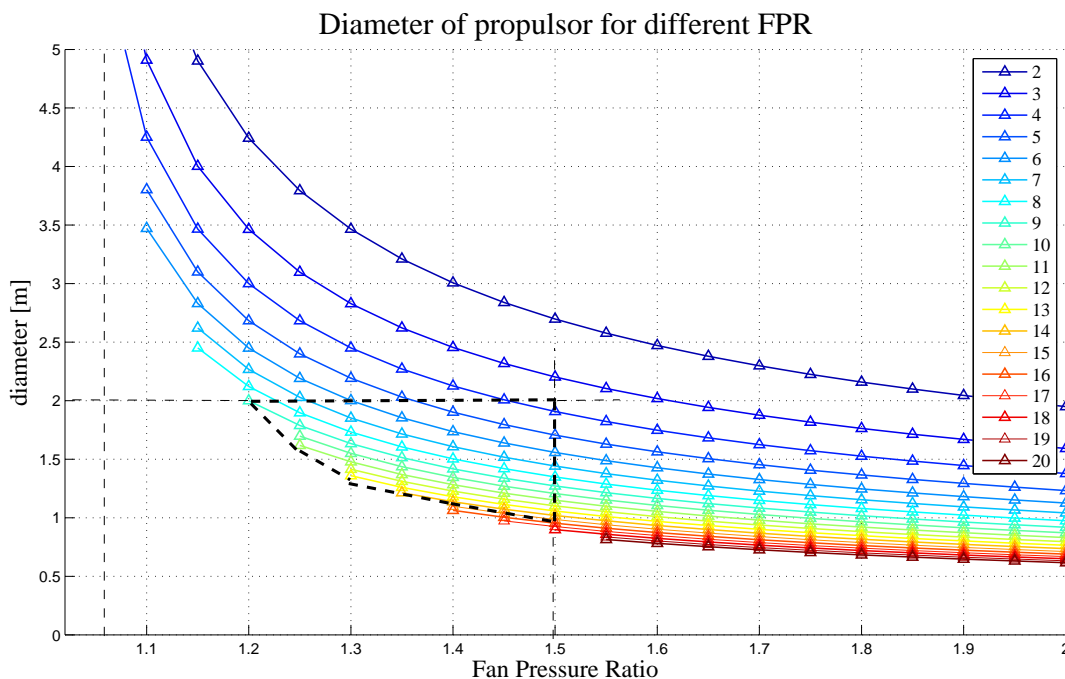
Figure 9: Size of the engines on the fuselage as a function of *FPR*. Cruise Mach Number $M = 0.8$, configuration Boeing 777. Each curve is at constant *N*. The fields of variation for FPR, N for distributed propulsion are plotted.

3 | THE CFD MODELS AND TOOLS

In the previous section we have made an abstraction of the engines fan through the introduction of a parameter, the Fan Pressure Ratio, which fits perfectly in a one-dimensional problem. The first question should be how to model the fan, and its equivalent FPR, for a CFD study. In the first part of this chapter we will analyse methods and strategies that we have analysed and used for the CFD studies of the different models.

In the last four sections of the chapter we will describe the three 2D models that we have prepared for the numerical simulations:

- in the first model the engine is located in the aft part of the wing profile

- In the second model the engine is over the leading edge of the wing

- In the third one, a bigger engine is put over the wing, to fit realistic limits for regional aircraft.

- In the last one, the engine is put directly behind the wing profile, to ingest all the boundary layer and to fill the wake.

3.1 ELSA CFD CODE

The code that has been used for this internship is "elsA" (Ensemble Logiciel de Simulation Aérodynamique).

ElsA is a CFD software developed by ONERA since 1997 to simulate internal and external aerodynamics for compressible, laminar or turbulent fluid flow. ElsA solves the compressible 3-D Reynolds averaged Navier-Stokes equations for fixed or moving bodies using a cell centered finite-volume method with second order upwind or central space discretization with scalar or matrix artificial dissipation on multi-block structured meshes. Discrete equations are integrated either by multi-step Runge-Kutta schemes with implicit residual smoothing, by backward Euler integration with implicit LU schemes. A large variety of turbulence models are available, ranging from eddy viscosity to full differential Reynolds stress models, and including Detached Eddy Simulation (DES) and Large Eddy Simulation (LES). ElsA is written in several languages: C++ for the main internal architecture, FORTRAN for the core functions of the CFD simulation, and python, for the user interface. Indeed, python scripts are submitted to the (command-line) software to launch CFD computations.

3.2 THE BOUNDARY CONDITIONS ACTUATOR DISK

In the previous chapter we have identified the Fan Pressure Ratio as one of the central parameters for the study of distributed propulsion. There are several ways to model a fan in CFD analysis. Since we are not interested in local effects (like swirl, unsteady flow, etc.), we are going to focus now on its global effects over the aircraft aerodynamics, so we chose to model it with an actuator disk, where the action of the fan (or any similar rotating object) is modelled through a force per unit of surface that is added as a source term through the surface of this actuator disk.

We will proceed very briefly to show how this boundary condition is introduced in elsA. Let's note ρ as density, $\vec{V} = [u, v, w]^T$ the velocity, $E = e + \frac{1}{2}\rho\vec{V}^2$ the total energy, where e is the internal energy, that for perfect gas is $\frac{P}{\rho} = (\gamma - 1)e$. We pose $\vec{W} = [\rho u, \rho v, \rho w]^T$ the conservative variable for the mean field. $\Omega_{ijk}, V_{ijk}, S_{ijk}$ denote respectively the elementary cell, its volume and its surface and $\vec{n}$ the external normal. The RANS equation in conservative and integral form can be written:

$$\frac{\partial u}{\partial t} \int_{\Omega_{ijk}} W \, d\mathbf{V} + \int_{S_{ijk}} \overline{\overline{F_c}} \cdot \vec{n} \, d\mathbf{S} - \int_{S_{ijk}} \overline{\overline{F_d}} \cdot \vec{n} \, d\mathbf{S} = 0 \tag{23}$$

Where $\overline{\overline{F_c}}$ and $\overline{\overline{F_d}}$ are respectively the convective flux and the diffusive flux. The finite volume method for a spacial discretization leads to a system of ODE for the temporal evolution of W:

$$\frac{d}{dt}(VW)_{ijk} + R_{ijk} = 0 \tag{24}$$

where R_{ijk} is the flux balance through S_{ijk}. We can write it as the sum of all the contributions over the six faces of the cell:

$$R_{ijk} = \sum_{1}^{6} H_l \text{ with } H_l = (q_c)_l - (q_d)_l \tag{25}$$

and $(q_c)_l, (q_d)_l$ are respectively the convective flux and the diffusive flux through the face l. The actuator disk introduces in the flow field a discontinuity of velocity and pressure. This discontinuity is introduced as a source term in the conservation equations. Let's consider two adjacent cells with the common face being a part of the surface of the actuator disk. Let's note $\Omega_{ijk_{up}}$ the upstream cell and $\Omega_{ijk_{dw}}$ the downstream one. The two numerical fluxes H_{up} and H_{dw} are equal and opposed in direction. For the upstream cell we have:

$$\frac{d}{dt}(VW)_{ijk} + \sum_{1}^{6} H_l \text{ with } H_l = 0 \tag{26}$$

but for the adjacent cell we add the source term:

$$\frac{d}{dt}(VW)_{ijk} + \sum_{1}^{6} H_l \text{ with } H_l = T_{dw} \tag{27}$$

with T_{dw} being calculated from the force $\vec{F}$ as:

$$T_{dw} = \left(\begin{bmatrix} 0 \\ \vec{F} \\ \vec{F} \cdot \vec{V} \end{bmatrix} || \vec{n} || \right)_{dw} \tag{28}$$

Equation 27 on the preceding page can be rewritten with the modified flux:

$$\frac{d}{dt}(VW)_{ijk} + \sum_{l \neq dw} H_l + H_{up} - (H_{dw} + T_{dw}) = 0 \tag{29}$$

.

3.2.1 Calculation for mass,momentum, energy balance

In order to analyse the boundary conditions, as we will do in section 3.2.3 on page 17 and to calculate all quantities, such forces, FPRs, velocities, power around in the actuator disk in the conduct, it is necessary to calculate the balances.

- The mass balance of a enclosing volume (in absence of source of mass) should be zero:

$$\int_{S \cup \Sigma} \rho \vec{u} \cdot \vec{n} dS = 0 \tag{30}$$

- The balance of momentum for a volume around the actuator disk writes:

$$\int_{S \cup \Sigma} \rho \vec{u} \vec{u} \cdot \vec{n} dS = \int_{S \cup \Sigma} -P \vec{n} dS + \int_{S_{AD}} \vec{F} dS \tag{31}$$

where $S = S_1 + S_2$ corresponds to two plane surfaces parallel to the actuator disk surface and orthogonal(but not necessarily) to the x axis, and Σ corresponds to the rest of the surfaces that enclose the volume. S_{AD} is the surface where the actuator disk is acting. The position of S_1 and S_2 is variable. The contribution of viscous stress is neglected.

- The energy balance can be written in order to estimate the "power" theoretically given by a hypothetical engine to the fluid through the boundary condition:

$$\mathbb{P} = \int_{S \cup \Sigma} \rho \vec{E} \vec{u} \cdot \vec{n} + P \vec{u} \cdot \vec{n} \; dS \tag{32}$$

where $\mathbb{P}$ is the power, P is the pressure and E is the total energy. For all Navier Stokes calculations we point out that the contribution of the heat flux and of the viscous tensors stresses have been neglected.
Those balances have been calculated with a python code that has been developed specifically to this . The spacial integrals are approximated with a first order scheme, and all balances have been validated by Tecplot result's for the same configurations.

3.2.2 The calculation of the lift/ drag coefficient in elsA

In this section we will briefly show how all coefficients (lift,drag and pitching moment) are calculated. Considering the equation 31, and projecting to the x-axis we get:

$$\vec{F_{net}} = \int_{S_{out} \cup \Sigma} (\rho u \vec{v} + (p - p_\infty)\vec{x} - \bar{\bar{\tau}} \cdot \vec{x}) \cdot \vec{n} \; dS - V_\infty \int_{S_{in}} \rho u \; dS \tag{33}$$

where S_{out} are exit surfaces and S_{in} inlet surfaces, Σ the other surfaces of the control volume. (p_∞ because of the nullity of the volume integral of a constant over a closed domain). In this expression we can identify different terms:

$$\vec{F} = \int_\Sigma (p - p_\infty)\vec{x} \cdot \vec{n} \, d\mathbf{S} \qquad\qquad\qquad\qquad\text{Pressure drag} \qquad (34)$$

$$- \int_\Sigma \bar{\bar{\tau}} \cdot \vec{x} \cdot \vec{n} \, d\mathbf{S} \qquad\qquad\qquad\qquad\text{Friction drag} \qquad (35)$$

$$+ \int_{S_{out}} (\rho u\vec{v} + (p - p_\infty)\vec{x} - \bar{\bar{\tau}} \cdot \vec{x}) \cdot \vec{n} \, d\mathbf{S} \quad \text{Dynalpy of the exit surfaces} \qquad (36)$$

$$+ \int_{S_{in}} u_\infty \rho \vec{V} \cdot \vec{n} \, d\mathbf{S} \qquad\qquad\qquad\qquad\text{Additive drag} \qquad (37)$$

Considering an angle of attack $\alpha = 0$ (otherwise it would be necessary to consider $u \cos\alpha + v \sin\alpha$) in elsA the following quantities are defined:

- Convective flux of ρ:

$$convro = \int \rho \vec{V} \cdot \vec{n} d\mathbf{S} \qquad\qquad\text{gives the mass flow rate} \qquad (38)$$

- Convective flux of ρu:

$$convrou = \int \left(\rho \vec{V} \otimes \vec{V} + (p - p_\infty)\vec{x}\right) \cdot \vec{n} d\mathbf{S} \qquad\qquad (39)$$

- Diffusive flux of ρu

:

$$diffrou = - \int \vec{\tau}_x \cdot \vec{n} \, d\mathbf{S} \qquad\qquad\text{gives the friction over the surface} \qquad (40)$$

So we can write:

$$F_x = \sum_{allsurfaces} convrou + diffrou \qquad\qquad (41)$$

Finally, to obtain drag coefficient we just need to transform all quantities into non-dimensional ones. c_D so obtained is the global result of the sum of the thrust of the engine and the drag of the complete configuration, that, as we already explained in 1.2.3 on page 4 cannot be told apart from thrust in such integrated configurations.

Lift coefficient corresponds to the equivalent quantities for the z-axis, so analogously we can write:

$$F_z = \sum_{allsurfaces} convrow + diffrow \qquad\qquad (42)$$

with w indicating all quantities over z-axis.
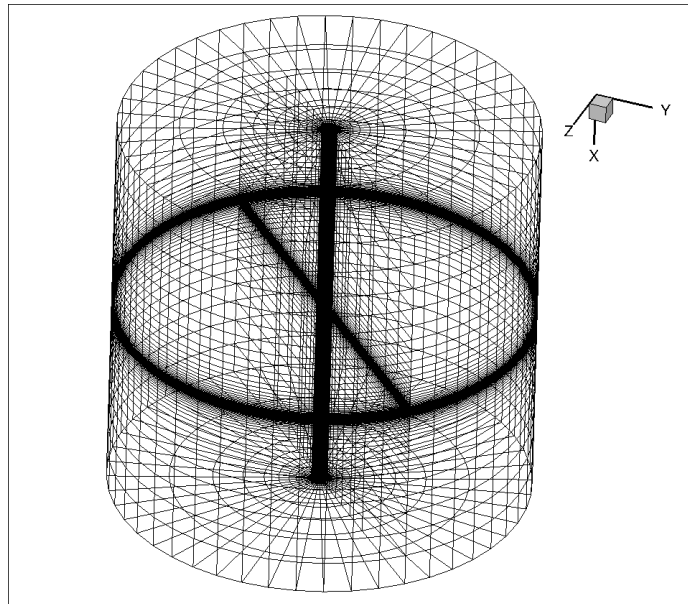
Figure 10: Geometry and mesh for the test case for the boundary condition. The actuator disk it is a planar ring (in x-plane) at the center of the volume

3.2.3 Analysis of the boundary condition

We have conducted an analysis of the boundary condition "actuator disk" to better analyze his numerical behaviour in terms of output for a given force as input. The test case is given in figure 10. It can be described as a pipe with large thickness with the actuator disk being at the center of this volume. Firstly, we have observed that this boundary condition causes some oscillations of the total pressure (and of the total temperature) upstream of the boundary condition, that are not physical. In figure 11 on the following page we can observe this phenomenon. We have verified that those oscillations are directly proportional to the force that we impose to the actuator disk. For a given input force for the actuator disk, the output force in the simulation is not exactly the same. We calculated, as explained above in section 3.2.1, a momentum balances around the boundary conditions and calculated the force $\vec{F}$, moving the surfaces $S1$ and $S2$ progressively away from the boundary condition in order to study the relationship of the total pressure oscillation with the output force.

In figure 12 on the next page we can observe that the output force is not constant according to the section $S1$ and $S2$ of integration, and it is affected by the same oscillation that affects total pressure and temperature. The choice of the section of integration seems critical for balances of thrust and force (that are crucial for the objective of this study).

Using the mass balance as shown in 3.2.1 on page 15, equation 30 on page 15 it turns out that this boundary condition is not conservative, but the ratio, for example, of the residual calculated from the equation 30 over the total ingoing mass flow is less than 10^{-2}. Moreover, the same ratio is of the same order of magnitude of the residual L2 of the density. Therefore, we can not definitely conclude our analysis about the conservation of mass through the actuator disk surface. In fig-
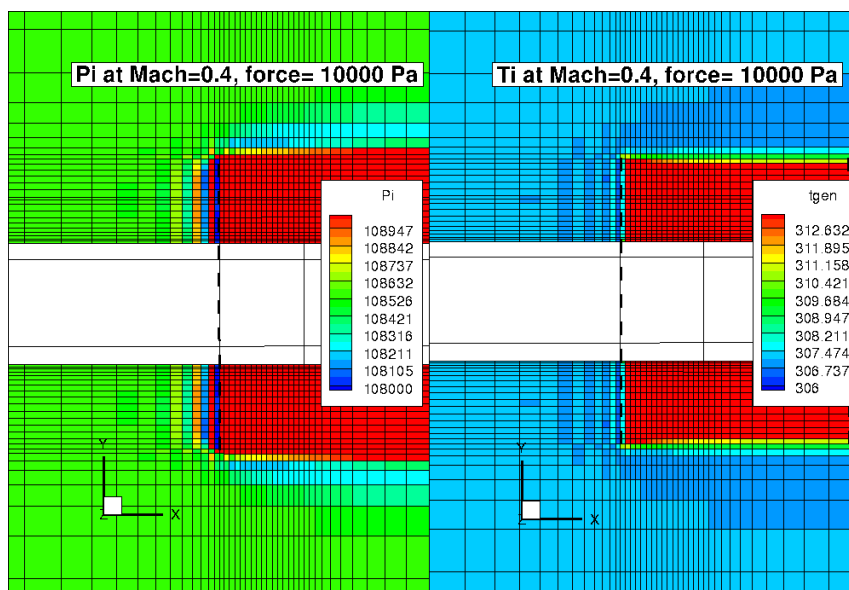
Figure 11: Oscillation of the total pressure and the total temperature. The dashed black line corresponds to the actuator disk surface section. Simulation for Mach number=0.4, force=10000 pa, $P_\infty = 97215Pa$. The plot is scattered because it is showed the primary value of total pressure in the cell, that it is not interpolated.
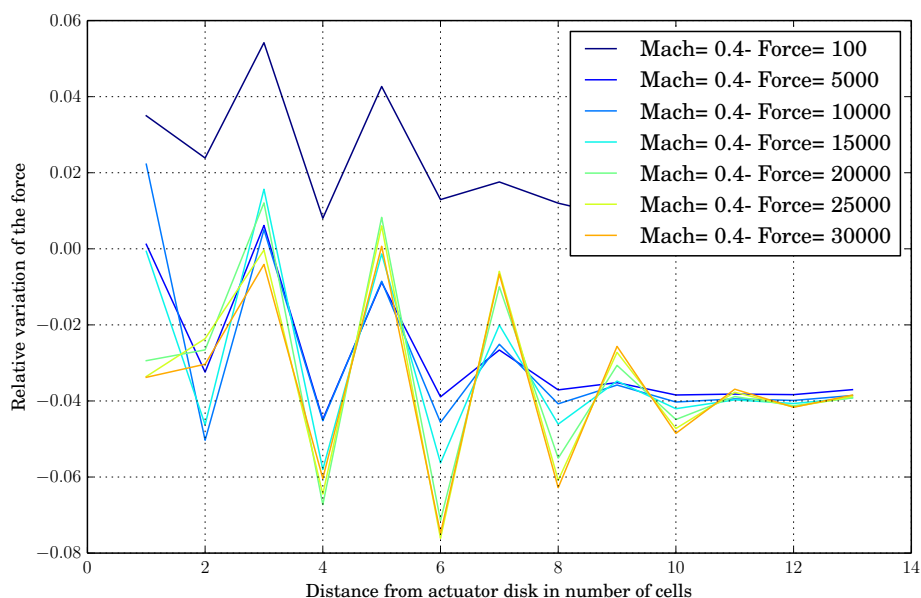
Figure 12: Relative variation of force= $\frac{F_{out} - F_{in}}{F_{in}}$ as a function number of cells separating S1 and S2 from the actuator disk. Configuration test case (see fig 10 on the preceding page and 11).
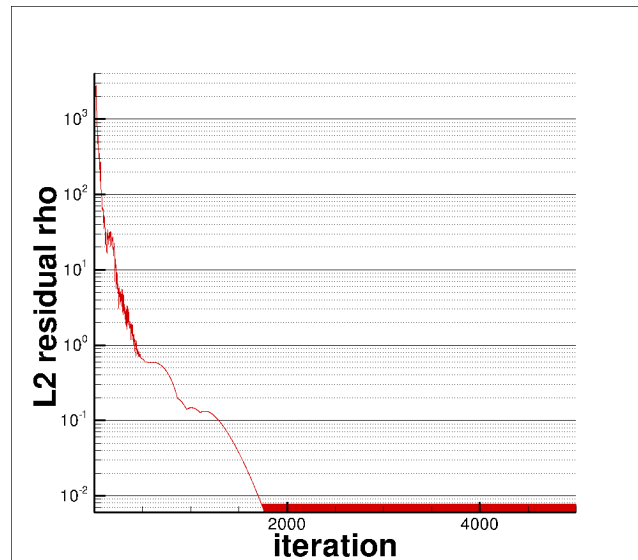
Figure 13: L2 residual of ρ: convergence curve. $M = 0.4, force = 10000Pa$

ure 13 the figure shows the convergence curve for L2 residual of ρ. The residual stabilizes after a certain number of iterations: this is probably due to the size of the mesh that could be refined to reduce the residual.

We applied the same analysis of the boundary conditions to the geometry that we will describe in section 3.3 on page 21. This case is substantially different from the cylindrical test case, because the boundary condition "actuator disk" is adopted between two solid boundaries, in a 2D convergent conduct bounded by two airfoils, which representing a model for distributed propulsion. In the first test case, the actuator disk is applied in open space where there are no walls. In figure 14 on the following page we can observe the total pressure oscillations that we have already put in evidence for the other case.

A momentum balance has been done, as for the previous case. Results are shown in figure 15 on the next page. It can be observed that is substantially different from figure 12 on the facing page. We note the same qualitative behaviour: the results of the momentum balance are influenced by the oscillations that it have been observed in the fluid flow.
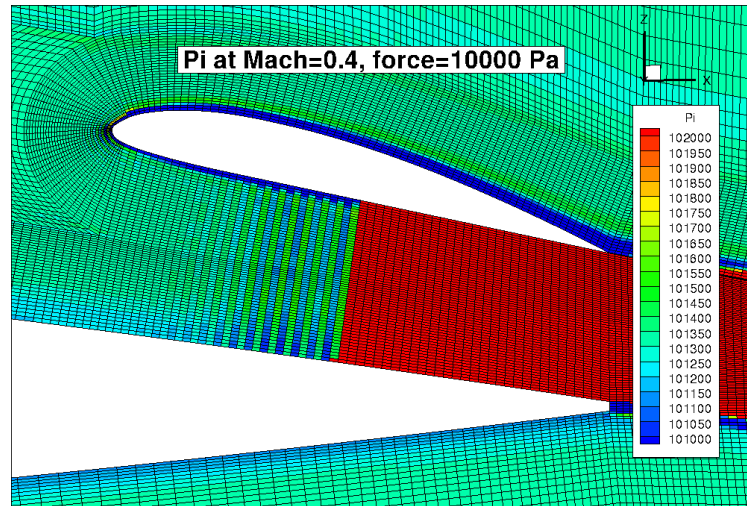
Figure 14: Oscillation of the total pressure. Simulation for Mach number=0.4, force=10000 pa, $P_\infty = 101325 Pa$. The plot is scattered because it is showed the primary value of total pressure in the cell, that it is not interpolated.
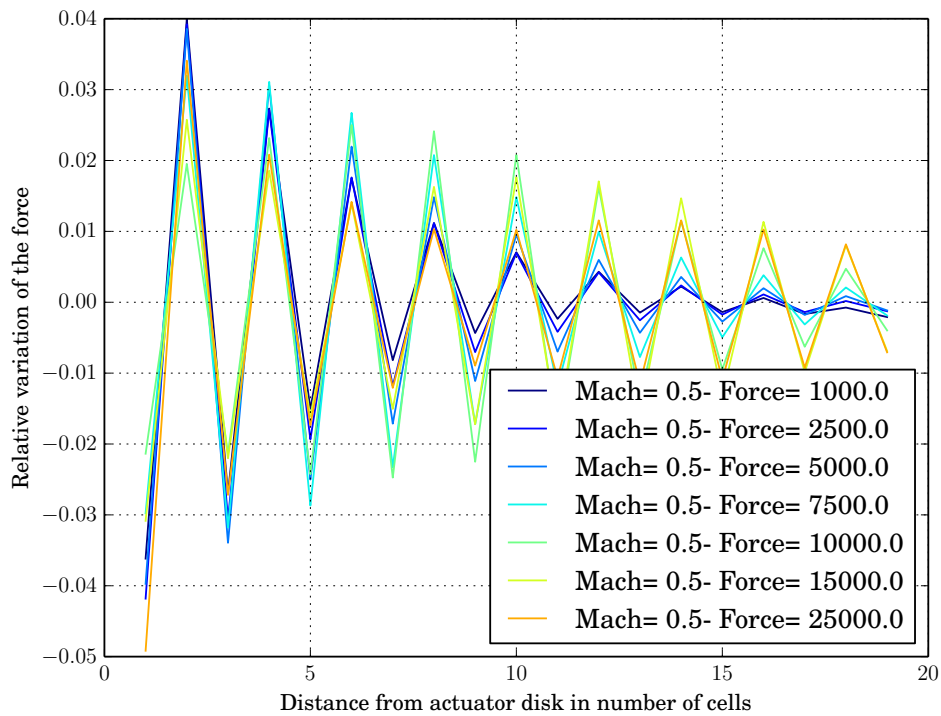
Figure 15: Relative variation of force= $\frac{F_{out} - F_{in}}{F_{in}}$ as a function number of cells separating S1 and S2 from the actuator disk. Configuration 2D between two profiles. See 3.3 on the facing page

3.3 THE 2D MODEL FOR DISTRIBUTED PROPULSION

At this point we have understood how to model an ideal fan of an engine with the actuator disk boundary condition (see 3.2 on page 14),so we can build a complete first model for distributed propulsion. In order to focus on the main aspects and effects of distributed propulsion, the model should be as simple as possible. Therefore we have opted for a 2D model described in the following section. As it can be seen in figure 16, it consists of two airfoils: the first, a NACA 23012, which represents a section of a wing with a unitary chord length, and a second one (CLARK Y) representing the upper part of the nacelle of an imaginary engine. They create together a convergent conduct, representing the fan conduct. In the middle of the conduct, we impose the boundary condition "actuator disk" as described in section 3.2 on page 14. *The airfoils profiles have been chosen for the following reasons: firstly, they are extremely common in aerodynamics; secondly, the aft part of both of them is flat, creating a conduct that is easier to size and design.*
It should be pointed out that we idealise the fan as "a surface" by which the total pressure is increased of a $\Delta P_i = (FPR - 1) * P_{i_2}$. We do not assume that this surface should be circular but we rather imagine it as a rectangular surface with a unitary width (because we are describing a 2D-model). Moreover, the shape of the area does not affect the conclusion that we have drawn so far. The fact that up to now we imagined the propulsors as a series of circular fans was to establish a visual and immediate comparison with present turbofan engines.
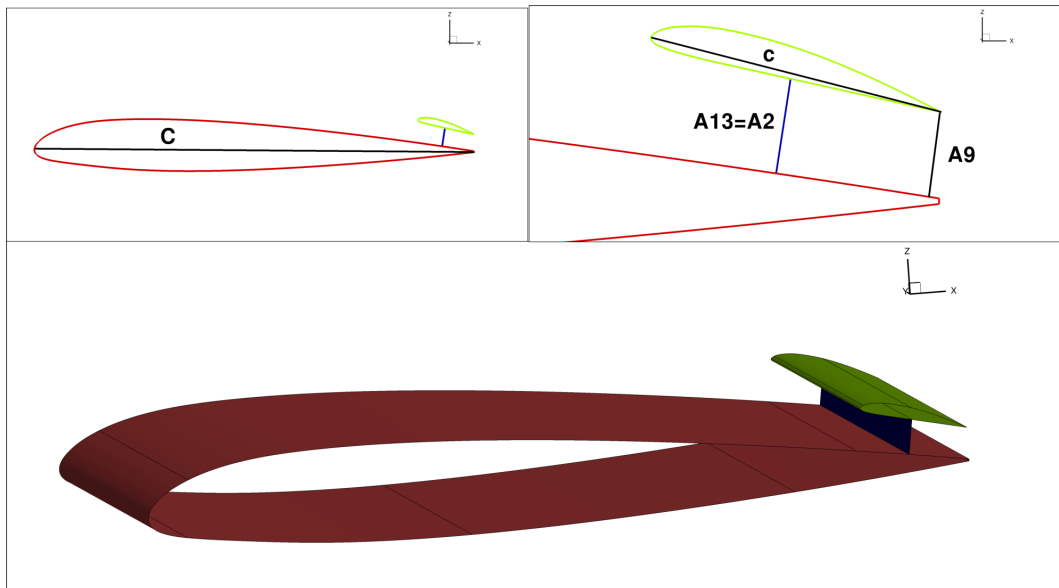
Figure 16: Different view of the model used for initial CFD analysis. The lower sub-image shows an extrusion of the 2D model that has to be used in elsA CFD code in order to process 2D analysis. (indeed, elsA accepts only 3D geometry,even for 2D simulations)

To size this conduct we have chosen a design point configuration and following the ideas that we have already shown in 2. Given a unitary chord for the main profile (NACA 23012), and given b=$\frac{1}{2}$ (wingspan) and $\lambda = 1$ such that $A_{ref} = 1$,

we assume that the depth of this model is $l = 1$. The sizing of the conduct has been done with the following hypothesis (following the notation of figure 3 on page 7):

- P_0, T_0 are given (atmospheric conditions)

- Exit pressure $P_9 = P_0$ (adapted nozzle)

- The Mach number right before the fan is assumed to be $M_2 = 0.5$, that represents a standard value for Mach number at leading edge of fan blades.

- A drag coefficient $c_D = 0.0250$

- The FPR is given and assumed low (respect to the standard of turbofan engines) : $FPR = 1.1$, and $P_{i_{13}} = P_{i_2} + \Delta P_i$, with $\Delta P_i = (FPR - 1) * P_{i_2}$

The total thrust of this model corresponds to the result of a dynalpy balance on the entire conduct:

$$F_{tot} = \rho_9 * A_9 * v_9^2 - \rho_0 * v_0^2 * A_0 \tag{43}$$

whereas the thrust generated by the fan is the result of a dynalpy balance between 2 and 13:

$$F_{fan} = A_{13} * \left(P_{13} + \rho_{13} * v_{13}^2\right) - A_2 * \left(P_2 + \rho_2 * v_2^2\right) \tag{44}$$

and they are in general not equal (for example, for an incompressible flow, it can be shown that $F_{tot} = 2F_{fan}$). It can be assumed that $\frac{c_{Dtot}}{c_{Dfan}} = \frac{F_{tot}}{F_{fan}}$, that lets us estimate the drag coefficient or, equivalently the thrust required.
The resolution of the conduct is a standard exercise of compressible gas dynamics, and in our hypothesis we can express all physical quantities (section, pressure, total pressure, temperature etc.) as a function of the exit surface. Therefore, the ratio $\frac{F_{tot}}{F_{fan}}$ calculated from equation 43 and 44 can be expressed as a function of A_9, but it can be observed (numerically) that it is independent from A_9, depending only on M_0, M_2, FPR. For a given c_{Dtot}, remembering equation 15 on page 8 we also attain that:

$$\frac{A_9}{A_{ref}} = \mathbf{c_{Dfan}} \cdot \left(\frac{M_0}{M_9}\right)^2 \cdot \frac{\beta}{\beta - 1} \tag{45}$$

that let us calculate the requested exit area of the conduct. Using continuity equation through the fan and $P_{i_{13}} = P_{i_2} + \Delta P_i$, the conduct can be solved completely. For the complete resolution, see A. A parametric study has been done, as usual, varying M_0 and FPR. In figure 17 on the facing page it is shown the exit area that corresponds to the distance between the two airfoil for our 2D model, for different combinations of the two parameters.
We choose the size of the engine finally fixing $M_0 = 0.5$ and FPR=1.1. The results of the sizing are shown in table 2 on the next page. Through those easy calculations we sized a model that, as shown in the next chapter, we will analyse thoroughly studying it both with Euler and Navier Stokes equation. In the next part we will show a different model that we have prepared for further studies.
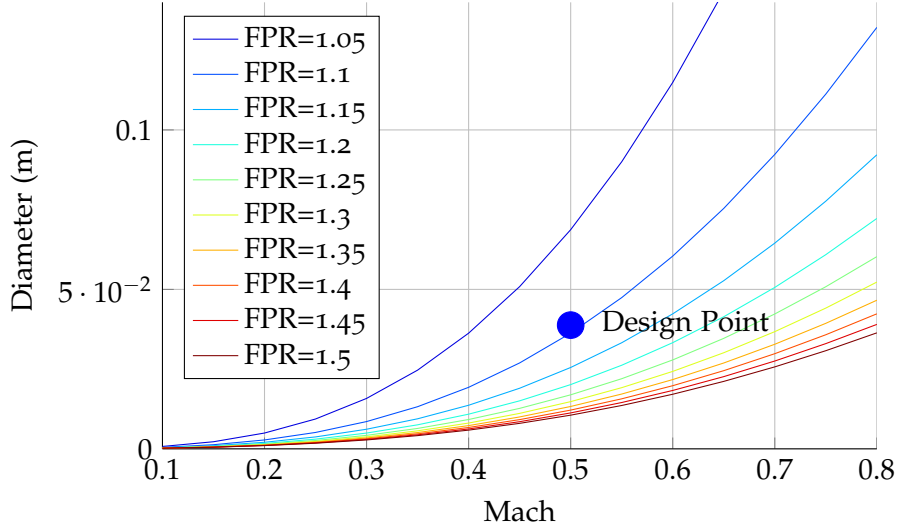
Figure 17: Exit area A_9 as function of M_0 and FPR, for $P_0 = 101325, T = 300K$

Table 2: Geometric and physics parameter for the considered model. **The sizing has been done for Mach=0.5**

Parameter	Value	Description
FPR	1.1	Fan Pressure Ratio
A_9	0.0388	Exit surface area
A_2	0.0433	Fan area
C	1	Naca 23012 chord length
c	$2.5A_9$	Clark Y chord length

3.4 LEADING EDGE CONFIGURATION

Distributed propulsion being such a new subject, it is necessary to explore different configurations. The decision to put the engine in the aft part of the wing has been arbitrary, based on the easiness of designing a conduct (that is almost straight) between the two profiles and based on the previous knowledge about possible benefits given by boundary layer ingestion. So we also analysed a configuration where the engine is put in the forward part of the wing profile. The model is directly derived from the previous one: the wing profile and nacelle profile (NACA 23012 and CLARCY Y) have been kept unchanged along with their dimension . We moved the CLARK Y profile and aligned it with the leading edge of the NACA23012. The surface of the actuator disk has been kept almost unchanged, but we had to change its position relating to the CLARK Y. In the previous model we arranged the geometry so that the position of the actuator disk surface is at the half cord of the nacelle profile. In this case, we can not keep the same: a compromise is necessary between the position of the actuator disk, and the size of the convergent conduct. Indeed, in this case, the conduct can't be linear in its shape (and always convergent) but it is slightly divergent behind the actuator disk because of the curvature of the leading edge of the NACA 23012. Therefore, positioning the actuator disk further forward in the convergent/divergent conduct

would have caused an excessive acceleration of the fluid, making the two configurations substantially different in their behaviour (i.e the fluid would accelerate to supersonic speed). In figure 18 the configuration is shown,and it can be compared with figure 16 on page 21 of the previous one.
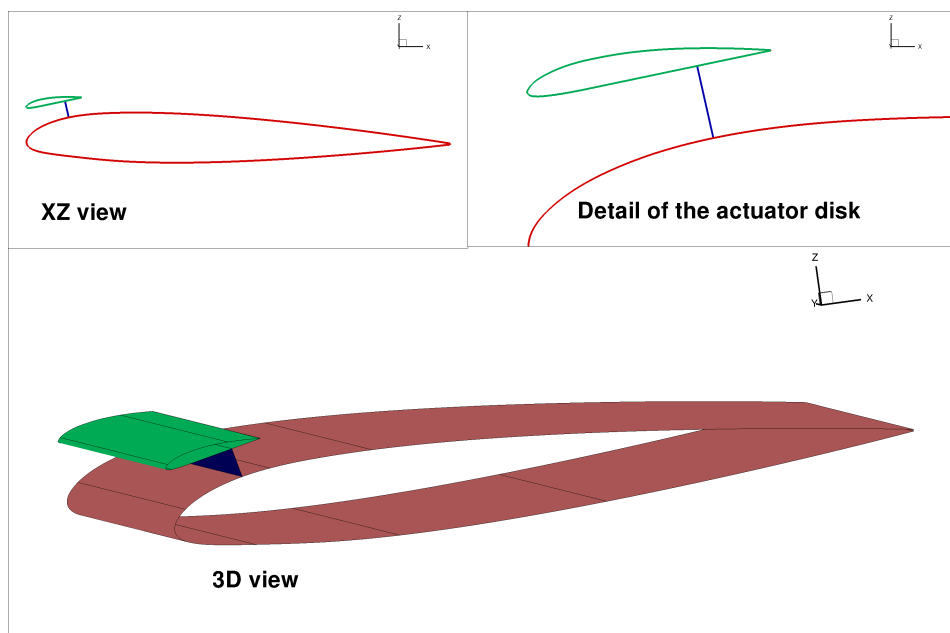
Figure 18: Model of the configuration with engine placed at leading edge

3.5 A BIGGER ENGINE IN THE AFT PART

The third configuration that we have analysed aims to:

- answering the question: *the configurations that we have prepared so far can equip a real aircraft with a given set of real parameters?*

- studying the parametric effect of the size of the engine

The answer to the first point is negative,as we will explain later on. Therefore we have designed this configuration to fit those (rough) limits. This configuration consists of an engine in the same position that in in 3.3 on page 21, but with a much bigger engine. In this chapter we will analyse a configuration with the engine that is in the same position that is shown in chap. 4 on page 27, but bigger in size. The configuration shown in this section has been sized through the procedure in appendix B on page 81. Briefly, our objective here is to equip a regional airliner (similar to an ATR) with an imaginary distributed propulsion system with dimension given in 3.3. Imposing a TOFL (Take Off Field Length) of $1km$ we recognize that this configuration can not take off in the given length, because it requires to provide the aircraft a too high acceleration. It would be necessary to impose a FPR=1.5, that for that configuration is too high and not interesting for future concepts of electrical engines. Moreover, we we will see in the next chapter, for
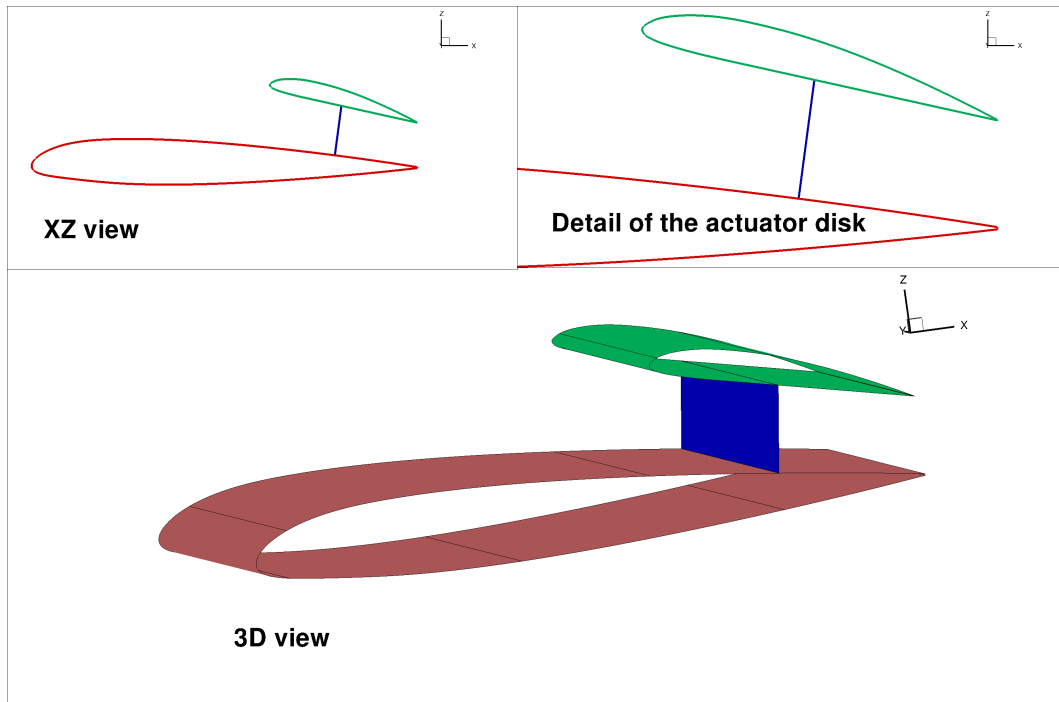
Figure 19: Model of the configuration with an engine of increased size.

FPR=1.25 we can observe a non physical behaviour in the conduct. Imposing a condition over the maximum C_l leads to a bound of the size of the engines that can fit the TOFL requirement for a reasonable FPR (1.10-1.15).

The configuration obtained is so composed: the wing profile and its size are kept unchanged. The engine diameter has been tripled (i.e. from 4 to 12 cm) and the nacelle, while maintaining the same profile has undergone a homothetic transformation (scaled up three times). The model is therefore shown in figure 19. The relative size of the engine to the wing is significant but we wanted to make a good comparison with the first case: changing other dimensions of the model would have signified the impossibility to discern the cause of the differences that we observe comparing it to the original case.

As you may notice, the sizing process in B on page 81 is iterative and the CFD simulation is part of it. As we will see, the simulation will show that a smaller engine could satisfy the requirements, but, since the objective is not to size a real aircraft, but only to understand distributed propulsion, we did not continue over the design process.

3.6 AN ENGINE BEHIND THE TRAILING EDGE

At the end, we also briefly analysed a configuration where an engine is located behind the trailing edge of the NACA wing, aligned with its chord axis. In this case, the engine has been symmetrized, adding a symmetrical CLARKY profile in the lower part. The engine surface has been doubled with respect to the first configuration, whereas the ratio between actuator disk surface and the exit surface
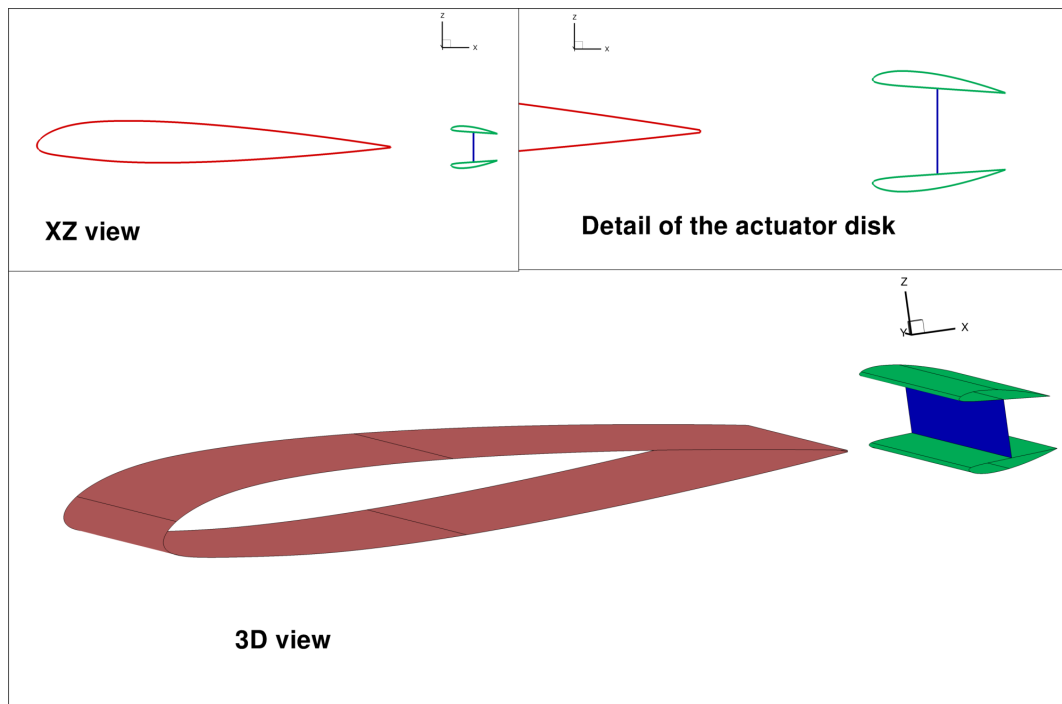
Figure 20: Model of the configuration with an engine that is located behind the wing and relatively far from it

is kept equal (ie, the angle of attack of the two CLARK Y profiles was reduced). The main characteristic of this engine is that, being located directly behind the wing, it ingest all the boundary layer that it develops around the NACA wing.

4 | CFD SIMULATIONS

In this chapter we will show all the results for the different models that we have detailed in the previous chapter. For the model that we firstly developed, see section 3.3 on page 21, we have done both a study based on Euler equations and one based on Navier Stokes equations. For the other models, only Navier Stokes equations have been used.

4.0.1 Physical and CFD parameters

All the models that have been presented in the previous chapter have been simulated at the same flight parameters given in the table 3:

Table 3: Geometric and physics parameter for the considered model.

Parameter	Value	Description
P_0	101325 Pa	External total pressure
T_0	300 K	External total temperature
M_0	0.2-0.5	Flow Mach number
FPR	1. - 1.25	Fan Pressure Ratio

The details of the implementations CFD simulation that are common to all the models are the following:

- The models are two-dimensional: the 3D representation in figures 16, 18 and 19 on page 25 corresponds to an "extrusion" of the 2D profiles, because elsA (CFD solver) accept only 3D geometry (in the extrusion direction, i.e. y-axis, there is only a element)

- The geometrical models that we presented have been simulated in a square field with side equal to 50 times the chord length (in this case 1 meter).

- On the far field boundaries a condition of non-reflection has been imposed

- On the wing surfaces a wall adiabatic condition (i.e. zero velocity) has been imposed for Navier Stokes simulations, whereas for Euler calculations a wall-slip condition (no friction at the surface) has been used.

- As already shown, the engine is modelled as a surface in the conduct to which is applied a "Actuator disk" boundary condition

- Air is considered as perfect gas

- Viscosity law: Sutherland law

- No transition models have been considered for boundary layers

- The turbulence model that has been used for Navier-Stokes simulation is "Spalmart Allmaras"

- Spatial numerical schemes: Jameson centred scheme with introduction of artificial dissipation

- Pseudo temporal integration schemes: scalar $LU - SSOR$ method

- The aerodynamic center for the calculation of pitching moment coefficient has been assumed, in first approximation, to be located at $\frac{1}{4}$ of the chord length of the wing profile. (Even if the presence of the second profile could invalidate this hypothesis)

- Multi-grid methods have been used where they helped the convergence of the simulation. Specifically, a *v-cycle* multi grid method with 2 level has been used.

- Variable CFL number (Courant-Friedrichs-Lewy): linear ramp up to CFL=100 in the first 100 iterations and constant thereafter.

- Parallel computing using 4/8 processor of the two departmental machines (daapuv)

- The parametric study for the angle of attack has been done using a "restart technique": i.e., for each $\alpha_i \neq 0$ simulation started from the results of the simulation for α_{i-1}, in order to speed up convergence and attain ourself to a more physical behaviour.

- elsA version that has been used: 3.4.04

4.1 TRAILING EDGE SMALL ENGINES: SIMULATION WITH AN EULER MODEL

As to the first model that we have developed in the previous chapter we decided to start with a simulation of a inviscid fluid, based on Euler equations for fluid flow. This step is necessary for different reasons

- To better understand all the aspects of the problem: the configuration, the boundary condition (see 3.2.3 on page 17),

- To test and validate all tools that have been developed to calculates all conservation balances over a relatively small and simpler mesh.

- To immediately assess the distance of the modelisation from the reality

- To exclude some cases for FPR that are evidently not reproducible in such a configurations

The mesh that we prepared (through Ansys ICEM) is shown in 21. The mesh has around 80000 elements. Different meshes have been tested and this is the one that corresponds to a good compromise between rate of convergence to the solution and number of cells.

It should be worth noticing that the use of much more refined meshes for an Euler calculation compromises its convergence. Indeed, the numeric schemes used to solve the discrete Navier Stokes/Euler equations (Roe Scheme, Jameson Scheme) introduce a numeric dissipation that is proportional to the aspect ratio of the cells. This numeric dissipation in NS simulation reproduces the behaviour of the boundary layer and actually helps the convergence, but for an Euler calculation, the use of a too refined mesh generates a "numerical" dissipative layer where the cells have an aspect ratio too elevated, effect that cannot be taken into account by the Euler equation of an inviscid (i.e. non dissipative) fluid, preventing the simulation from converging.

Mesh trailing edge, small engine: euler-
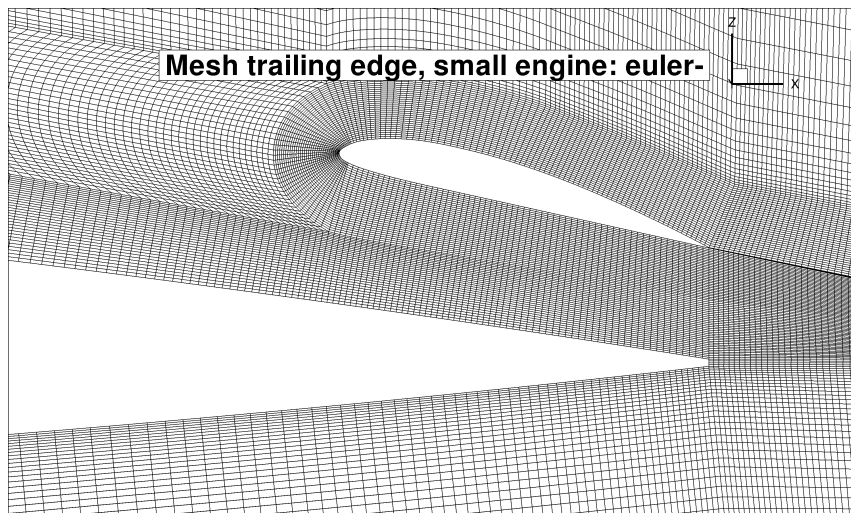
Figure 21: Detail of the mesh around the engine,configuration at trailing edge, euler computation

The variables for this parametric study are indicated in table 4. We have done a very large sweep for the various parameters; moving from take-off typical Mach number to "cruise" Mach number, for very different values of forces- from 0 to 25000 Pa- that approximatively correspond to FPRs $\simeq 1 \rightarrow 1.25$ (as we will see later on the section).

Table 4: Parametric study for trailing edge small engine, euler calculations

Parameter	Value
Mach Number []	0.2 0.3 0.4 0.5
Force (per unit of surface) [Pa]	0 1000 2500 5000 7500 10000 15000 20000 25000
Angle of attack [deg]	0° 2°

In this first parametric study there are many significant phenomena that are not

(a) Residual of ρ and ρu.

(b) Lift coefficient of the two profiles: convergence
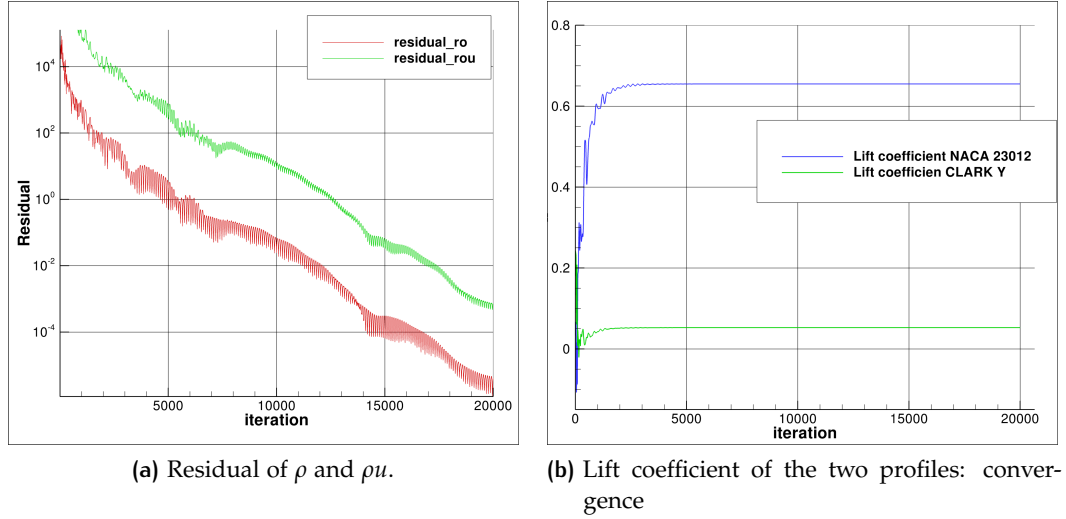
Figure 22: Convergence curve a case of the Euler 2D model. Mach=0.5, force=25000 Pa, $P_\infty = 101325 Pa$

reproducible, such as, for example, the effect of the angle of attack, stalling configuration, development of boundary layer and boundary layer ingestion. But, it is important to observe and understand the generic behaviour of the configuration. We will shortly present the main result of this study, not considering each case, but in terms of a global conclusion.

Because of the lightness of the mesh, for each simulation 20000 iterations have been done. All calculation converged. In figure 22 as an illustrative example, the convergence curves for the residuals of the density and ρu and for the lift coefficient of the two profiles.

4.1.1 Relationship between FPR and input force

In our preliminary analysis we identified the Fan Pressure Ratio as one of the key parameters to model a distributed propulsion system. But, as you may have noticed, in CFD analysis, the input for boundary condition "actuator disk" is not the FPR, but a force per unit of surface. A relationship needs to be established. From a theoretical point of view, it is possible to find a formula that links the FPR to the force and the Mach number at the fan section, but because of oscillations that we already identified, it is not possible to know precisely the M_{fan}. We propose a practical correlation, calculating the ratio as:

$$FPR = \frac{P_{i_{13}}}{P_{i_2}} = \frac{\frac{1}{A_{up}} \int_{A_{up}} P_i ds}{\frac{1}{A_{dw}} \int_{A_{dw}} P_i ds} \tag{46}$$

where A_{up} and A_{dw} are two sections in the conduct parallel to the actuator disk, the first before it and the second after. In figure 23 on the facing page results are shown. The is linear, and for low forces (< 10000 Pa) it could be assumed with good approximation, for example, that force= $5000 Pa$ corresponds to $FPR = 1.05$, force= $5000 Pa \rightarrow FPR = 1.10$.
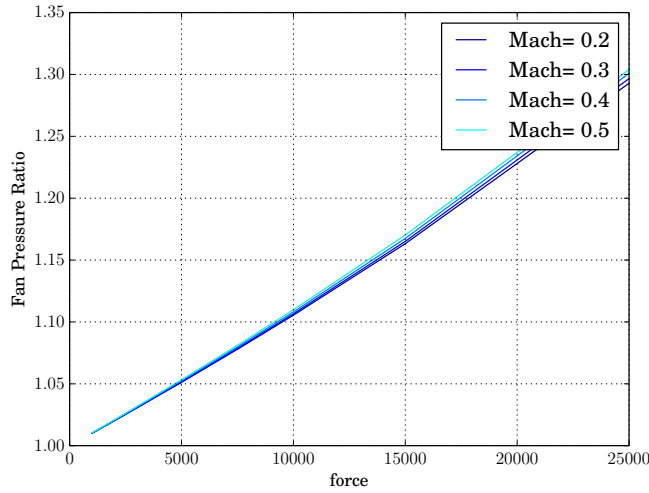
Figure 23: Relationship between FPR and input force

4.1.2 Lift coefficient and distributed propulsion

The problem of the trade-off between the lift coefficient at cruise speed, lift coefficient at take off and the speed at take-off/landing is directly concerned by this study. Indeed we can write the lift coefficient as:

$$c_L = \frac{m \cdot g}{\frac{\gamma}{2} P M^2 A_{\text{ref}}} \tag{47}$$

For a fixed altitude of 35000 ft, taking a cruise speed of $M = 0.8$ and a take off speed of $M = 0.2$ the ratio $\frac{c_{L_{\text{takeoff}}}}{c_{L_{\text{landing}}}} \simeq 5$. It means that the aircraft during landing/-take off must be able to generate a c_l five times greater than during cruising. The necessity of flaps for standard aircraft follows immediately. Future aircraft, using a distributed propulsion system, could take advantage from the ingestion/aspiration of the fluid flow through the fan. In figure 24 on the next page we can observe the behaviour of the two different angles of attack of the c_l for different Mach Number. The continuous line is the sum of the c_l of the two profiles, and the dashed line includes the vertical contribution of the thrust through the conduct. For the design point that we have illustrated above, the aspiration of the flow through the conduct causes an increase of the lift coefficient that is significant. For $M = 0.2$ the total lift coefficient of the system is three times the value of the reference case at null force. For an angle of attack = 2° this augmentation is even more significant. Therefore, as explained above, at first analysis, distributed propulsion seems to be able to increase the lift coefficient at low speed, envisaging the possibility of removing mechanical flaps.

4.1.3 Results

In figure 25 on page 33 it is shown the flow for different forces (per unit of surface) at fixed Mach Number, for an angle of attack = 0°. We observe the stream-tube of the conduct in the aft part of the system that changes enormously its shape and dimension according to different input forces for the boundary condition.

Figure 24: Lift coefficient as a function of the input force for different Mach Number and different input force. (Design point: $M = 0.5$, force= 10000
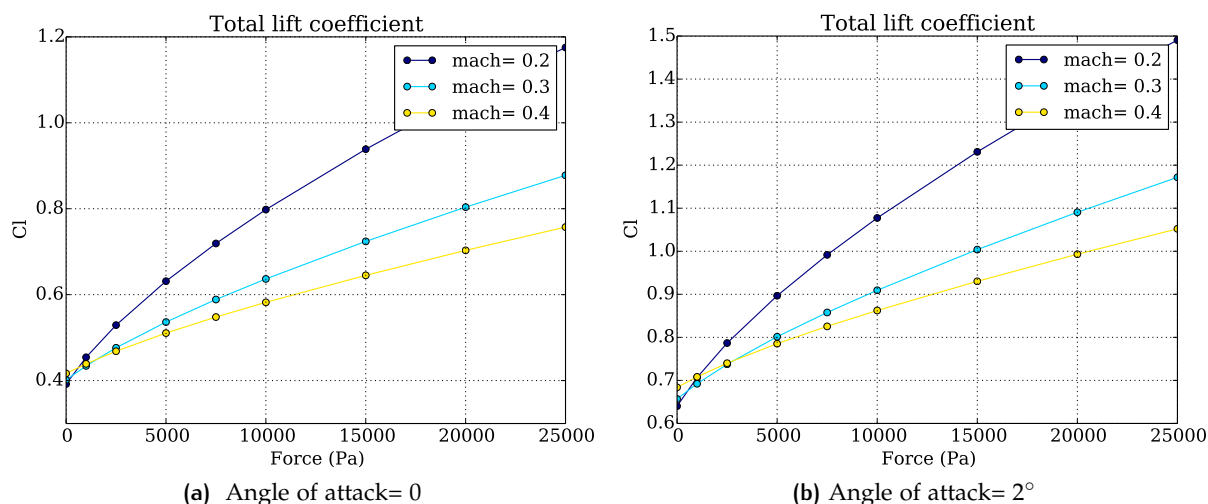
The supersonic flow that can be observed at the upper section of the profile could be explained by two main reasons: first, the CLARITY profile is not designed for such Mach number. Indeed we remember that the profile has been chosen because lower pressure side being very flat. Secondly, the relative angle of attack to the local flow is around 10°. In addition to this, the very low speed under the lower side forces necessarily the flow to accelerate on the other side.

The acceleration of the fluid flow is directly related to the increase of the lift coefficient as shown in figure 24: the acceleration causes a reduction of the pressure whereas under the lower side it remains almost constant.

In figure 26 and 27 on page 35 it is worth noticing the placement of the stagnation point over the CLARK Y profile according to the input forces. This is a characteristic that it will be found over all the simulations of the various models.

We observe that for very high forces the flow in the channel becomes supersonic. But, it seems not reasonable that the flow could become supersonic in such a way: considering the boundary condition that we are applying, how it has been used for, and the relative value of the force (25000 Pa $\simeq$ 25% of the input pressure, i.e. an FPR=1.25) we guess that we are simulating a non-realistic case for such a condition. Therefore, careful attention should be paid when drawing conclusion from such cases.

In conclusion, we present in figure 27 on page 35 some details of the simulation at Mach=0.2. The conduct is adapted for a lower value of the force (around 5000 Pa) and for higher input forces the stagnation point is clearly out of position. It is interesting to note that the conduct was designed for cruse Mach number (see table 2 on page 23). Globally it is evident that at this speed the system is much more sensible to variations in input force (the stream-tube explores very different dimensions).

To conclude, the configuration is sane and well-balanced, so we have proceeded to loot at more realistic Navier-Stokes simulations.
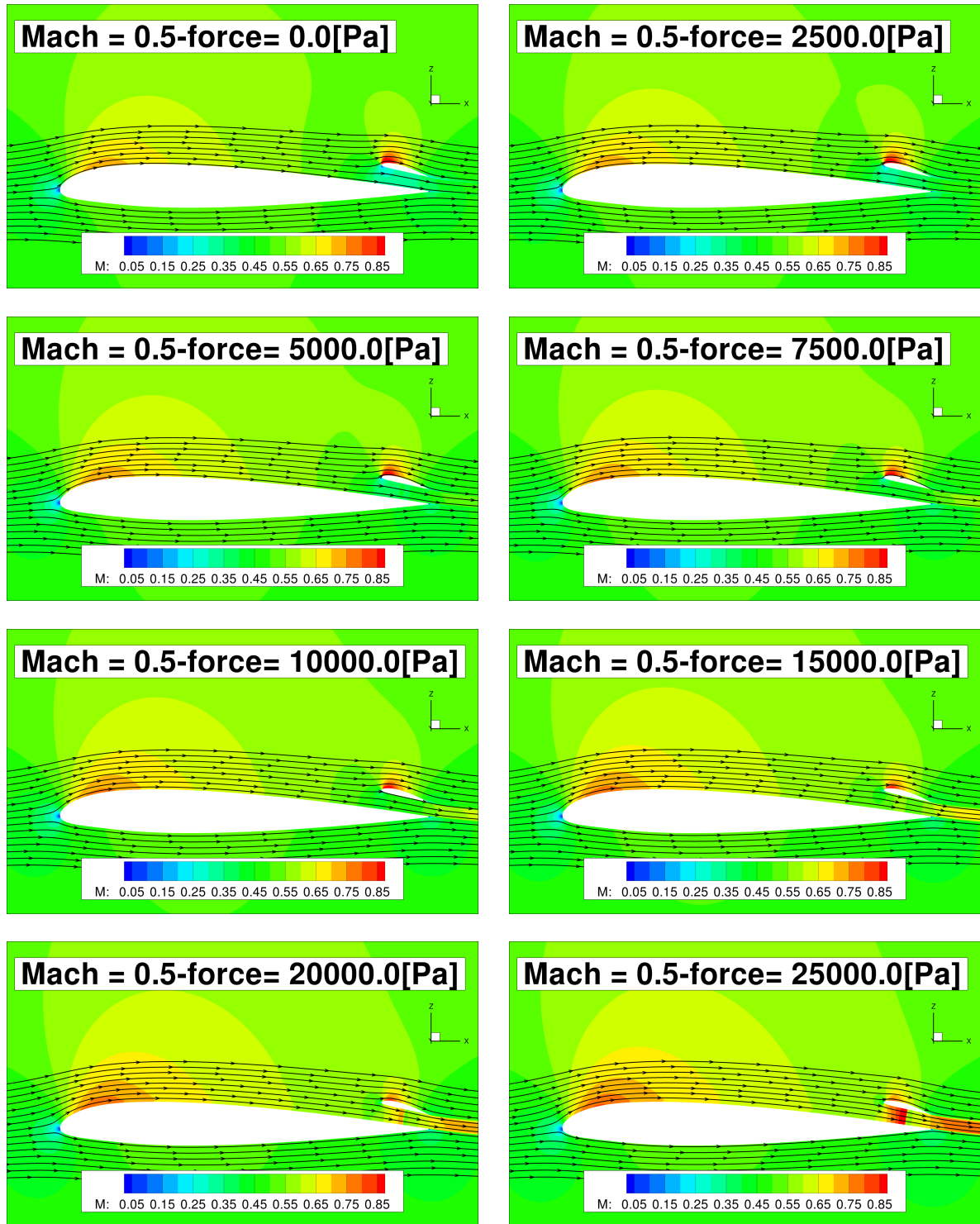
Figure 25: A global view of the Mach number around the two airfoils, for $M_0 = 0.5$ and different input forces (from 0.0 to 25000 Pa. $P_0 = 101325$, $T_0 = 300K$

Figure 26: Details of the Mach number in the conduct and around the CLARK Y profile, for $M_0 = 0.5$ and different input force (from 0.0 to 25000 Pa. $P_0 = 101325$, $T_0 = 300K$
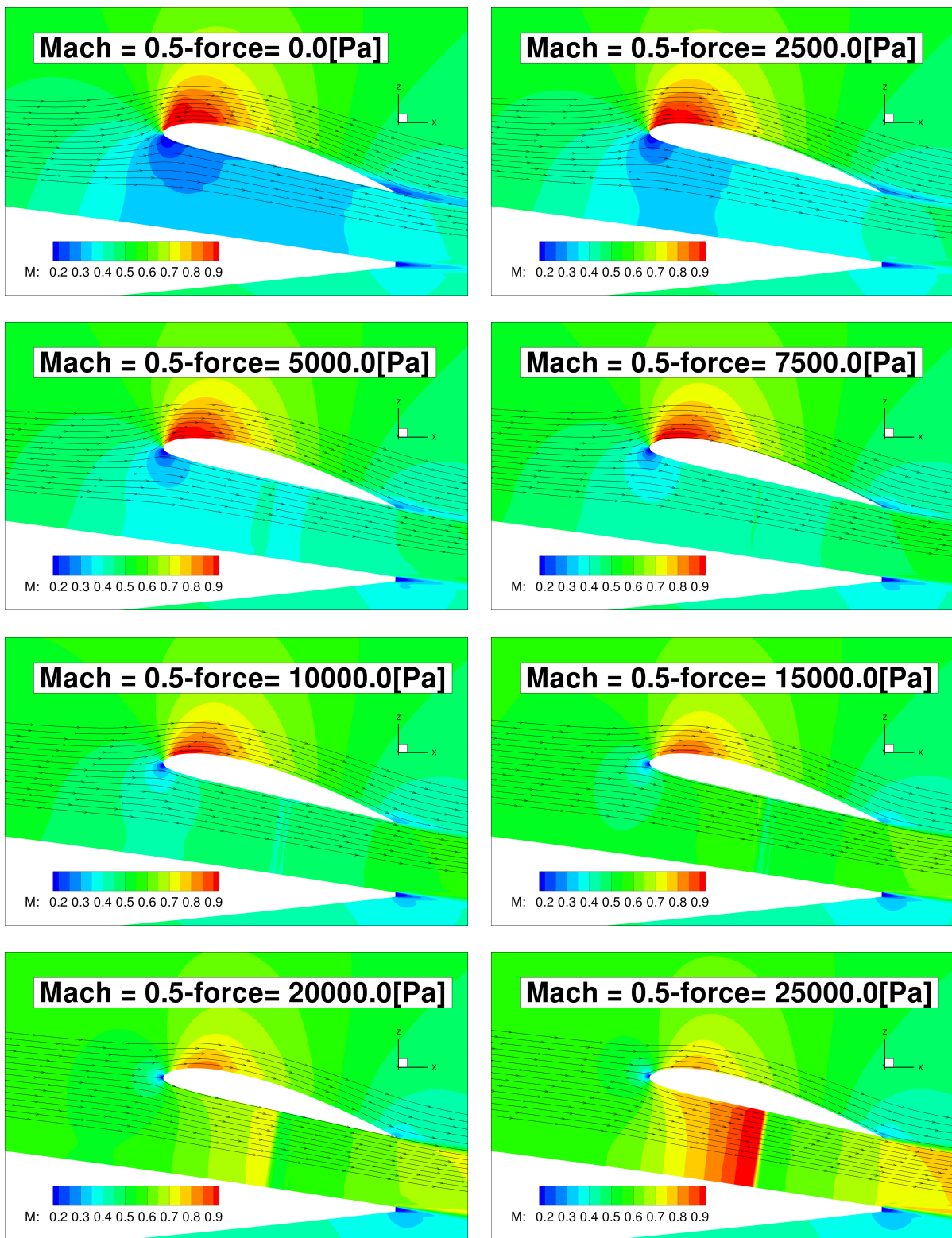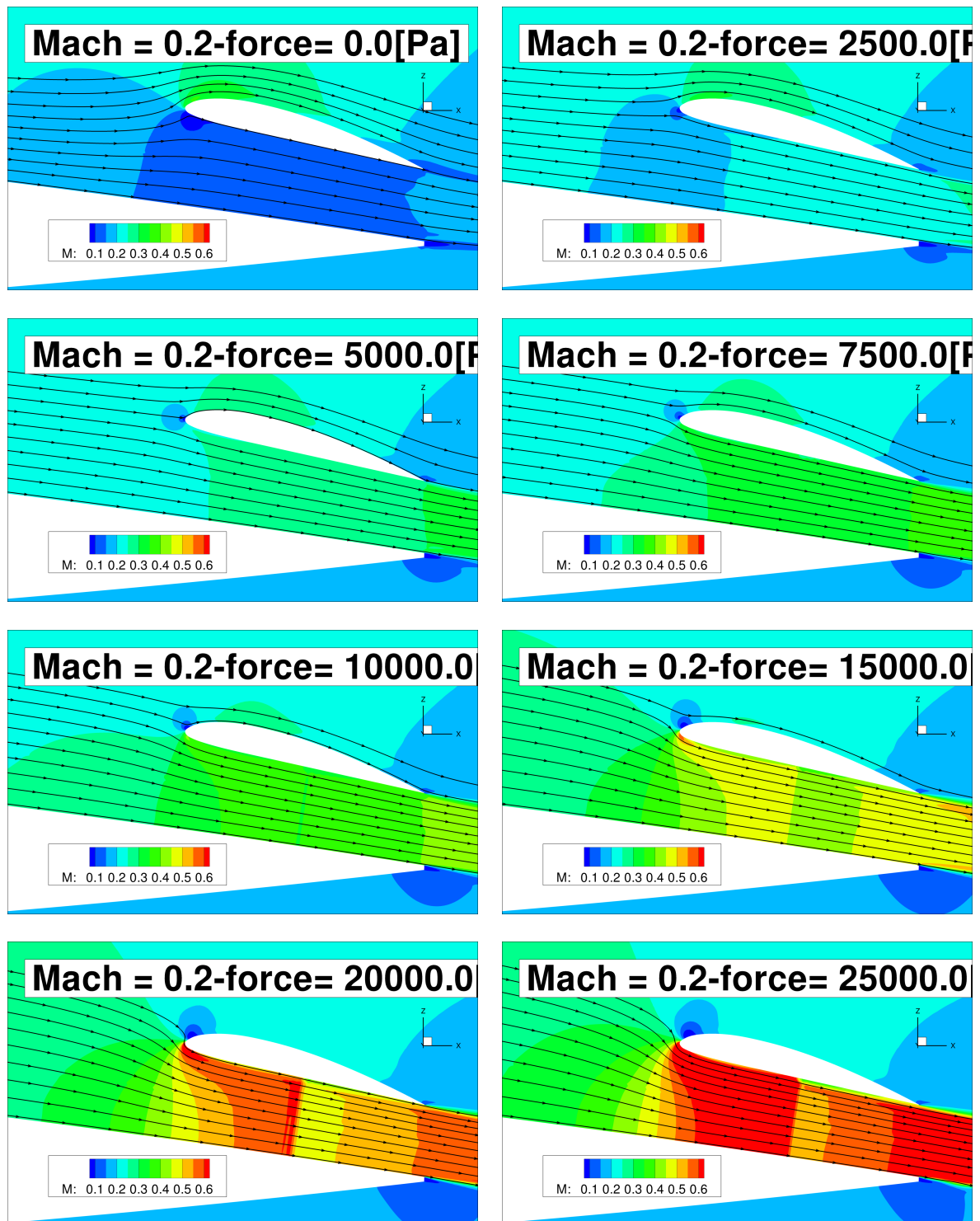
Figure 27: Details of the Mach number in the conduct and around the CLARK Y profile, for $M_0 = 0.2$ and different input forces (from 0.0 to 25000 Pa. $P_0 = 101325$, $T_0 = 300K$

4.2 SIMULATION WITH A NAVIER–STOKES MODEL

The next analysis step has been to study the same model using a more realistic fluid model, i.e. using Navier Stokes equations. The geometry has been kept unmodified (see 2 on page 23), but the mesh has been redone as it is shown in figure 28. The mesh has been adapted to take into account the boundary layer and to respect the classical conditions of $y^+ \simeq 1$ on the walls. Elements number increased from 80000 to 195000. The mesh size is a compromise between a detailed analysis and computational time.
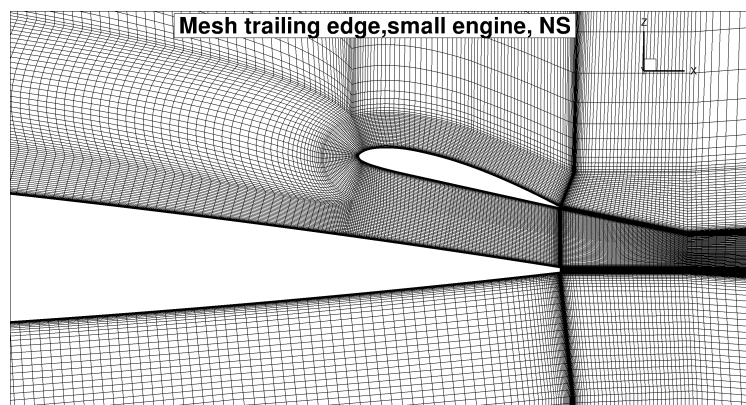
Figure 28: Detail of the mesh around the engine, configuration at trailing edge, Navier stokes computation

In this case, the parametric study is different and it has been split in two different studies. The first focuses on the behaviour at slow Mach Number at take-off/landing conditions. Indeed, as shown in appendix B on page 81, we can imagine a regional aircraft with such a configuration over the wings such that it could take-off at a velocity of M=0.2. We therefore studied the behaviour at different angles of attack, up to stall angles. In table 5 different test cases are shown.

Table 5: Parametric study for trailing edge small engine,Navier Stokes calculation. Polar curve

Parameter	Value
Mach Number []	0.2
Force (per unit of surface) [Pa]	0 1000 2500 5000 7500 10000 15000
Angle of attack [deg]	0° 4° 10° 12° 14° 16° 17° 18° 19° 20° 21° 22° 23° 24°

We eliminated the higher FPR, because it was clear from Euler simulation that for such a geometry,they have shown a non-physical behaviour. Angles of attack have been chosen in such irregular way to study individuate stalling angle of attack and lifts coefficients.

In addition to this, we also prepared a reference configuration made of the NACA 23012 only (without the second profile) that will serve as reference case. The second parametric study that has been considered consists in a study around cruising

configuration (with always reference to B). We do know that the two profiles do not adapt very well to higher Mach number from the previous simulations, but we have performed this analysis, to understand how the model behaves and to understand when this configuration could satisfy the requirements for cruise configuration. In table 6 parameters are shown-

Table 6: Parametric study for trailing edge small engine, Navier Stokes calculation. Cruise study

Parameter	Value
Mach Number []	0.5
Force (per unit of surface) [Pa]	0 500 1000 1500 2000 2500 3000 5000
Angle of attack [deg]	$-1°$ $0°$ $1°$

4.2.1 Results of the low speed study

In figure 29a on the following page lift coefficient curves versus the angle of attack for various forces are shown. The dashed line represents the curve for the NACA23012 profile alone without engine. The stall angle of attack for this configuration is around $16°$ and, for higher forces, it decreases. Considering the reference case (dashed line) and the case at null force (blue continuous line), there is a 5% loss in the maximum lift coefficient, just because of the introduction of the CLARK Y profile. For low forces the pre-stall behaviour of the lift coefficient is non-linear, but for higher forces it becomes much more linear: the aspiration effect overcomes the standard flow circulation around the NACA23012 profile. We can observe the different behaviour during the transition of the stalling angle. The engine completely modify the flow over the upper side causing a much more sudden stall. Indeed the physics of the stall are different from the reference case: in the NACA23012 simulations, stall starts from the trailing edge, whereas in the propulsed configuration, the stalls suddendly develops at the leading edge. The curves confirm that distributed propulsion could be able to (partially) substitute mechanical flaps: lift coefficient at high angle of attack is $\simeq 3$ times the reference value (of the wing profile only).
Finally, we can notice that this model is very sensible to angle variation: for example, at take off/landing configurations the variation of the c_l of a delta alpha=$1°$ is not counterbalanced by doubling the thrust of the engine.

In figure 29d on the next page it is plotted the pitching moment coefficient versus the angle of attack of the model. The reference case with the NACA profile only shows, as expected, that the pitching moment is independent from angle of attack (up to $10°$) . The model is generally stable (the c_m is negative) and for low angle of attack it is almost constant, but we do put on evidence that this behaviour is far from being a good one. At high-lift configuration, without the engine turned on, the coefficient becomes positive and therefore possibly unstable.
In the figures 30 and 31 on page 40 a selection of the results are plotted. Firstly, it is put on evidence the boundary layer that is developed around the profile and
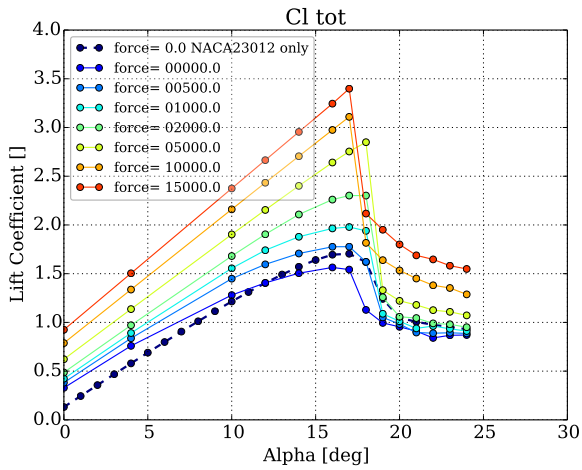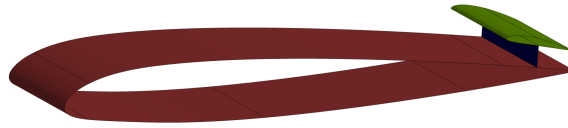
(a) Lift coefficient
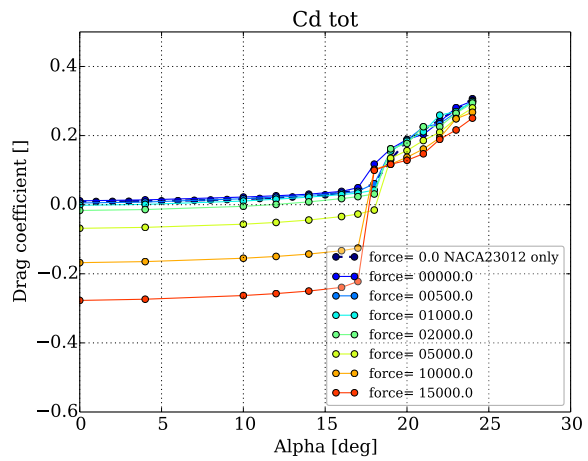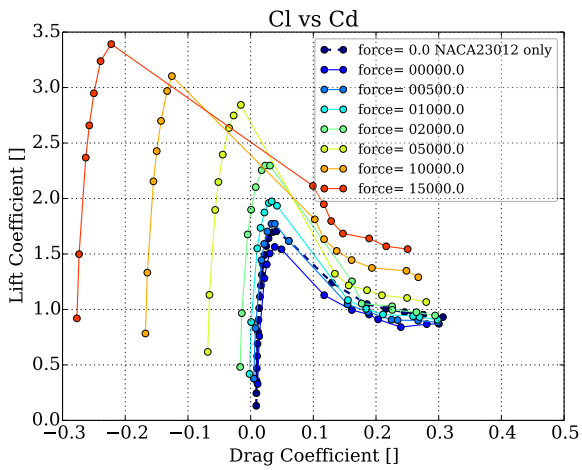
(b) Drag coefficient

(c) Lift coefficient versus drag coefficient, iso-forces
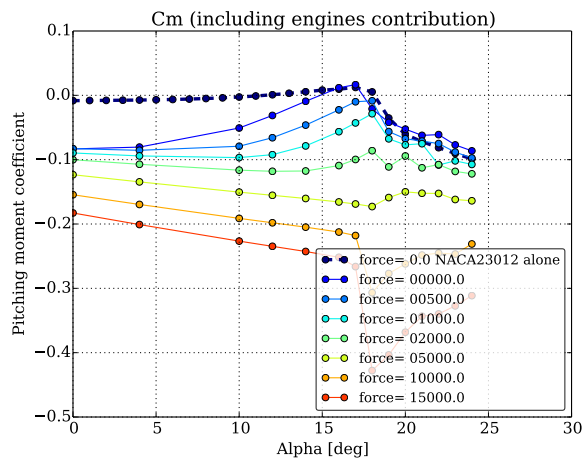
(d) Pitching moment coefficient

Figure 29: Parametric study of the lift and drag coefficients for different forces and angle of attack. Mach=0.2, Navier Stokes simulation. The dashed line represents the case where only the NACA23012 is simulated

that is ingested by the engine. The two last configurations of the first series of figure correspond to two post-stall configurations. In the second series of figures the Mach field is shown.
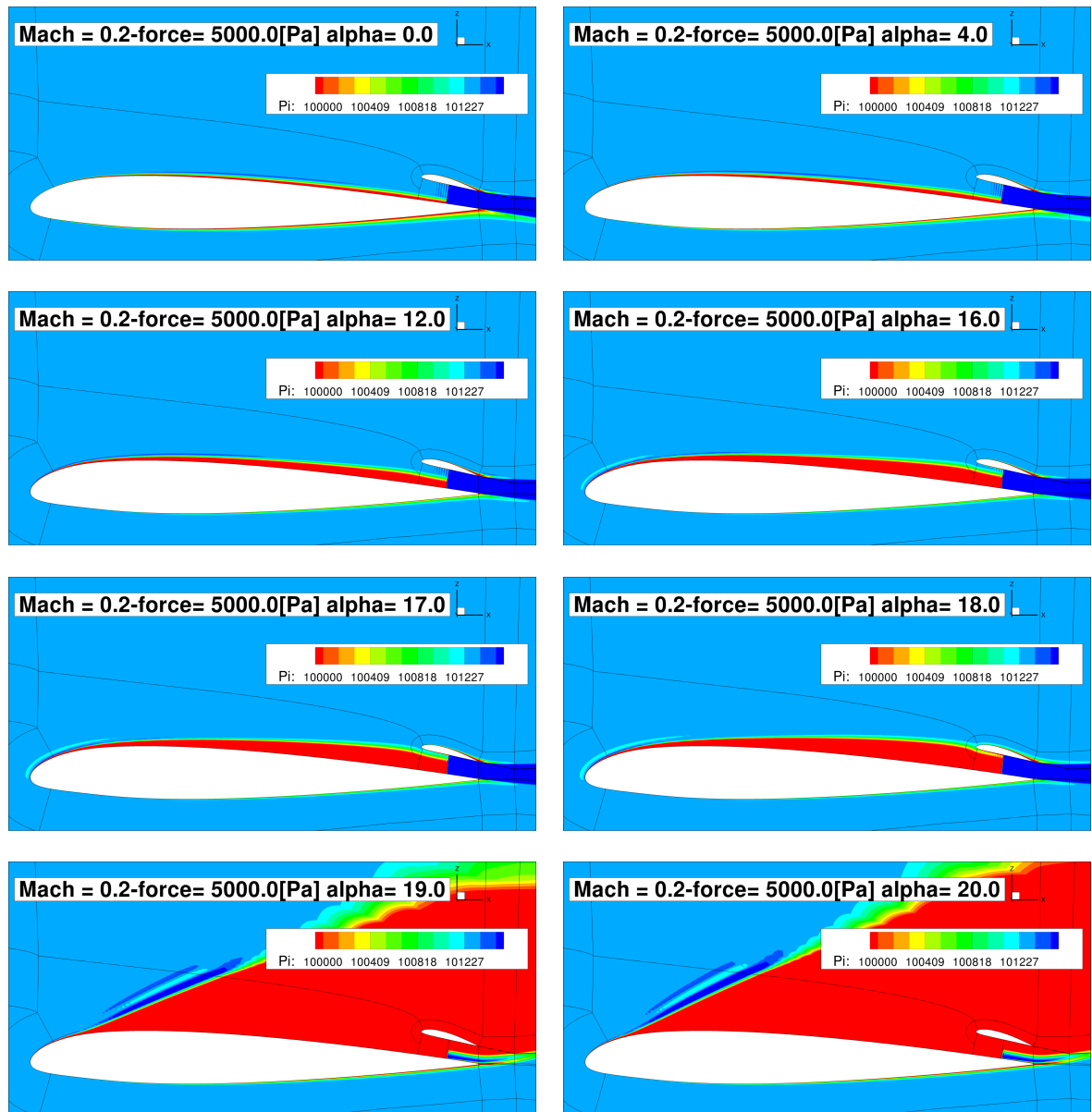
Figure 30: Details of the total pressure around the model for a fixed input force and different angles of attack. $P_0 = 101325$, $T_0 = 300K$
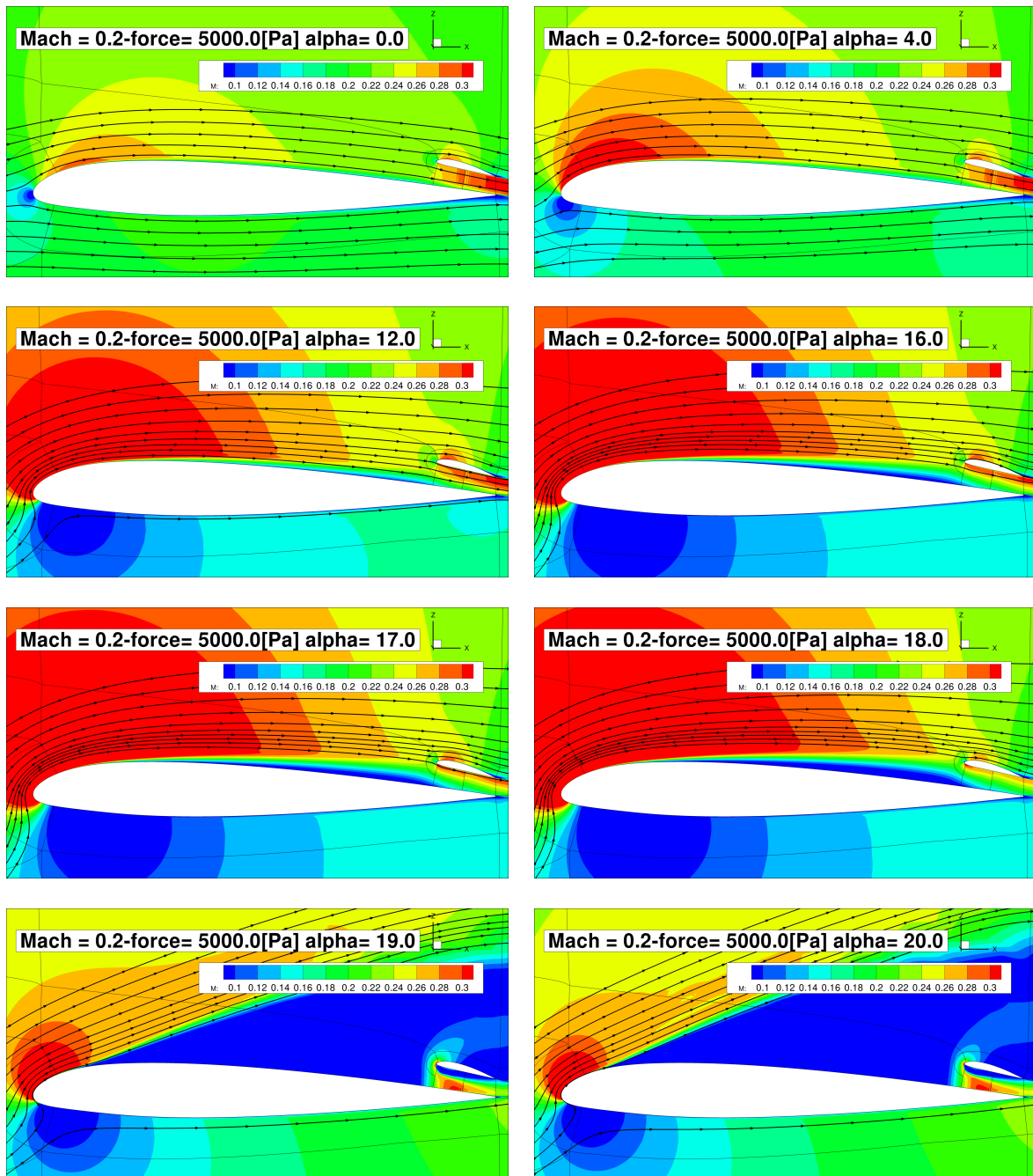
Figure 31: Details of the Mach number around the model for a fixed input force and different angle of attack. $P_0 = 101325, T_0 = 300K$

4.2.2 Results of the cruise speed study

The parametric analysis at cruise speed (Mach number=0.5) has been done to identify the"ideal" parameters for an ideal configuration. Referring to the hypothesis that we have done in appendix B, we would like to identify parameters such that $c_L = 0.5 \simeq 0.6$ and such that $c_D \simeq 0$ or negative . The profiles that characterize this configuration are not adapted to Mach=0.5, and calculations converged with more difficulty. In figures 32 we can identify a cruise point for a force (per unit surface) = $5000 Pa$, $\alpha = 1°$ (equivalent to an FPR=$\simeq 1.05$, for which $c_D \simeq 0$, instead of the design point of FPR=1.1,as expected). It is interesting to notice that drag coefficients almost insensible to the variation of α for low angles of attack.

(a) Lift coefficient

(b) Drag coefficient

(c) Pitching moment coefficient

Figure 32: c_L,c_D e c_M vs input forces at cruise configuration (Mach number=0.5) for different angle of attack

4.2.3 Integral balances around the actuator disk condition

In this section we will briefly show an attempt of calculating momentum and energy balances around the actuator disk. This analysis suffers of two significant problems. First, the integration of the engine in the airframe limits the capability to estimate the power that the engine has generated, the second, the non-physical oscillations generated by the actuator disk boundary condition.

Firstly, a momentum analysis has been carried out similarly to what has been described in section 3.2.1 on page 15. In this case, we have neglected the viscous efforts over the two surfaces. In figure 33a we can observe the result of the momentum balance versus the input force (always expressed per unit surface). As already noticed in the analysis of the AD condition, the CFD code slightly overestimates the input force. The behaviour is similar for all different angle of attack, except those corresponding to a post-stall configuration. Indeed, further observations show that across the actuator boundary surface a recirculation zone has developed, that seems to prevent the boundary condition to work properly.

(a) Momentum balance versus imposed input forces

(b) Power balance over the boundary condition
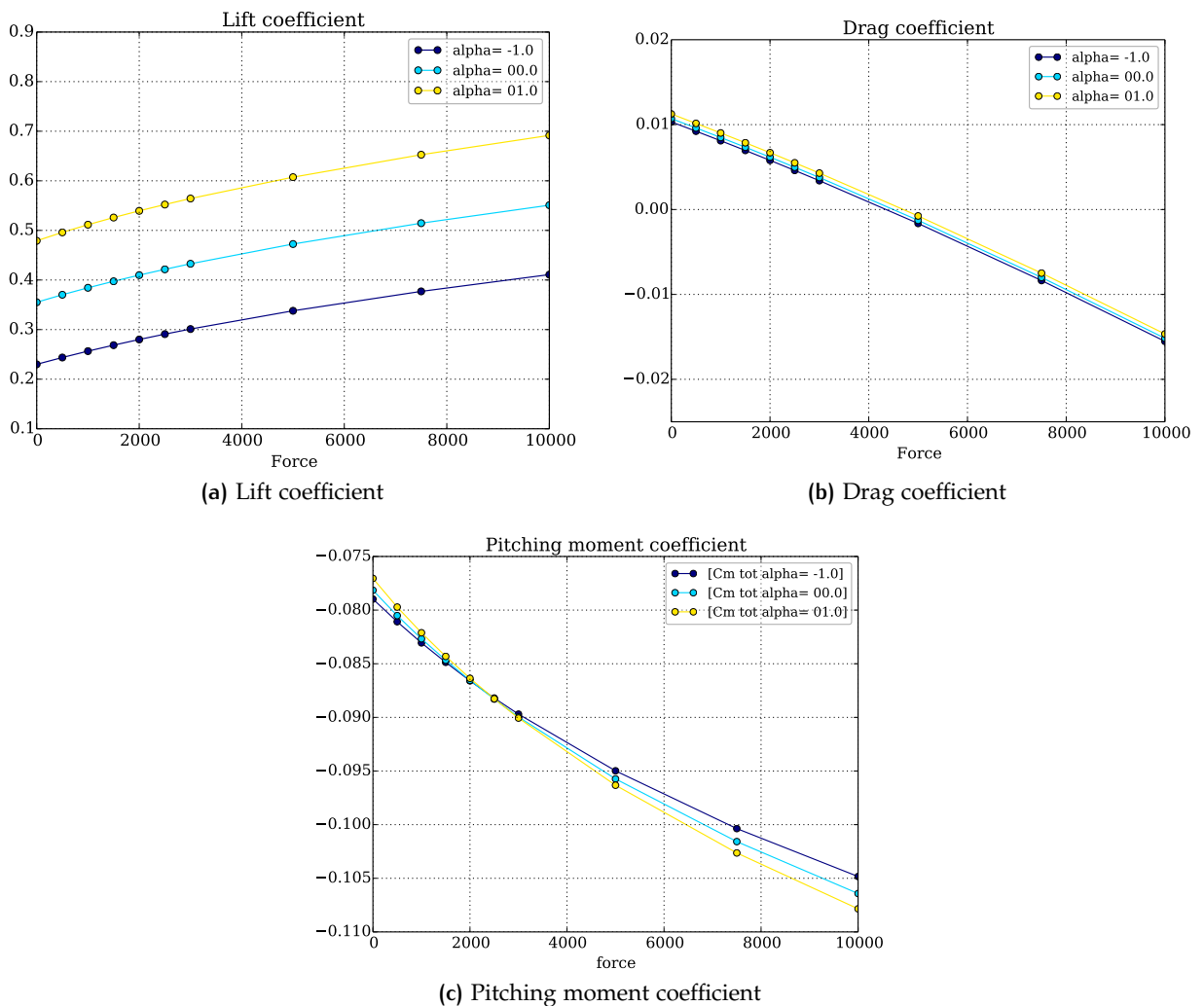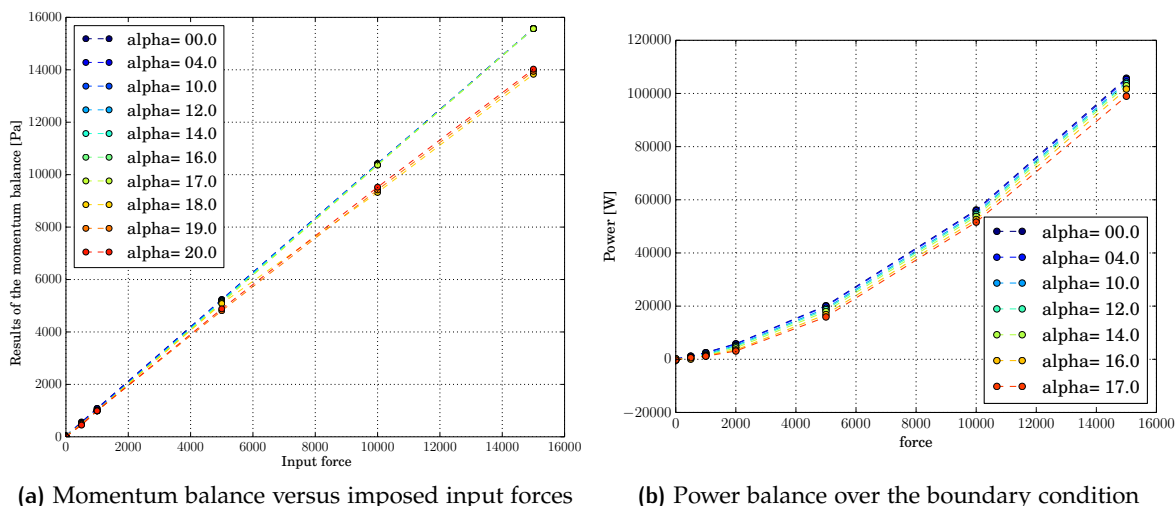
Figure 33: Integral balances around boundary disk condition, trailing edge configuration

Secondly, an energy balance, following the balance equation 32 on page 15 has been carried out to estimate the theoretical power that an imaginary engine would transmit to the fluid through the actuator disk. (We remind that, for simplicity, it has been neglected the contribution of the heat flux and of the viscous tensors stresses). In figure 33b the result of this balance is shown. We note that there is a slight incidence effect and the behaviour is almost quadratic. These values are in the same order of magnitude of real-engine (with an obviously scale effect that has to be considered).

It is necessary to put on evidence that the calculation of this energy balance is critical because of the non-physical oscillatory phenomena that are generated by the boundary condition. Indeed, the oscillatory phenomena are especially present in energy-related variables, such as the total pressure, or the total energy. So, whereas

all momentum balances are almost acceptable, even taking into consideration the oscillation, the integration of the oscillation of the total energy causes some errors that could result in negative power. A solution is to integrate as far as possible from the boundary conditions (i.e. let the oscillations dissipate), but in this case, the term of the dissipative energy due to the viscous effort could not be negligible. For the calculation shown in figure 33b a compromise solution has been adopted, and the stalled cases (angle of attack greater than 17°) have been excluded.

More generally, the estimation of the power generated by the boundary condition is difficult because is it actually impossible to tell apart the thrust and the drag generated by the engine, the drag generated by the wing and the induced drag of the boundary layer (see section 1.2.3 on page 4).

Finally, we tried to estimate the BLI effect, through the definition of the following quantity:

$$\eta_b = \frac{\vec{F} \cdot \vec{V_{av}}}{\mathbb{P}} \tag{48}$$

where $\vec{F}$ is the force resulting from the momentum balance, $\vec{V_{av}}$ is the surface average of the velocity over the boundary disc condition and $\mathbb{P}$ the power as described in equation 32 on page 15. This represents an efficiency of the boundary layer ingestion. As already said, being the calculation of the power critical, this calculation is just a rough attempt to understand the behaviour of the boundary layer ingestion in terms of energetic performances. In figure 34 this quantity is shown versus the input force. The estimation is therefore restricted for this case to the lower angles of attack. The value of η is not of absolute interest, because of the problem of the calculation of the power, due to the boundary condition and because of the strict integration of the engine over the airframe. But, the trend of the curve and the position between them are significant. Indeed, we could qualitatively notice that, for a fixed force (or equivalently, FPR), the efficiency is higher for higher angles of attack, that is equivalent to say that the efficiency is higher for thicker boundary layers. Indeed, the engine ingest some air at lower velocity leading to an increase of the propulsive efficiency that we have defined in chapter 1 on page 1.

(a) Efficiency η_b versus the input force for different angles of attack.

(b) Efficiency η_b versus the input force for different angles of attack.zoom around cruise point.
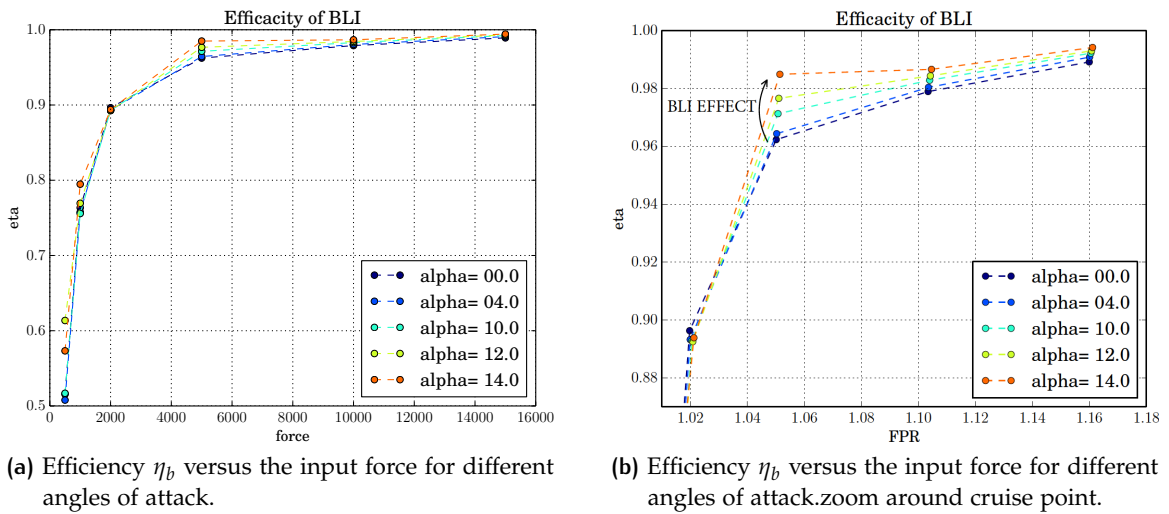
Figure 34: Efficiency η of the small engine, trailing edge configuration

4.3 LEADING EDGE ENGINE CONFIGURATION

In this section we will present the results of the CFD analysis of the model that has been presented in section 3.4 on page 23. It is the sectional view of a wing with the engine positioned aligned with the forward part of the wing. The model is show in figure 18 on page 24. The mesh of this configuration has around 270000 elements and it is shown in figure 35. The boundary conditions have been kept unchanged (see 3 on page 27). Again, as for the previous model, we studied two

Mesh leading edge configuration
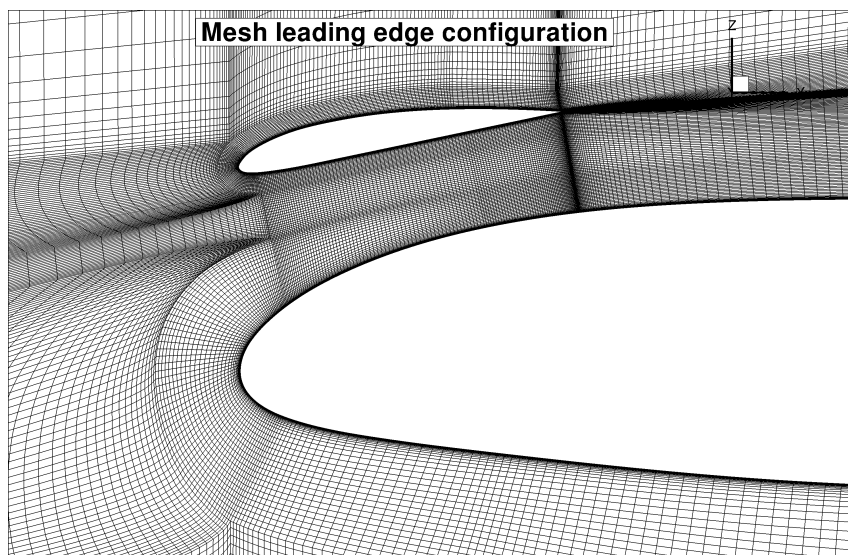
Figure 35: Detail of the mesh around the configuration with the leading edge engine

groups of simulation, one at low Mach number, considering a study of model at different angles of attack. This one is shown in table 7. The second study corresponds to a study around cruise configuration, that is shown in table 8 on the next page.

Table 7: Parametric study for forward engine,Navier Stokes calculation. Low speed study

Parameter	Value
Mach Number []	0.2
Force (per unit of surface) [Pa]	0 1000 2500 5000 7500 10000 15000
Angle of attack [deg]	0° 4° 10° 12° 14° 16° 17° 18° 19° 20° 21° 22° 23° 24°26°28°30°

The main characteristic that differentiates this configuration from the last one is that the boundary layer cannot develop enough to have a significant impact over the performance of the aircraft. The engine does not ingest the boundary layer.
In addition, the presence of the CLARK Y profile could have a beneficial effect over the stall angle for this configuration. Indeed, its positioning relative to the NACA 23012 could be assimilable to that of some kind of leading edge slats (even if this is not the primary objective of our device, being an engine).

Table 8: Parametric study for forward Navier Stokes calculation. Cruise study

Parameter	Value
Mach Number []	0.5
Force (per unit of surface) [Pa]	0 500 1000 1500 2000 2500 3000 5000 7500 10000
Angle of attack [deg]	$-1°$ $0°$ $1°$

A third substantial difference with respect to the first configuration is the fact that the conduct is convergent-divergent: it is expected that the velocity field at the boundary condition actuator disk will be higher.

4.3.1 Results for the low speed study

In this section we will present the result for the parametric study at $M = 0.2$, i.e. as usual, for an imaginary take-off situation.

In figure 36 on the following page lift and drag coefficients are shown for alpha varying from 0° to 30° and for different forces (from 0 to 10000 Pa). In figure 36a on the next page the different behaviour of the lift coefficient can be observed: indeed, as expected the stall angle is higher (especially for very high forces) and the stall is much less violent, and much more similar to the behaviour of the NACA23012 alone. In that case and in all cases of this configuration, the stall starts from the trailing edge, whereas for the preceding configuration the stall develops from the leading edge. The engine in this case operate similarly to a slat device, in addition to the fact that it energizes the fluid flow around the upper side of the system. It is interesting to notice that, as can be seen in figure 38 on page 48 the stall is almost unnoticeable and that the fact that the CLARK Y is completely stalled does not influence the fluid flow around the engine. In this configuration, we can observe the Coanda effect that redirects the fluid flow around the upper side of the wing profile (see figure 37 on page 47). In figure 36 on the following page we notice how the slat redirect and re-accelerate the flow around the system. The drag coefficient shows in figure 36b on the next page a very similar behaviour to the reference case for lower forces. The pitching moment coefficient show a very stable (and negative, ie naturally stable) behaviour.
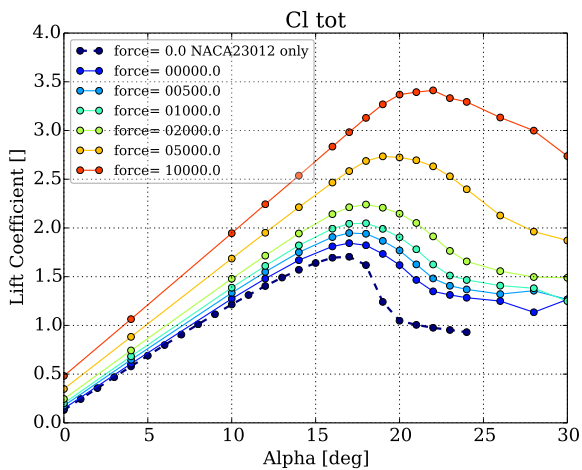
(a) Lift coefficient
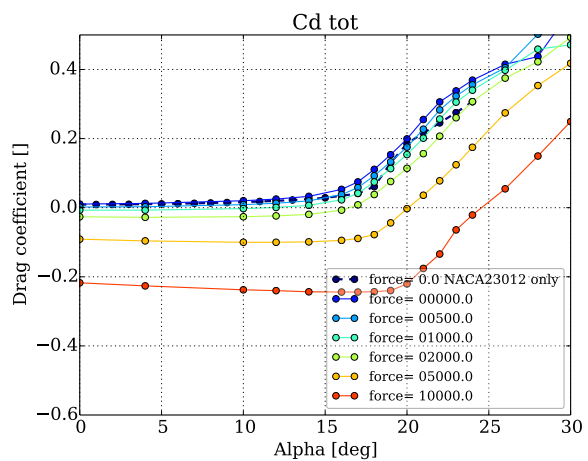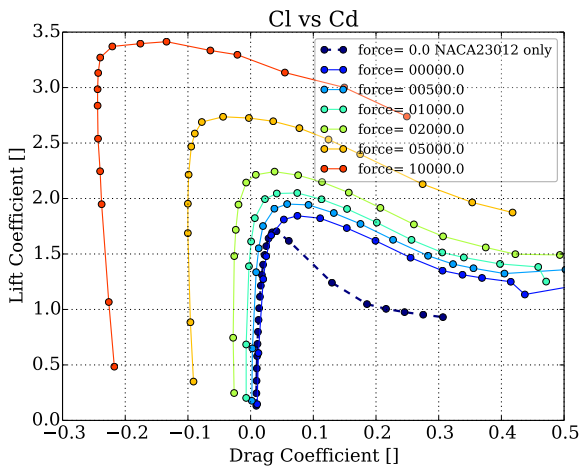
(b) Drag coefficient

(c) Lift coefficient versus drag coefficient, iso-forces
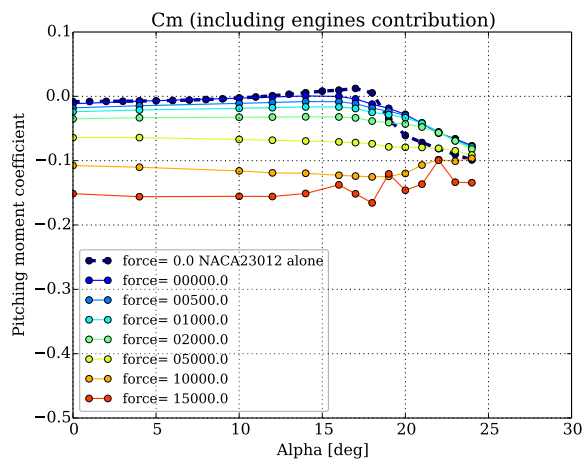
(d) Pitching moment coefficient

Figure 36: Parametric study of the lift and drag coefficients for different forces and angle of attack. Mach=0.2, Leading edge configuration. The dashed line represents the case where only the NACA23012 alone is simulated
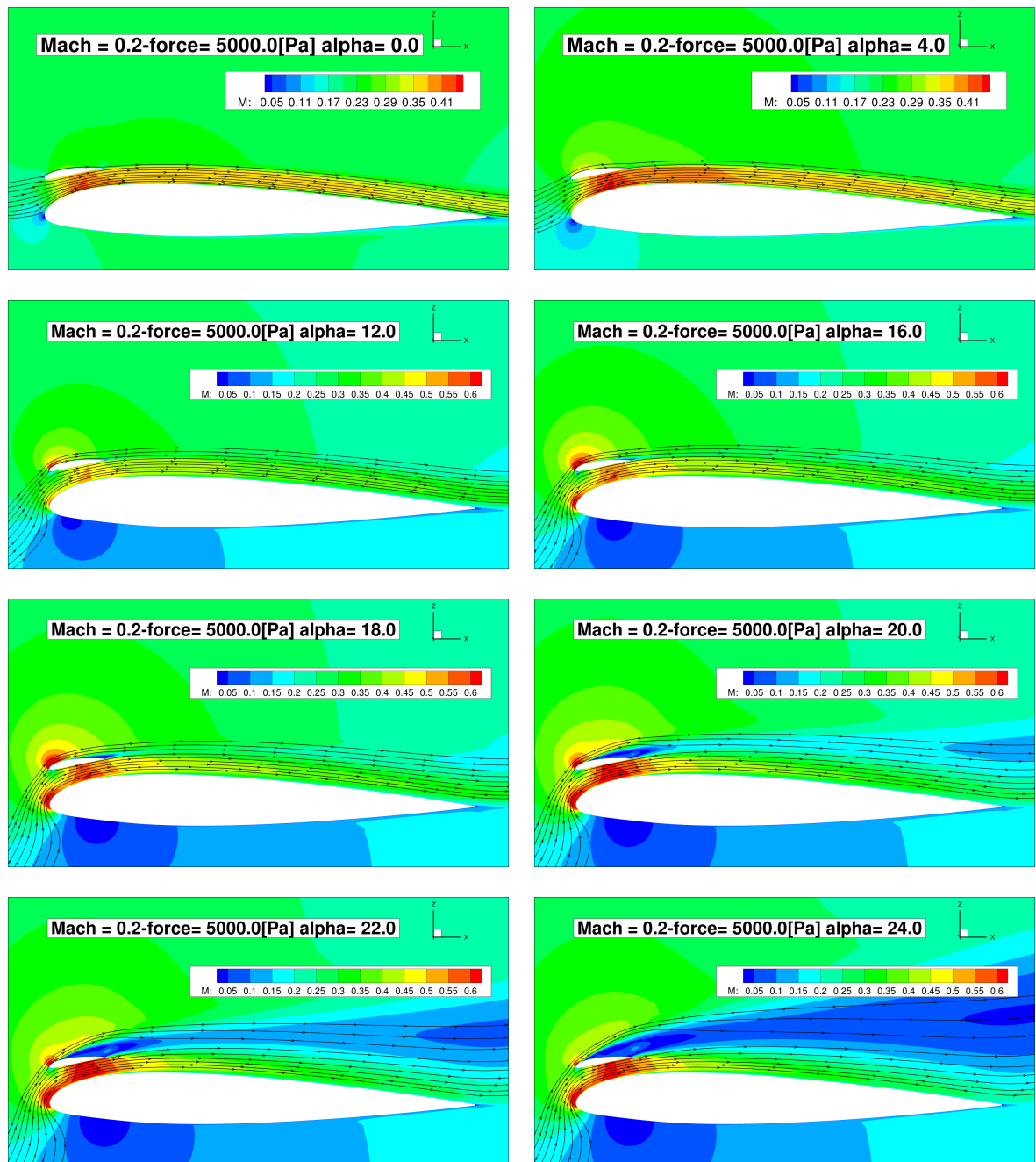
Figure 37: Details of the Mach number around the model for a fixed input force and different angles of attacks. Forward engine, $P_0 = 101325$, $T_0 = 300K$
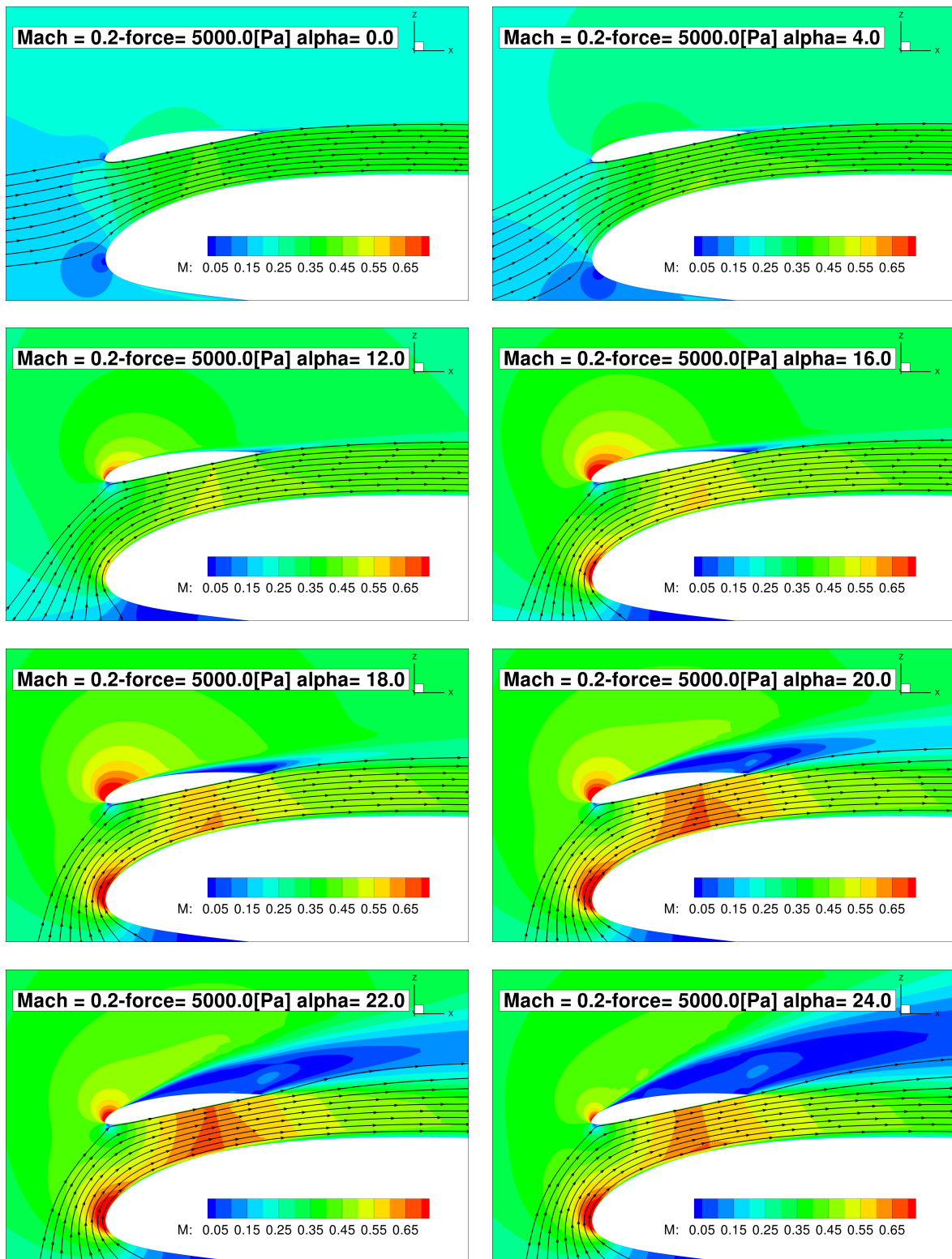
Figure 38: Details of the Mach number around the model for a fixed input force and different angles of attack. Forward engine, $P_0 = 101325$, $T_0 = 300K$

4.3.2 Results of the cruise speed study

In figure 39 the results of the cruise analysis are shown. First of all, this config-
uration has shown a much better behaviour in term of convergence and stability
of the solution, that let us simulate many more different configuration. In the
figure we can identify an "ideal cruise point" for force (per unit surface)=3000Pa,
$\alpha = 2° - 3°$ for which the drag coefficient is zero. It is very interesting to put on
evidence that the pitching moment coefficient in this configuration is almost zero
(figure 39c, please note that the y-axis scale is different from the scale of the equiv-
alent figure for the others configuration) and with a negative slope. This wing
therefore surely has an advantage in term of stability in cruise configuration.

(a) Lift coefficient

(b) Drag coefficient

(c) Pitching moment coefficient
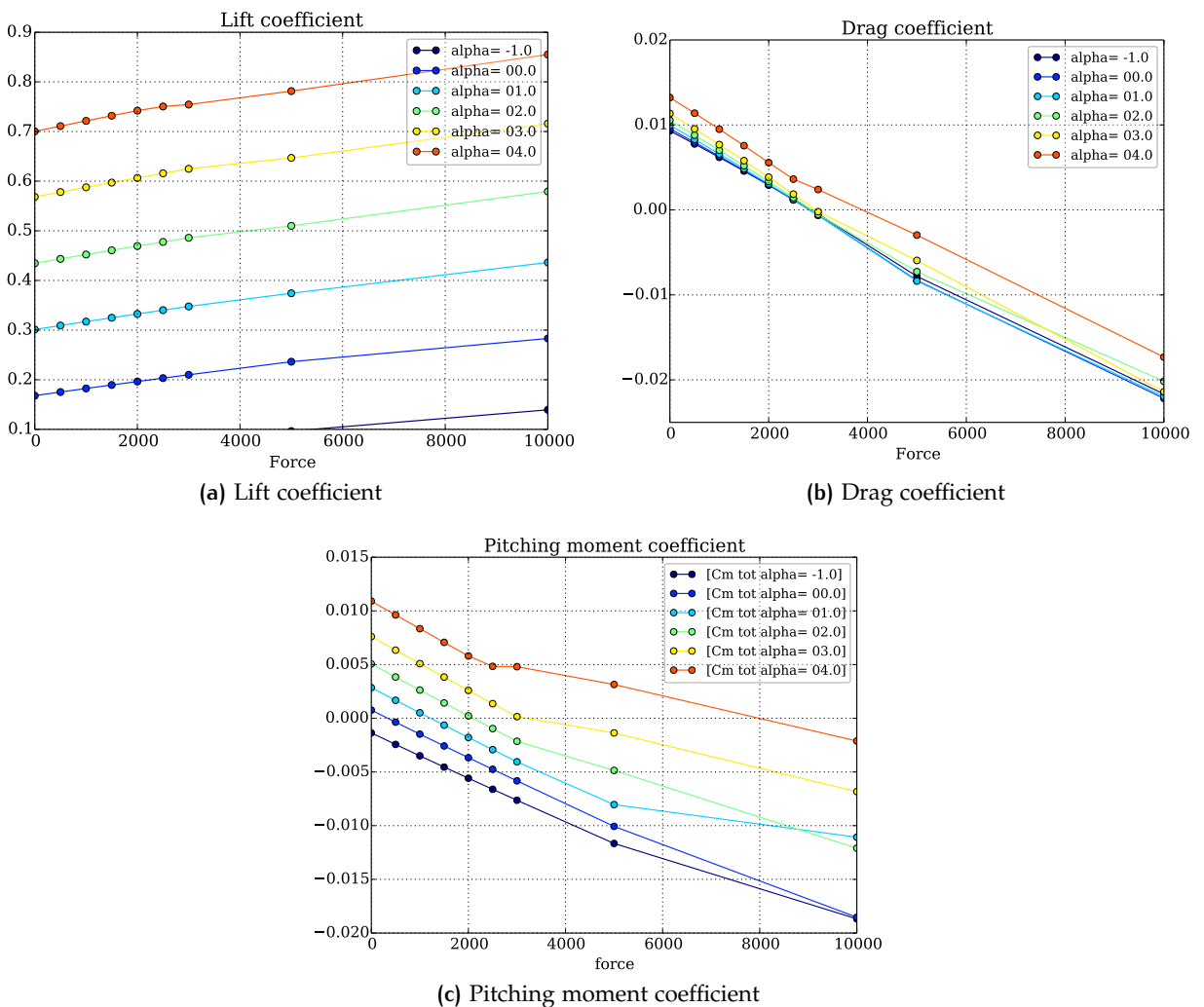
Figure 39: c_L,c_D e c_M vs input forces at cruise configuration (Mach number=0.5) for different angle of
attack

4.3.3 Comparison with the trailing edge engine

The leading edge engine has been designed in order to keep the surface area equal to that of the trailing edge configuration, but, because of the geometry of the leading edge, the conduct is convergent-divergent, whereas in all other configuration is convergent only (and much less convergent). In figure 40a we observe that the flow velocity crossing the actuator disk surface is more than double for the leading edge engine. The fluid flow must accelerate to turn around the leading edge of the wing profile, especially for higher angles of attack, where the stagnation point is much lower. In addition to this, the shape ratio between the entry surface and the actuator disk surface is higher than in trailing edge configuration, so the flow is further accelerated. This significant difference explains the different behaviour in figure 40b, where the efficiency that we have defined in 48 on page 43 is shown. The efficiency of the leading edge engine decreases for increasing angle of attack: in this configuration, as expected, no gains due to BLI ingestion can be achieved. Moreover, for increasing force, the efficiency falls down. The behaviour is substantially opposite to that of the trailing edge configuration.

(a) Velocity at the actuator disk surface: traling edge versus leading edge engine

(b) efficiency η_b versus the input force for different angles of attack.zoom around cruise point.
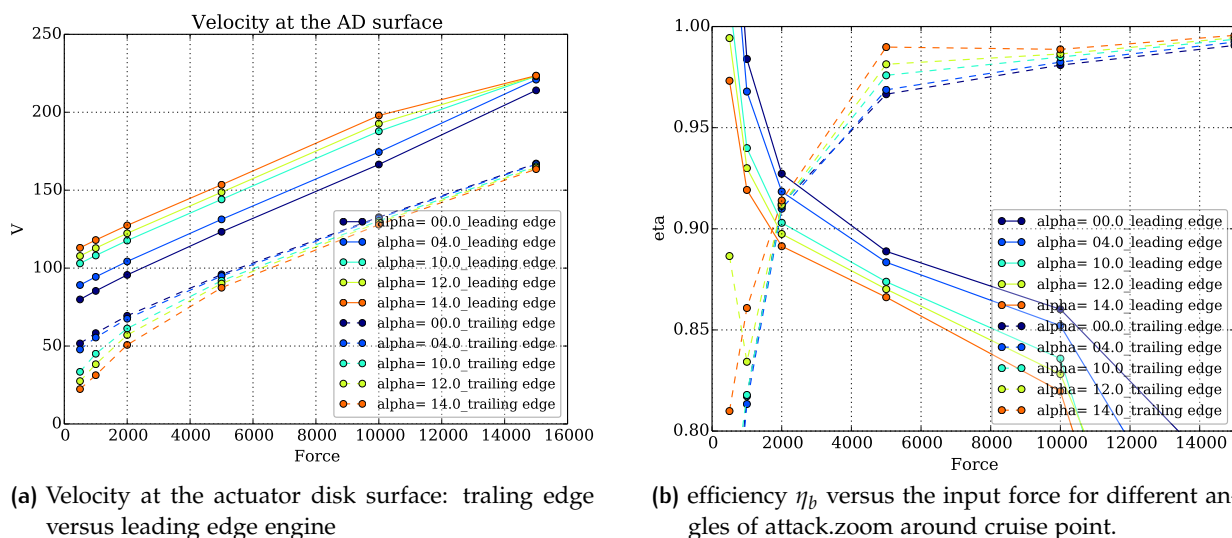
Figure 40: Comparison of velocity and efficiency between leading edge engine and trailing edge engine

We compare now the pure aerodynamic performance in take-off configuration (i.e. at Mach=0.2) between the two models. It can be observed that the leading edge configuration produces a lower total lift coefficient (also because of the orientation of the engine) for lower angles of attack, whereas the maximum lift coefficient are higher, because the wing stalls later. The leading edge configuration seems to have an advantage: the loss in lift coefficient for low angles is a good compromise for higher maximum lift coefficients and for a better post-stall behaviour. In a certain sense, this dualism in terms of behaviour could be approximated to the dualism of leading edge devices, like slats and trailing edges devices. This can be also observed compared figure the Cl-Cd curves in figure 36c on page 46 and 29c on page 38.

Because of the different performances of the two configurations, it is significant

to compare lift and pitching coefficient such that $c_D \simeq 0$ (at least for low angles of attack). In figures 41a we can observe lift coefficients of the two configurations, along with the reference case. As already put in evidence we can notice a trade off consisting in a lower lift coefficient for lower angles of attack for a better post-stall behaviour. From figure 41b it is clear that the leading edge configuration has a definitive advantage in terms of pitching moment stability. It is generally much lower, and, in addition, the curves are much more linear and constant: the system in this case is more stable than the trailing edge configuration. Indeed, the engine is forward the aerodynamic center of the system, reducing (i.e. less negative) the total pitching moment.
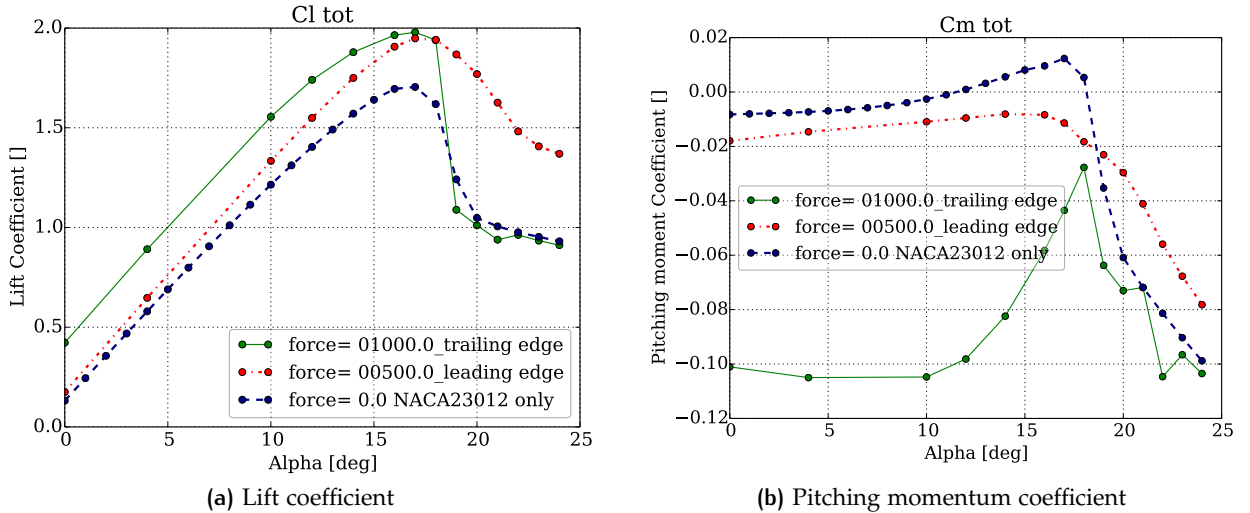

(a) Lift coefficient

(b) Pitching momentum coefficient

Figure 41: Comparison of lift and pitching coefficient of the two configuration at $c_D = 0$

The performance at cruise speed confirms the advantage that the leading edge device possesses over the trailing edge configuration (in terms of aerodynamics properties). Indeed, pitching moment coefficient is even lower and more constant with respect to the calculation at Mach=0.2 and the lift coefficient for the same angle of attack is essentially higher for the leading edge configuration.

It is necessary to highlight that an engine set in the forward part of a wing arises a set of problems that are not taken into account in an aerodynamic analysis. For example, the present formulation of the actuator disk condition does not take into account the heating phenomena: in a real engine the exiting flow would be much hotter, that could make necessary an isolating layer over the wing, which adds weight and therefore making this configuration possibly less envisageable. However, in a very long term perspective, the use of electric propulsive system could eliminate this problem.

To resume, if we focus only to pure aerodynamics performances, the leading edge configuration possesses a definitive advantage over the trailing edge device, but, there are some drawbacks that are not strictly related to the aerodynamics. Firstly, the efficiency we have defined seems to give an advantage to the trailing edge configuration (because of the boundary layer ingestion), even if we recognize that this kind of analysis is inherently limited. Secondly, the thermal-structural problems could be not so negligible, without considering electric propulsion.
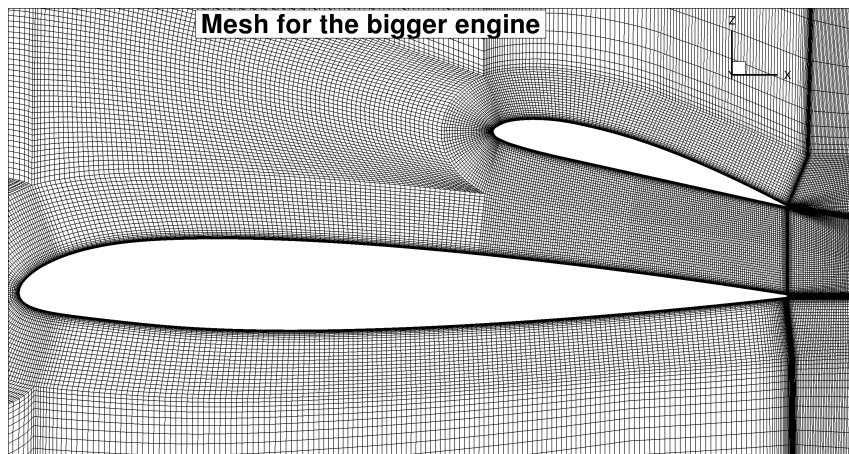
Figure 42: Detail of the mesh around the configuration with the bigger engine

4.4 A BIGGER ENGINE

In this section we present the 2D model that we have shown in section 3.5 on page 24. The topology is substantially equivalent to the first model, whereas in this case the engine diameter is three times the original one, along with the chord of the CLARK Y profile. This bigger engine has been sized to fit some realistic requirement that a regional airliner equipped of such engines should satisfy and to study the size effect over the configuration. The model is shown in figure 19 on page 25 and the mesh, that consists of 290000 points, as shown in figure 42. As usual, two parametric analysis have been done, they are shown in the table 9 and 10.

Table 9: Parametric study for trailing edge big engine, Navier Stokes calculation. low speed study

Parameter	Value
Mach Number []	0.2
Force (per unit of surface) [Pa]	0 1000 2500 5000 7500 10000 15000
Angle of attack [deg]	0° 2° 4° 6°8° 10° 12° 13° 14° 16° 17° 18° 19° 20°21°22°23°24°

Table 10: Parametric study for trailing edge big engine, Navier Stokes calculation. Cruise study

Parameter	Value
Mach Number []	0.5
Force (per unit of surface) [Pa]	0 500 1000 1500 2000 2500 3000 5000
Angle of attack [deg]	−1° 0° 1°

4.4.1 Results for the low speed study

The result for the first parametric study are shown in figure 43 on the following page, as usual in terms of the different coefficients. In this case, several cases have been excluded from the graphics because, convergence of the different simulations were much more difficult to obtain. From the first sub-figure we do note that the introduction of a bigger engine implies the decrease of the stall angle (that is located at 15-16 °. Lift coefficient in this configuration is very high because of the fact that we tripled the surface, therefore tripling the total force generated by the actuator disk. Comparing the dashed line of the NACA23012 to the curve at zero force (per unit surface), we notice that the presence of the CLARK Y degrades the behaviour of the system: the maximum lift coefficient is lower and corresponds to a lower angle of attack. The size (chord) of the engine is, in this case, comparable to the size of the wing and does not integrate well with it. The loss in pure aerodynamic is compensated by the presence of the engine: indeed, the drag coefficient (that in this case could be called, "thrust" coefficient) is very low (very negative) because of the big surface of application of the boundary condition.

The pitching moment coefficient shown in figure 43d on the next page is extremely negative, even when the engine is turned off, showing the intrinsic instability of this configuration. Again, the presence of the nacelle profile, in its size, degrades the performance of the configuration. According to the appendix B on page 81 this configuration corresponds to the first iteration of a sizing process where we have supposed the maximum lift coefficient to be 2.5. It is evident that this hypothesis is largely satisfied. In a realistic design process the following iteration would be characterized by a smaller surface area (because take-off Mach number would be smaller). It is clear that this configuration is an upper bound in the design process because the thrust generated by the engine is clearly too high for this 2D configuration. The realistic engine size should be comprised between the size of this configuration (12 cm) and the size of the first one (4 cm). In figure 44 on page 55 we observe a detail of the boundary layer that is ingested by the engine in this configuration. In figure 45 on page 56 there is a global view of the fluid flow around the different cases. It is interesting to note how, in the last two figures, the wing is stalled (that is confirmed by the values of the lift coefficient) but, at the same time, the engine is able to keep the flow "almost attached" to the wing.

Post-stall angles of attack are not shown in the figures because of convergence problems of such configurations. They should have been computed using unsteady RANS (URANS).
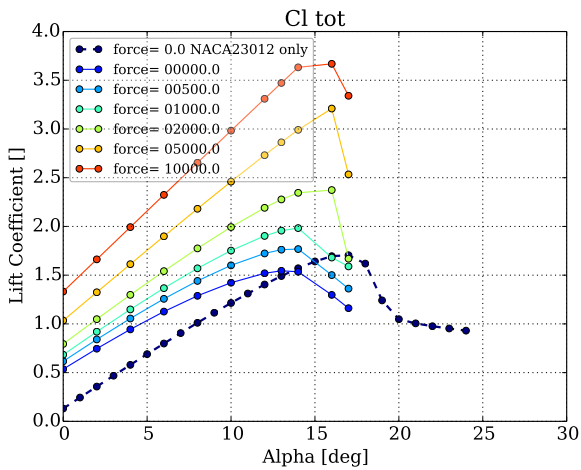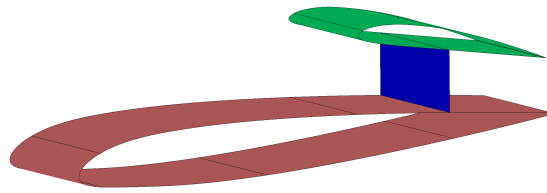
(a) Lift coefficient
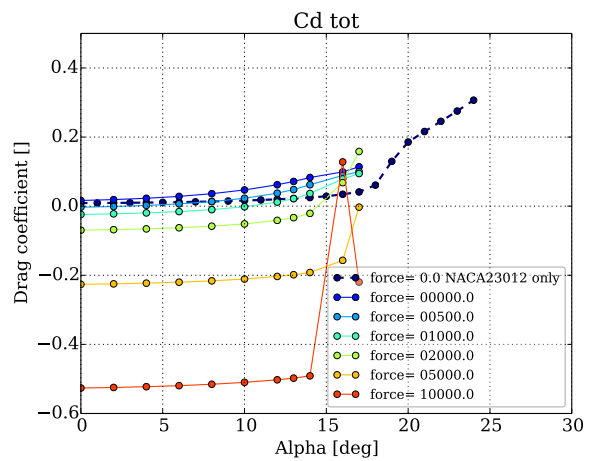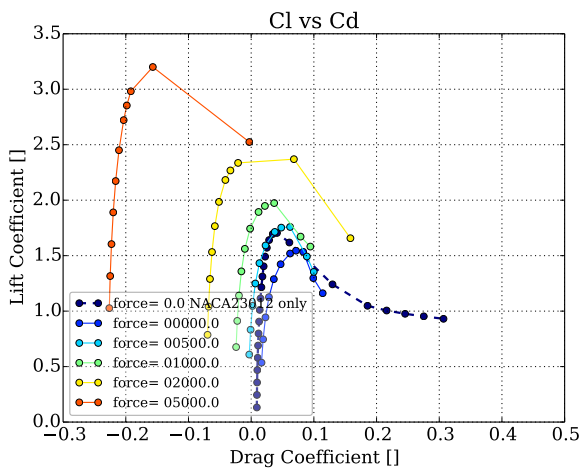
(b) Drag coefficient

(c) Lift coefficient versus drag coefficient, iso-forces
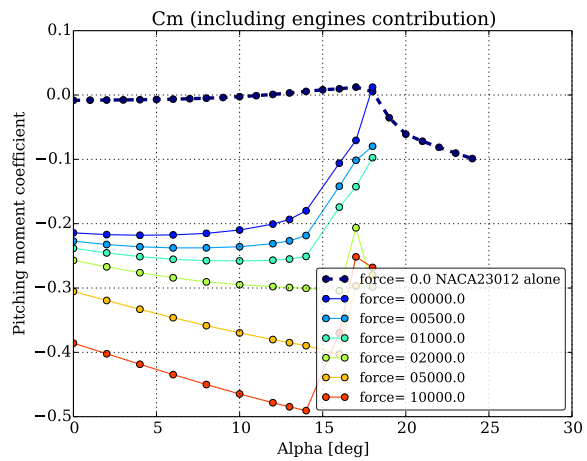
(d) Pitching moment coefficient

Figure 43: Parametric study of the lift and drag coefficients for different forces and angles of attack. Mach=0.2, Bigger engine in the aft part of the wing. The dashed line represents the case where the NACA23012 alone is simulated
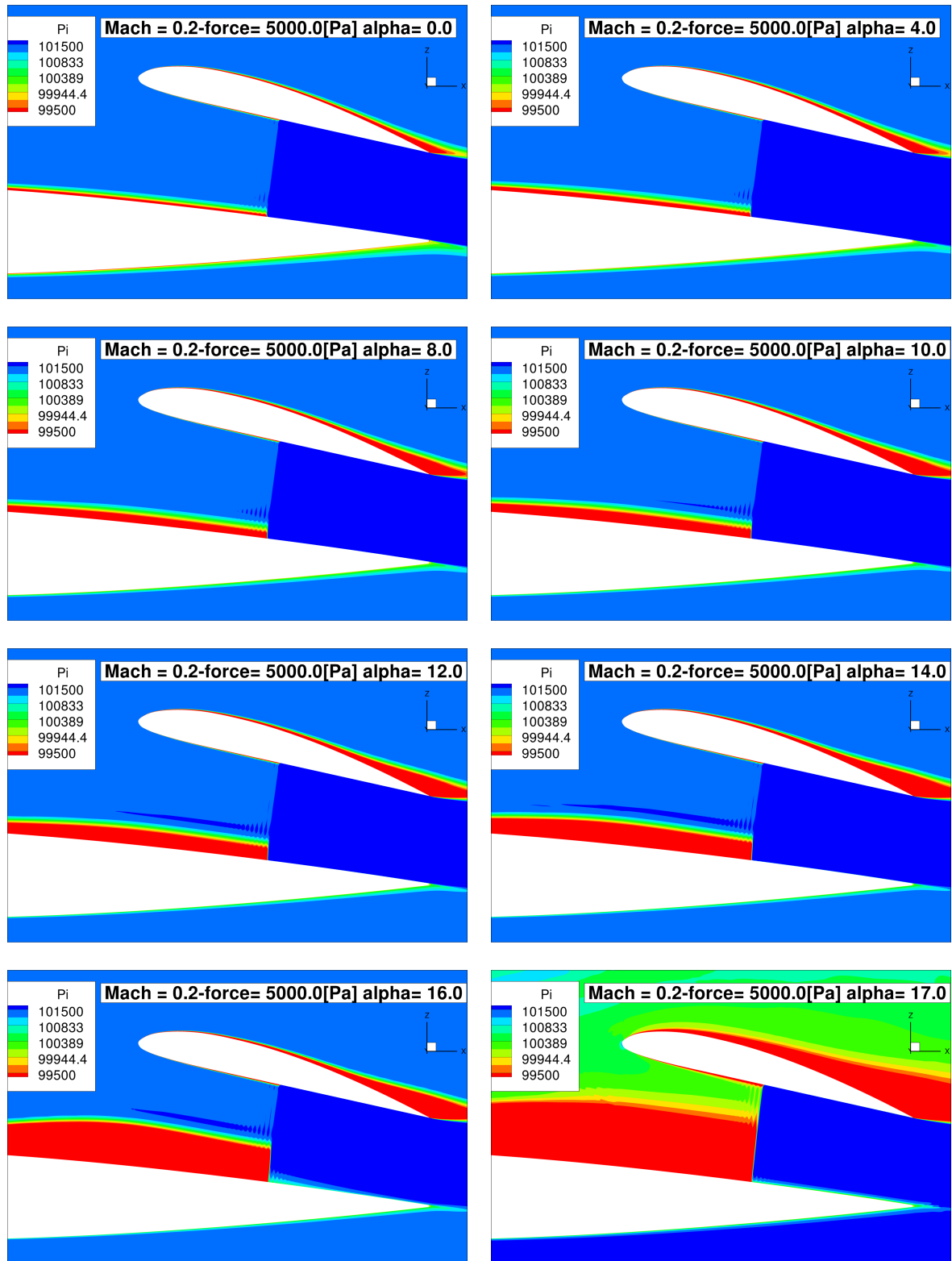
Figure 44: Details of the totale pressure around the model for a fixed input force and different angles of attack. Big engine
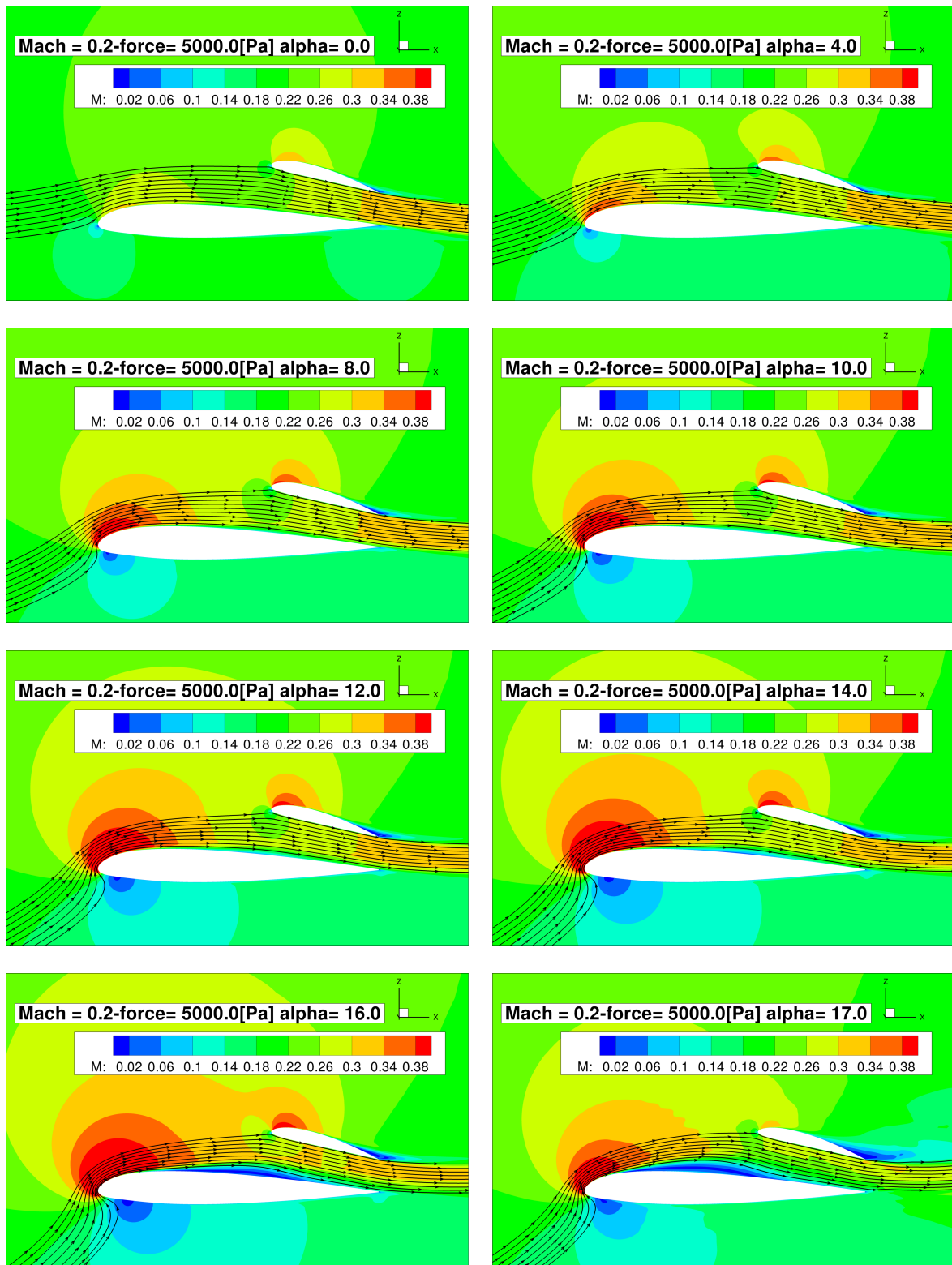
Figure 45: Details of the Mach number around the model for a fixed input force and different angles of attack. Big engine

4.4.2 Results of the cruise speed study

We have already noticed that this configuration is "extreme" even for very low Mach number.Also, we have studied also the configuration in cruise configuration, but convergence problems arose for several parametric configuration. Indeed, the circulation around the CLARK Y profile induced by the engine is responsible for the generation of a shock wave over the upper side of the nacelle, that should have required the modification of the mesh to better capture it (and as already said, the modification of the profile shape). In figure 46 the valuable results are shown. We can identify a "cruise point" for the force= $3000Pa$, $\alpha = 0°$. In this case the aspiration effect of the engine is sufficient to augment the lift coefficient of the desired amount without changing the angle of attack of the system. Again, the pitching moment coefficient is very negative, as for the take-off simulation. This configuration is inherently less stable than the two configuration that we studied so far.

(a) Lift coefficient

(b) Drag coefficient

(c) Pitching moment coefficient
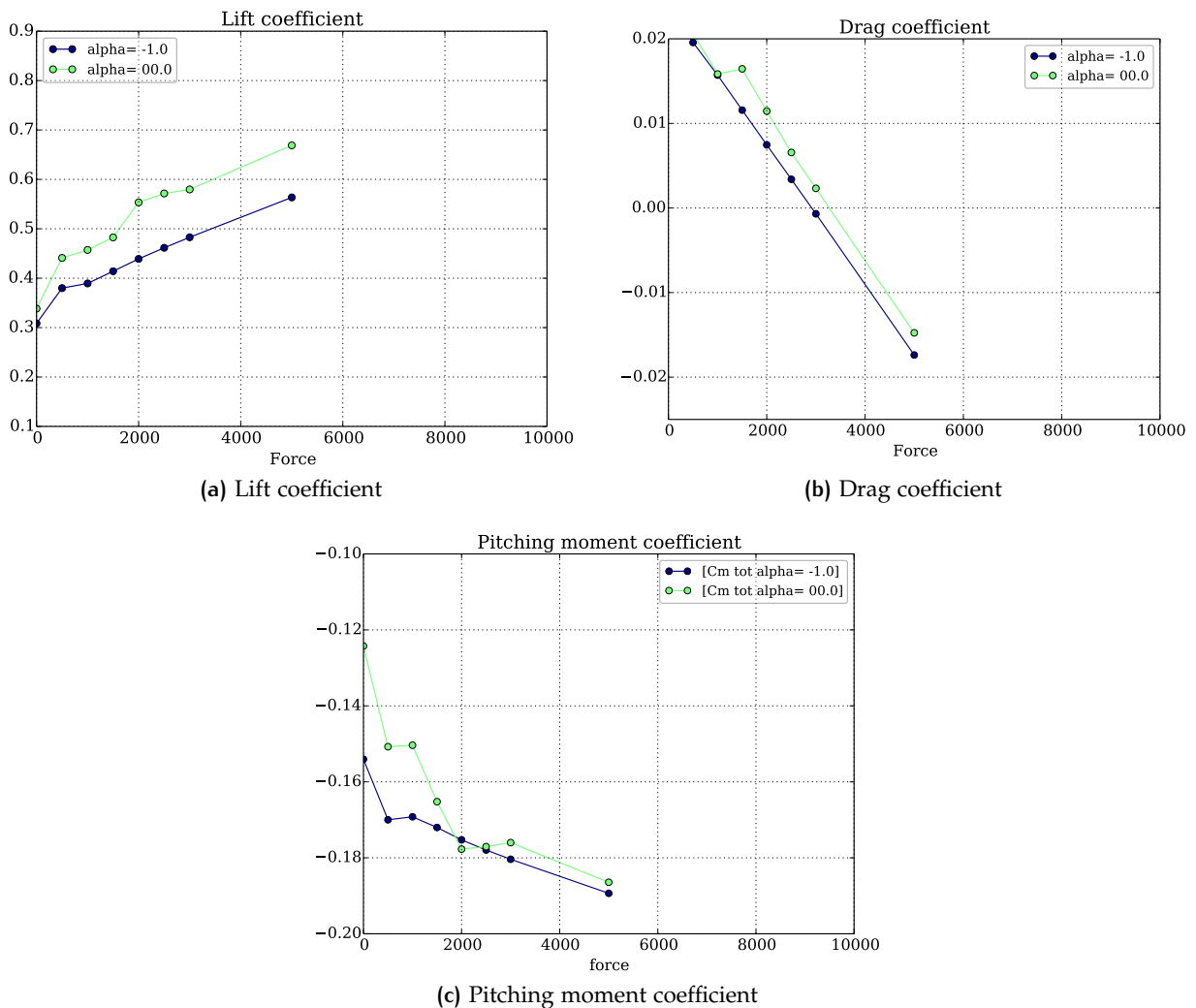
Figure 46: c_L,c_D e c_M vs input forces at cruise configuration (Mach number=0.5) for different angles of attack

4.4.3 Comparison

Let's compare this configuration with the original one: the difference between the two of them is that the engine (and the nacelle profile) has undergone a scaling up transformation with factor 3. Again, to do a significant comparison, in figure 47 are shown lift and pitching coefficient for a two cases such that $c_D \simeq 0$ (at least for low angles of attack, see figure 47c). It can be observed that the performances of the big engine are globally worse than the small one: whereas lift coefficient are a bit higher, stall happens much earlies (in term of angle of attack). In addition, pitching moment coefficient is much lower: this is due to the presence of the big CLARK Y profile that increases greatly the negative pitching momentum.

(a) Lift coefficient

(b) Pitching momentum coefficient
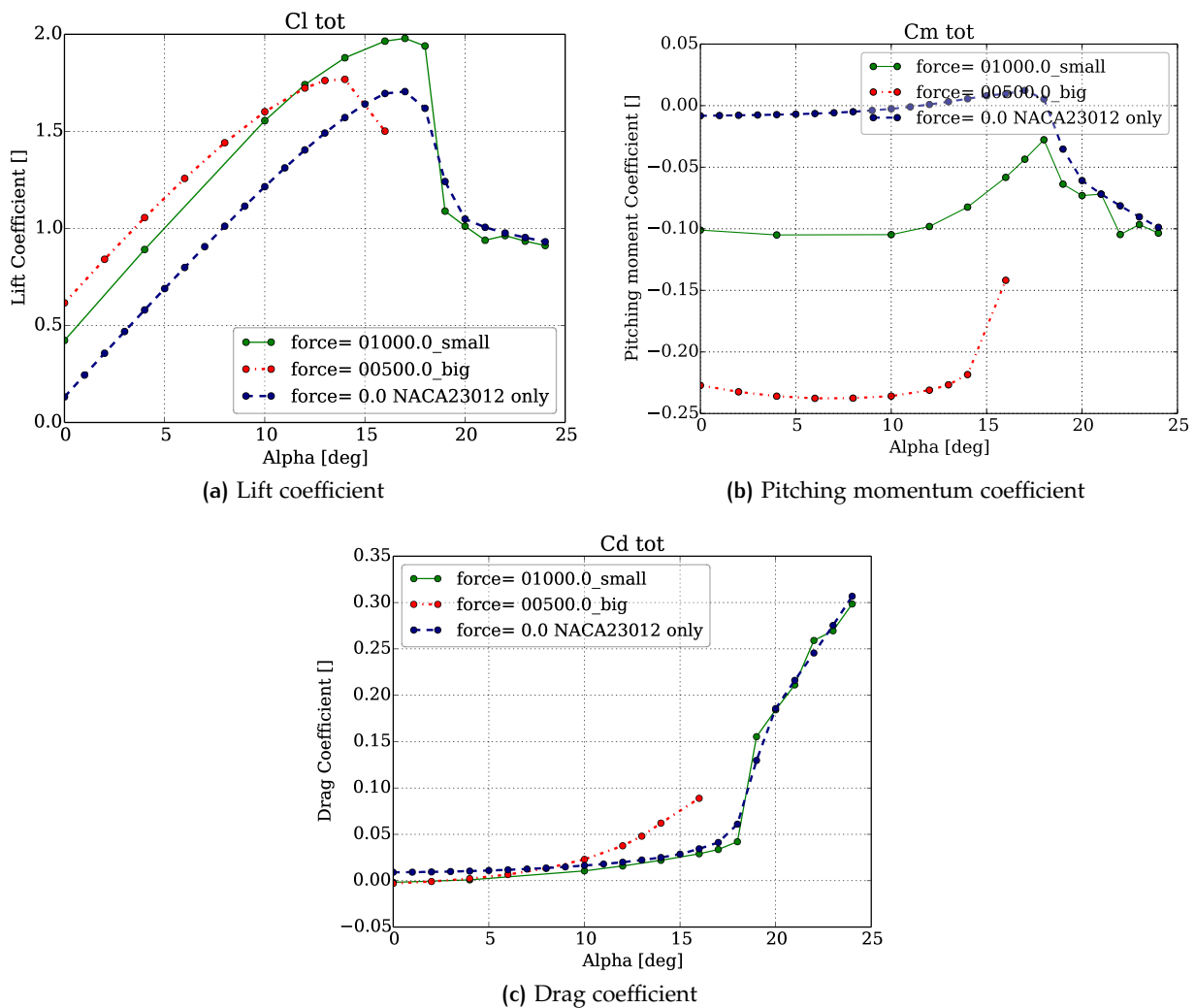
(c) Drag coefficient

Figure 47: Comparison of lift and pitching coefficients of the two configurations at $c_D = 0$ for the small and big engine

The comparison at Mach=0.5 substantially leads to the same conclusions: the drag is higher for the big engine, and pitching moment coefficient is more negative.
We also tried to measure the efficiency of the configuration, using the usual (rough) definition of efficiency. In this case, velocities in the actuator disk section are very

similar, but as it can be seen in figure 48 the performance is lower, even if we observe as usual higher performance for higher angles of attack. The reason of the higher performance of the small engine could be identified with the fact that the ratio between the surface ingesting the boundary layer and the total surface is higher in the small engine.
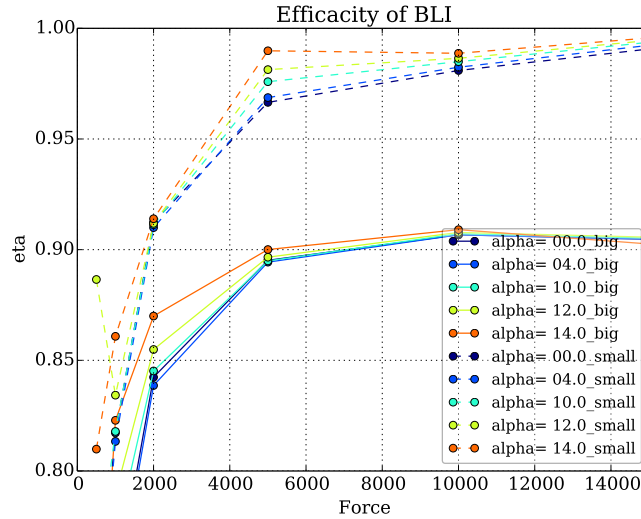
Figure 48: Comparison of the efficiency for the small and big engine

To conclude, in the previous sections we have recognised that an engine of this size is too powerful (for example, we can easily undestand the fact that it is able to reattach the flow over a stalled wing). This fact, along with the comparison that we have made, leads to the conclusion that this configuration is not a viable one, even if it (over)-respects the requirements that we have used to define the size of the engine in this system.

Mesh: engine behind the wing
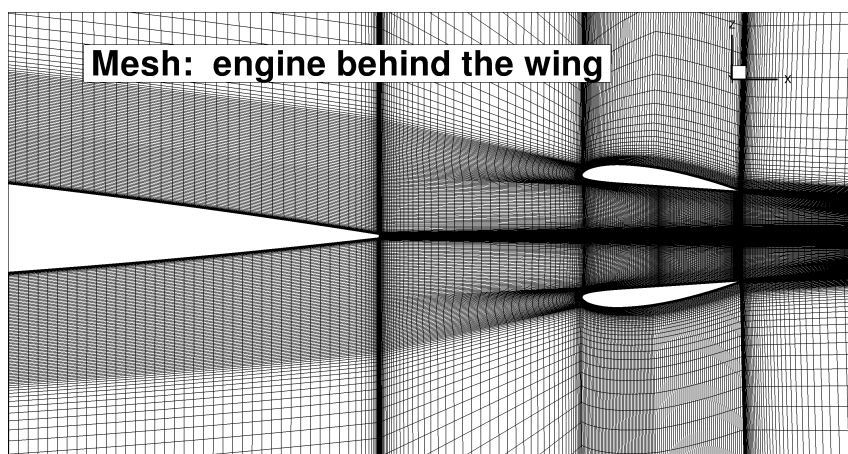
Figure 49: Detail of the mesh around the configuration with the engine behind the wing

4.5 AN ENGINE BEHIND THE WING

In this section we present the 2D model that we shown in section . This case is substantially different from all the others configurations. The engine is in a standalone configuration behind the wing, centred about the same axis. In this configuration the engine ingests the boundary layer that developed around the wing, and re-energizing the flow fills the wake behind the aircraft. This configuration is expected to be efficient because of this characteristic (see figure). It is very important to note that this configuration separates itself from the concepts that we have studied so far: the engine in this case is not integrated to the wing structure, and all advantages that came from such a integration are lost. At the same time, this case is an important reference to compare with all the other models.

The model is shown in figure and the mesh, that consists of around 300000 points, is shown in figure . The engine, in this case is symmetrical around the main axis, with the addition of a second CLARK Y profile in the lower part. We do put in evidence that the engine in this case has a surface that is the double of the original one. Moreover, the angle of attack of the two profiles delimiting the engine has been reduced, to keep the ratio actuator disk surface over the exit surface constant. The two parametric studies that have been carried out are shown in table and .

Table 11: Parametric study for the engine behind the wing,Navier Stokes calculation. Low speed study

Parameter	Value
Mach Number []	0.2
Force (per unit of surface) [Pa]	0 1000 2500 5000 10000 15000
Angle of attack [deg]	0° 2° 4° 6°8° 10° 12° 13° 14° 16° 17° 18°20°22°24°

Table 12: Parametric study for engine behind the wing, Navier Stokes calculation. Cruise study

| Parameter	Value
Mach Number []	0.5
Force (per unit of surface) [Pa]	0 1000 2000 3000 5000
Angle of attack [deg]	$-1°$ $0°$ $1°$

4.5.1 Results for the low speed study

In figure 50 on the next page lift, drag and momentum coefficients are shown. As expected, in this configuration, being the engine detached/separated from the wing, the lift coefficient is not deteriorated, but it is higher than the reference configuration, but at the same time the stalling behaviour is surprisingly different from the reference configuration.

The presence of the engine behind the wing, even if it is separated from it, influences the flow around the wing. Indeed, in figure 51 on page 63 we can observe that the stall in this configuration develops at the trailing edge (at $16 - 17°$) but, the wing stalls only at $18°$: the engine is able to postpone the stall, in exchange of a higher loss in lift coefficient through the transition. Post-stall images are shown in the two last figures (where we can notice also a stall on the lower of the CLARK Y!).

Observing figure 50d on the next page, it is interesting to note the substantial different behaviour of this configuration from the reference case: the positioning of the engine far away from the reference point for the calculation of the pitching moment coefficient is responsible for those very high (negative) values of the coefficient, along with the fact that the fluid flow for higher angle of attack does not circulate around the wing but comes mainly from the lower part (see figure 51).

In the figure 52 on page 64 we put on evidence the boundary layer that is ingested by the engine in this configuration. For very high angle of attack, it is evident that this configuration does not ingest all the boundary layer that develops around the wing. Because an aircraft works less at negative angles of attack, it could be envisagable to move the engine upwards.
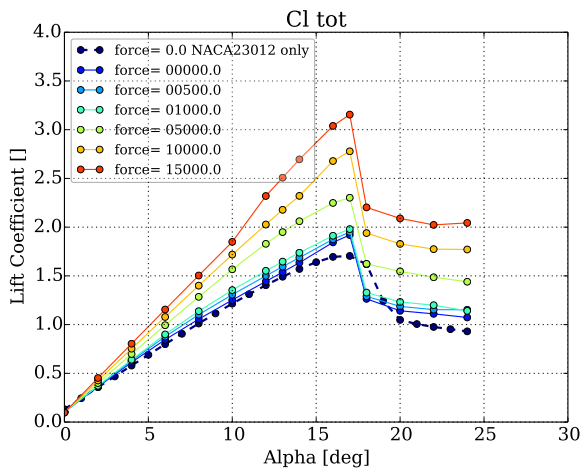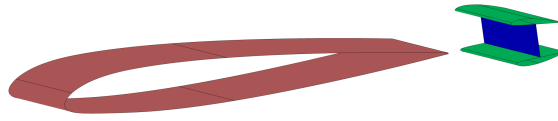
(a) Lift coefficient
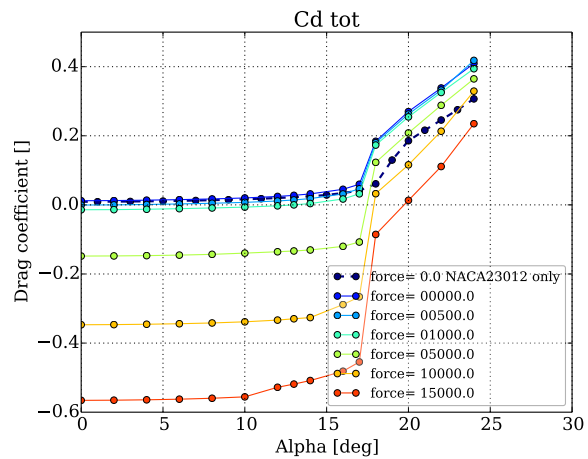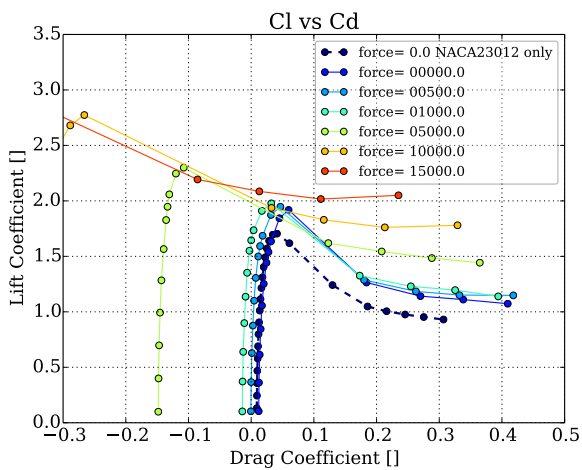
(b) Drag coefficient

(c) Lift coefficient versus drag coefficient, iso-forces
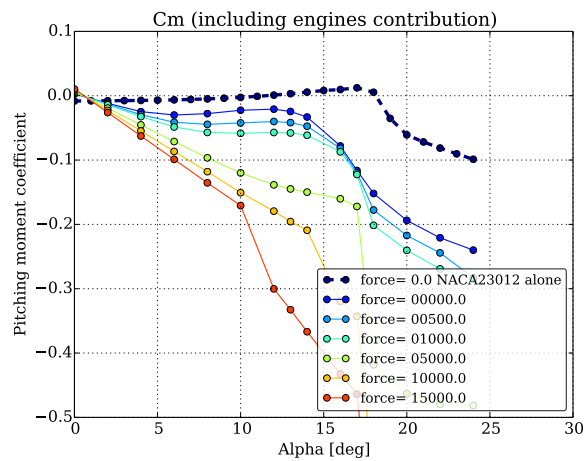
(d) Pitching moment coefficient

Figure 50: Parametric study of the lift and drag coefficients for different forces and angles of attack. Mach=0.2, Navier Stokes simulation. The dashed line represents the case where only the NACA23012 alone is simulated
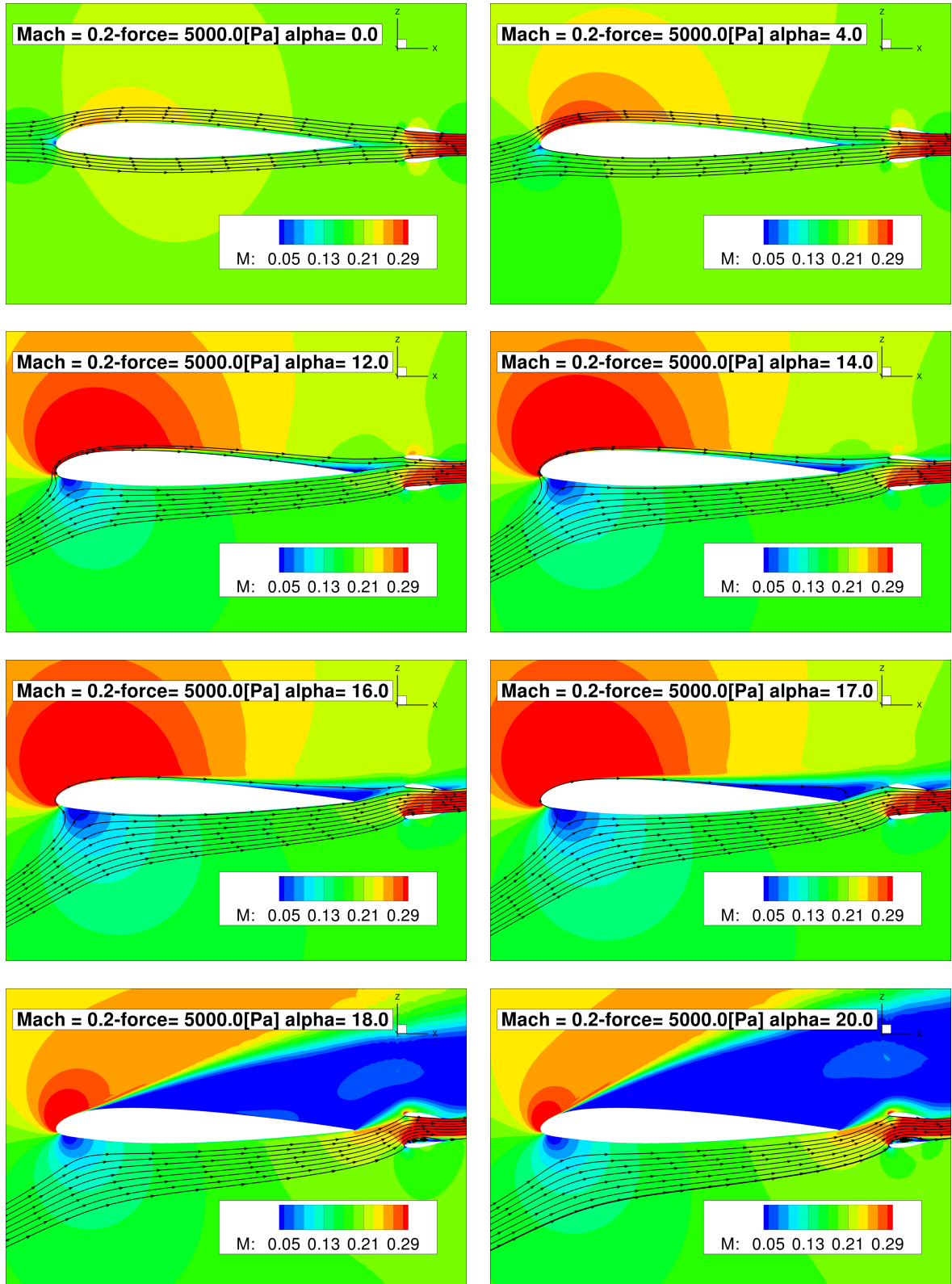
Figure 51: Details of the Mach number around the model for a fixed input force and different angles of attack.
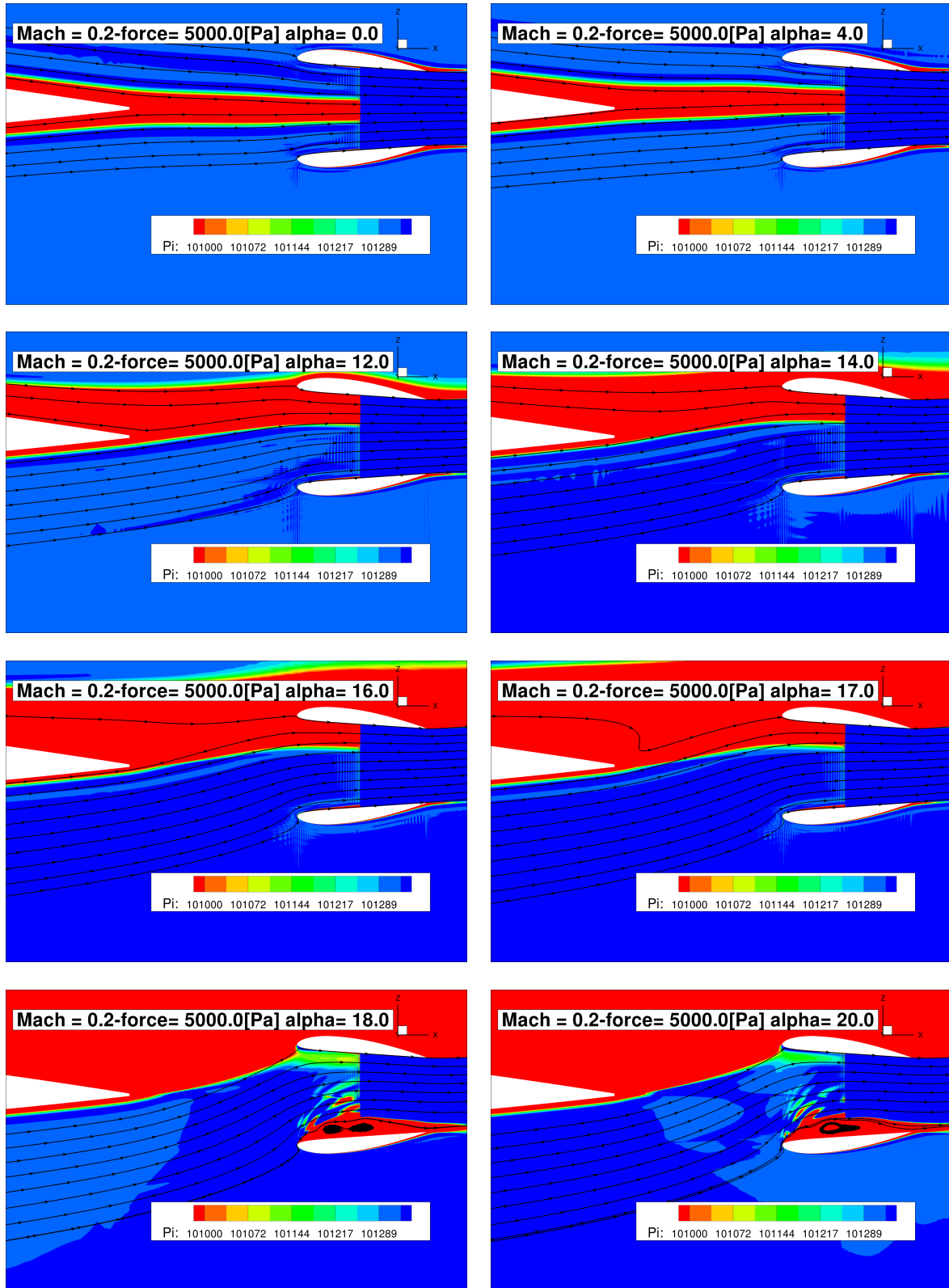
Figure 52: Details of the total pressure around the model for a fixed input force and different angle of attack.

4.5.2 Results of the cruise speed study

To conclude, as usual, we present an analysis of the configuration at Mach=0.5. Observing figure 53a we note that the lift coefficient is not very much influenced by the increase of the force: this sounds logical whether you consider at the separation of the engine from the wing. As usual, drag coefficient does not vary too much with angle of attack. The ideal cruise point could be identified at force=3000Pa, $\alpha = 3°$. Pitching moment coefficient again is almost zero and generally stable according to figure 53c.

(a) Lift coefficient

(b) Drag coefficient

(c) Pitching moment coefficient
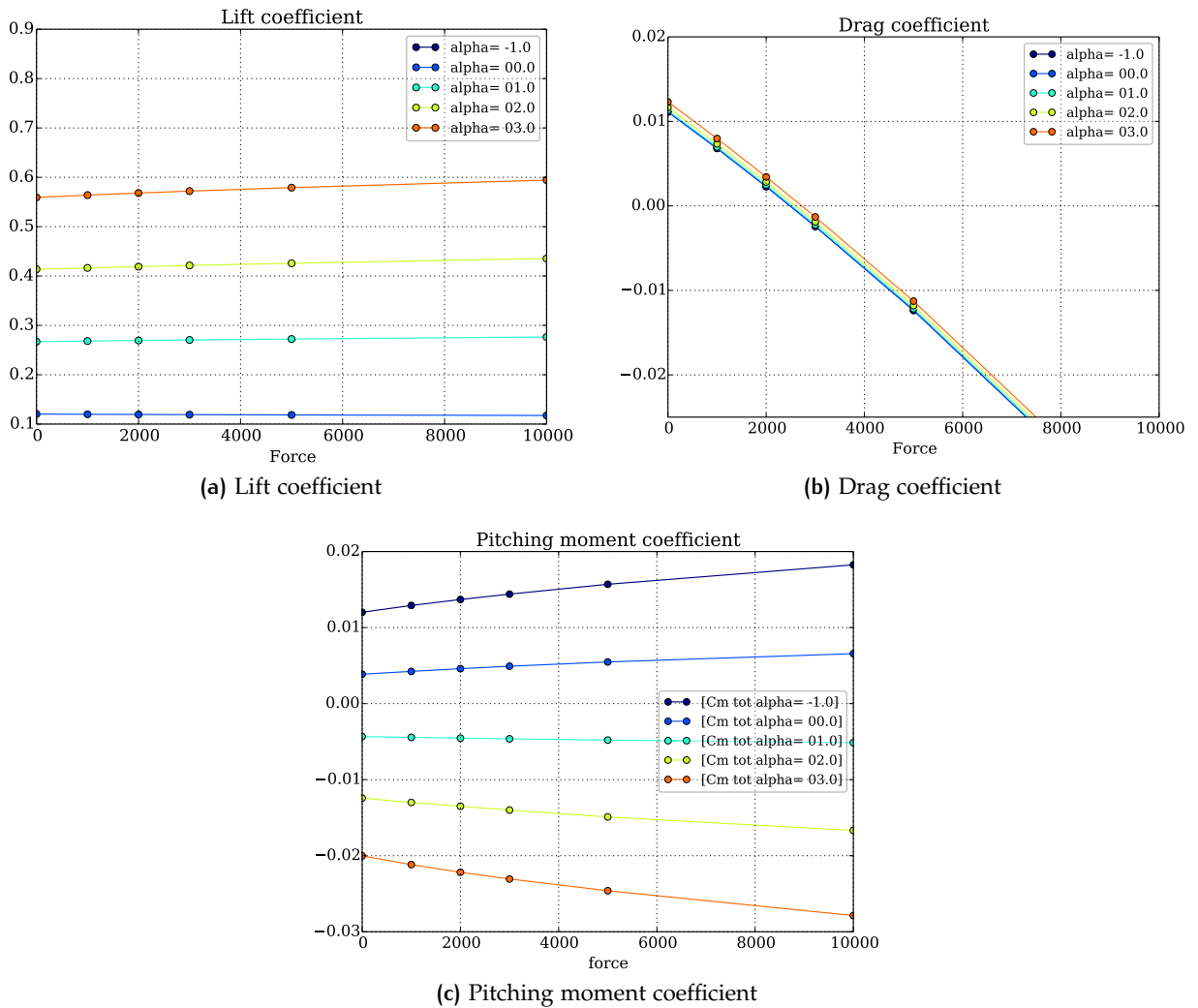
Figure 53: c_L, c_D e c_M vs input forces at cruise configuration (Mach number=0.5)

4.5.3 Comparison

In this section we will compare this configuration with the trailing edge small engine, as done for the other configurations. We remind that in this configuration the engine has been symmetrized and therefore the surface is the double of the

first configuration (8cm vs 4cm).

This configuration is very different from the other, and a comparison is more difficult. We notice that the lift coefficient of this configuration is lower at constant force. Indeed, the lift generated by the system with the engine located over the trailing edge is enhanced by the presence of the engine itself. The main contribution of the nacelle to the lift in this configuration is significant (around $c_L \simeq 0.5$) where in the other system is negligible and almost all the lift comes from the wing profile. It could be noticed, that for a constant force, the Δc_L of the wing between the two configurations is around $0.5 \simeq 1$, that clearly demonstrates the beneficial effect of the engine over the trailing edge.

If, anyway, we compare configurations such that $c_D \simeq= 0$, such as in figure the difference is less accentuated, but still present. The maximum lift coefficient is almost unchanged because in both cases we observe the same kind of stalling behaviour.

As already remarked, the pitching moment coefficient behaviour is quite different because of the "different" flow that the two configurations capture. The trailing edge device always captures the fluid flowing over the upper side of the system, where the engine behind the wing captures a flow that for increasing angles of attack flows below the wing, which explains the diminution of pitching moment coefficient in figure 54b.

In cruise configuration (i.e. at low angle of attack, Mach=0.5) lift coefficient is lower, for the same reason explained previously.

Finally, we made a comparison in terms of efficiency in figure . Again, performances of the trailing edge system are better. Attention should be paid to the fact that for this configuration it does not measure the global performances of the system, but of the engine only.

To conclude, the two configurations are substantially different and a comparison in terms of performance is not significant with our "basic" definition of efficiency. In terms of aerodynamics performances, again, the trailing edge system is better, because of higher lift produces for $c_D \simeq 0$, and because of lower pitching moment.
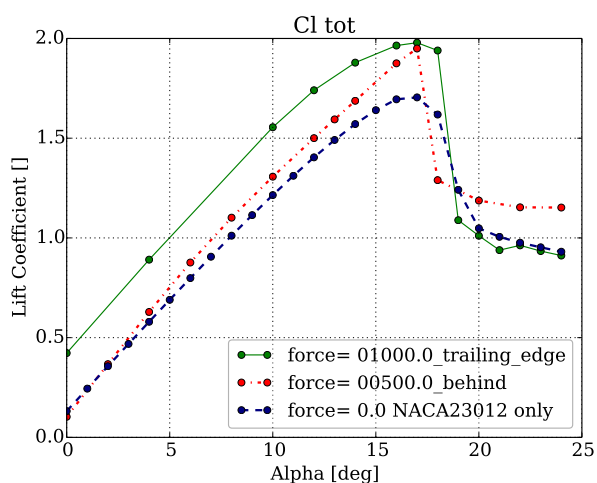
(a) Lift coefficient
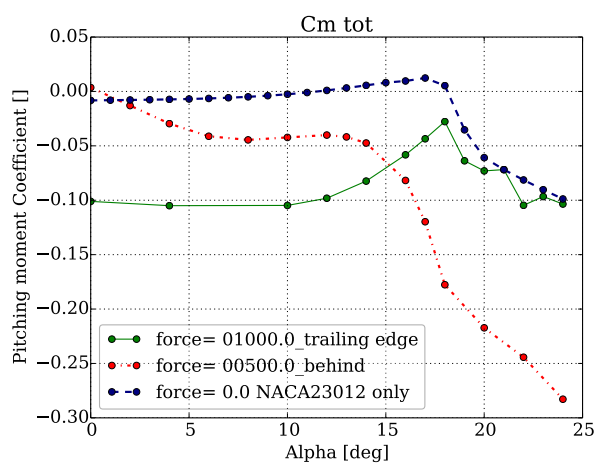
(b) Pitching momentum coefficient
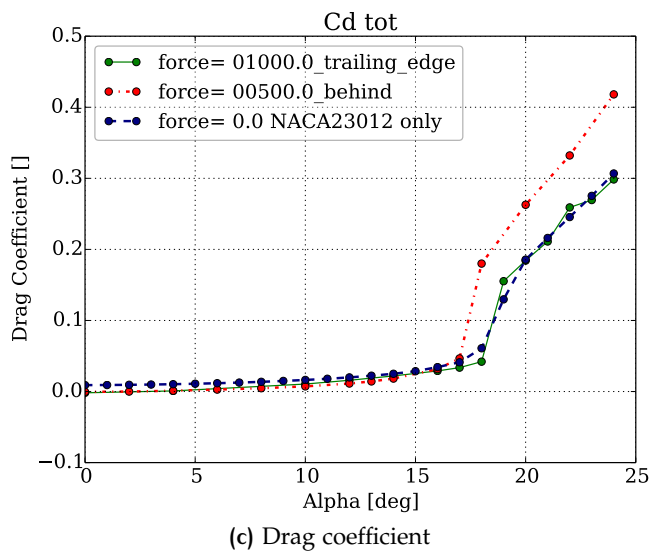
(c) Drag coefficient

Figure 52: Comparison of lift and pitching coefficients of the two configurations at $c_D = 0$ for the small and big engine
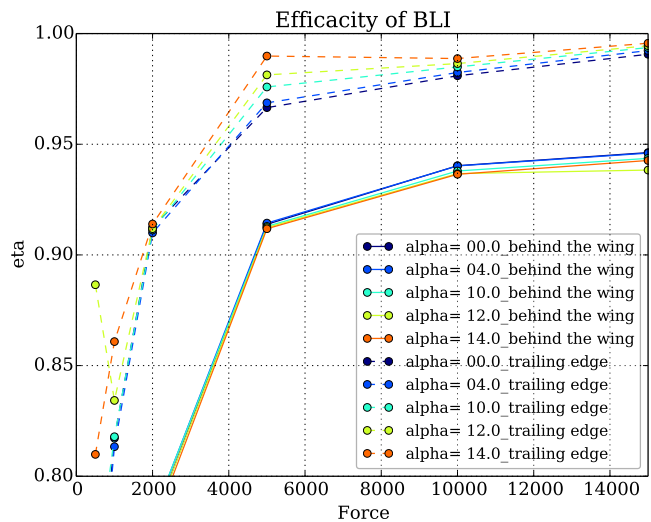
Figure 53: Comparison of the efficiency for the engine behind the wing and the trailing edge engine

4.6 CONCLUSION

In this chapter we have shown and analysed the results of different 2D models for distributed propulsion, focusing on the effects over lift, drag and pitching moment coefficients. We also tried to make some comparison, between the first configuration (small engine located behind the wing) and the other configurations. We could draw the following conclusions:

- The configuration with the model located at the leading edge has a definitive advantage over the reference one, both in take-off and cruise performances. Moreover, post-stall behaviour is much better in terms of fligh quality. Also, the positioning of the engine ahead of the aerodynamic center, gives a more stable configuration as a result. Nevertheless, it is necessary to remind that thermo-structural aspect of this configuration has not been taken into account in this analysis. Also, the shape of the conduct resulting from the positioning of the engine over the leading edge of the engine results in a substantially faster flow through the actuator disk, even if this point could be solved with an accurate design.

- The comparison between the two engines located at the same position, but with different sizes has lead to some mixed results. As expected the increase in the engine size results into higher lift coefficients, but the side-effects is that the significant size of the nacelle increases drag coefficient et lowers stall angles. At the same time, it is acknowledged that the big engine is over-sized compared to the size of the wing. The ideal configuration should have a smaller size than the big engine we have simulated.

- The last configuration is substantially different and an effective comparison is difficult. It results that for a given drag coefficient, the corresponding lift coefficient is higher for the reference model. From an aerodynamics point of view, there is little interest in considering this configuration as efficient as the trailing edge engine. Also, the complexity that such an engine would introduce from a mechanical and structural point of view decreases the interest in such a configuration.

We also tried to estimate propulsive performances through the definition and calculation of an efficiency that (roughly) represents the propulsive yield of the integrated engine. It results that the most effective configuration is the first one, with a small engine over the trailing edge. Indeed, the boundary layer that develops around the wing in this configuration is completely ingested maximizing the ratio between boundary layer surface and engine actuator disk surface. This is far from being a definitive and precise analysis, because of the limits in the estimation of the power, because of the integrated configuration, and because of limits generated by the boundary condition. An energy-based far-field approach would be necessary to accurately estimate gain of distributed propulsion because of boundary layer ingestion.

5 | A 3D MODEL FOR DISTRIBUTED PROPULSION

In this chapter we will present the final study of the internship: the CFD simulation of a concept of a futuristic aircraft equipped with distributed propulsors.

5.1 THE MODEL

The natural continuation of study of the two dimensional models that we have carried on so far is to study an aircraft concept equipped of distributed propulsion. The model that we have studied is shown in figure 54. This model has been built directly from the 2D-model:

- The aerodynamic profile of the aircraft body is drawn from a NACA23012 profile, and nacelle is still described by CLARK Y profile. To simplify the model, no tails or control surfaces are present (therefore the concept is inherently unstable).

- The propulsive system, as usual, is described through the introduction of an actuator disk boundary surface. This model could be very simplistic for 3D simulation, but at the same time it is a valid tool to quickly assess global aerodynamic performances of the aircraft.

- The wingspan of this aircraft is around 4 meters. The aircraft could be assimilable to a recognition/transport automatic drone.

- The height of the engine surface is set to 8 cm, a compromise between the two trailing edge configurations that we have studied in the previous chapter.
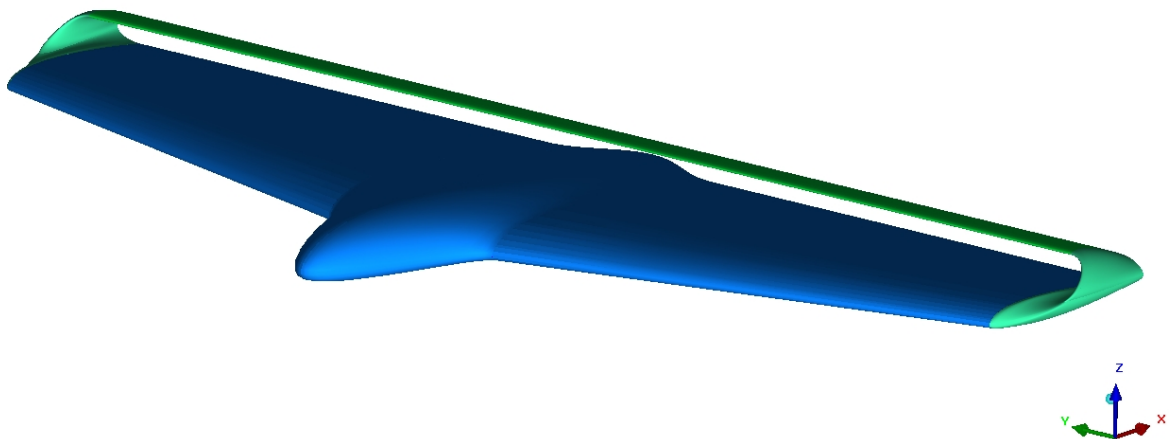

Figure 54: 3D conceptual configuration for distributed propulsion

The objective of the study of this 3D model are:

- to evaluate aerodynamics effects in a 3D configuration;

- to study the use of the actuator boundary condition in 3D-configuration for multi-block/Chimera meshes

- to compare the results with the the 2D model.

5.2 THE MESH

As to the mesh for this simulation we used some advanced techniques for meshing, such as "Chimera" and non-coincident matching. The Chimera method which enables a discretization of the flow equations in meshes is composed of overset grids, a technique that facilitates meshing of complex configurations composed of the meshing of a basic geometry and of additional elements. Communication between component grids is achieved by interpolation within overlapping grid regions (overset grids).

The grids around the surfaces of the aircraft have been done through the software Pointwise. This mesh is itself a multi-block structured mesh with overlapping blocks, as shown in figure 55a. Around this grid, a Cartesian multi-block octree has been built (figure 55b), where some advancing matching techniques have been used, such as non-coincident matchings: there is no matching between the grids of two facing blocks, but there is a 1 to 2 matching mapping. This technique simplifies mesh generation for complex configurations, and reduce the global number of mesh points for a given configuration, by preventing the propagation of mesh refinements throughout the computational domain. At last, the exterior domain has been meshed through the use of Cartesian grid abilities of elsA.

The mesh consists of around $20 \cdot 10^6$ elements, but due to overlapping regions the actual number of calculation points is lower.
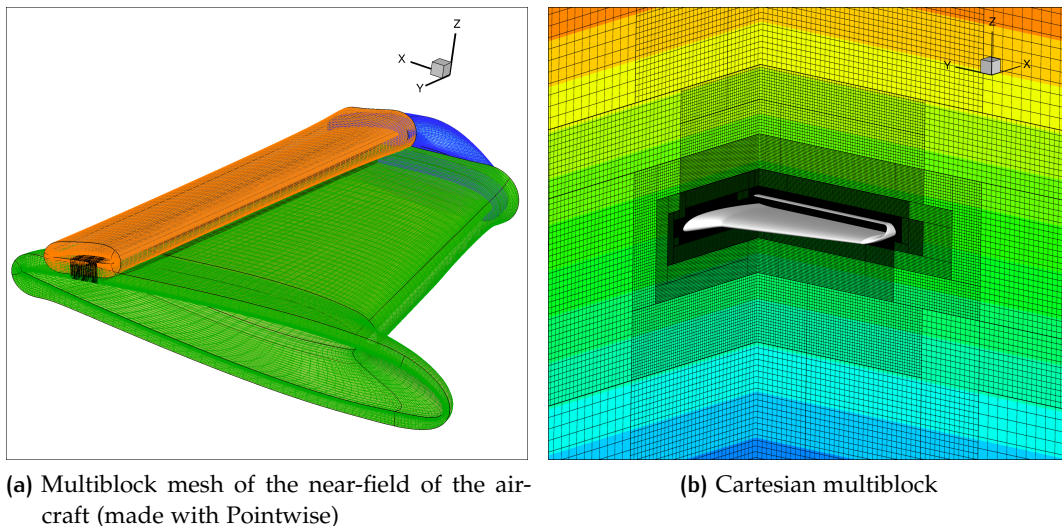

(a) Multiblock mesh of the near-field of the aircraft (made with Pointwise)

(b) Cartesian multiblock

Figure 55: Mesh of the 3D model: details of nearfield mesh and farfield cartesian grid

5.3 CFD SIMULATIONS AND RESULTS

For this configuration we have studied the cases that are indicated in table 13. An attempt to study cruise performance at Mach=0.5 has been done, but calculations does not converge. As already identified for 2D model, the chosen profiles for the aircraft are not adapted for higher speeds. In addition, the geometry of the connection between the wing and the nacelle (tip) should be refined (there are some sharp edges).

Table 13: Parametric study, 3D model

Parameter	Value
Mach Number []	0.2
Force (per unit of surface) [Pa]	0 3000 5000
Angle of attack [deg]	0° 4° 8° 12° 16°

A typical solution convergence is shown in figure 56. The L2-norm of the residual is plotted, and it can be seen that the residuals converge approximately 3 to 4 orders of magnitude. The lift is also shown to converge to a steady value. In figure 57 on the following page pressure contours (c_p) on the surface are shown, along with Mach contours on the symmetry plane: the acceleration of the flow caused by the engine is evident. Discontinuities of the visualization are due to the discontinuity of the solution, caused by the non-coincident matchings.

(a) Residual of ρ and ρu.

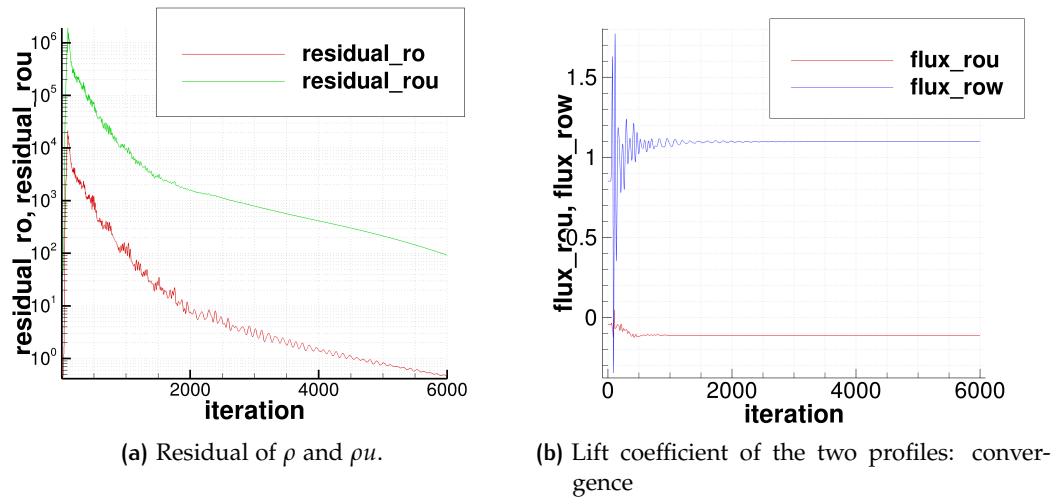(b) Lift coefficient of the two profiles: convergence

Figure 56: Convergence curve 3D model. Mach=0.2, force=5000, $\alpha = 12°$

An analysis of the results has highlighted some defects of the mesh:

- the lack of a sufficiently refined grid behind the profile to capture the wake dissipation flow

- the growth-rate of the Cartesian grid is possibly too fast

- the mesh around the tip should be reworked

But, even considering those problems, the quality of the solutions is sufficient to assess an evaluation of this preliminary concept. For further analysis, a refinement of the mesh is suggested.
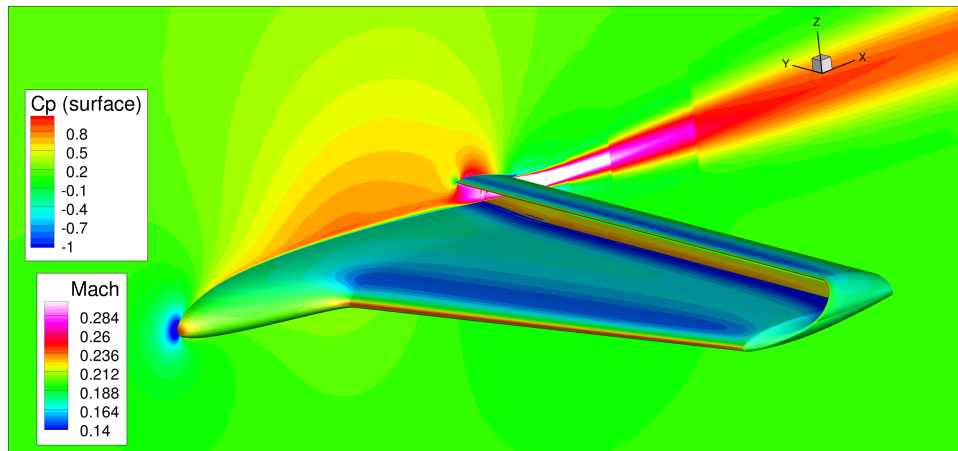
Figure 57: Contours of C_p on the body surfaces and Mach number in the symmetry plane

In figure 58 we can observe the streamlines around the aircraft, in a high angle of attack configuration ($\alpha = 12°$). The flow is quite regular around the surfaces, except for the tip of the wing where a vortex is generated. In figure 59 on the facing page we can remark an iso-surface corresponding to the total pressure gain given by the engine to the flow (in this case for a $\alpha = 0°$). Again, we can observe the swirling flow around the wing tip.
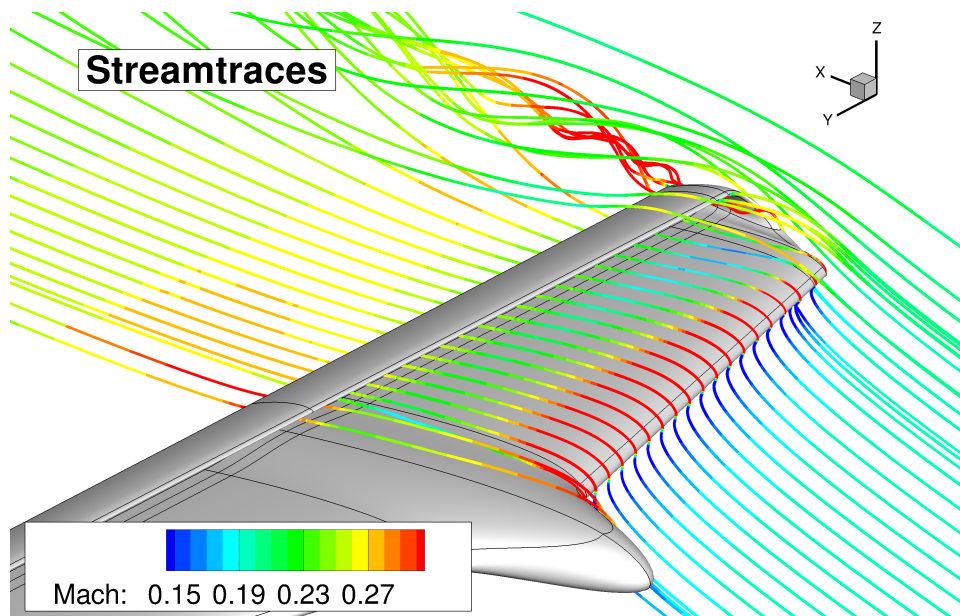
Figure 58: Flow stream lines around body surfaces, coloured corresponding to Mach Number. Mach = 0.2, $\alpha = 12°$, force=5000 Pa, $P_\infty = 101325 Pa$

Finally, in figure 60 on the next page lift and pitching moment coefficients are shown. Drag coefficient is not shown (because of the defects of the mesh).
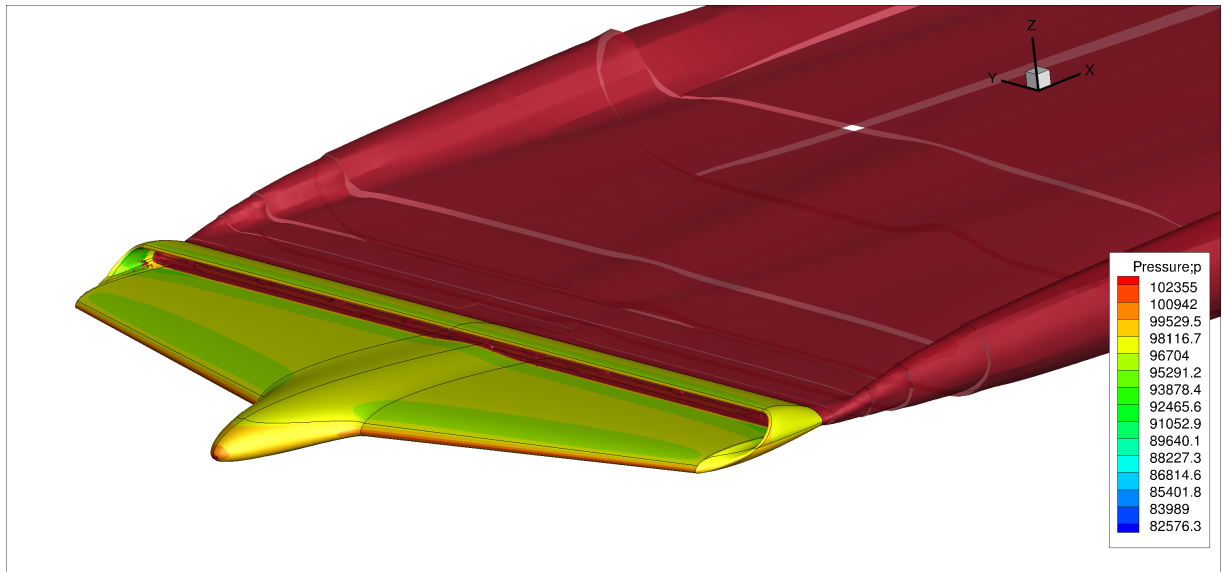
Figure 59: Iso-surface of the gain of total pressure coefficient in the fluid flow, along with pressure values over the surface of the aircraft, Mach=0.2,$\alpha = 0°$,force=5000 Pa,$P_\infty = 101325 Pa$

(a) Lift coefficient

(b) Pitching moment coefficient
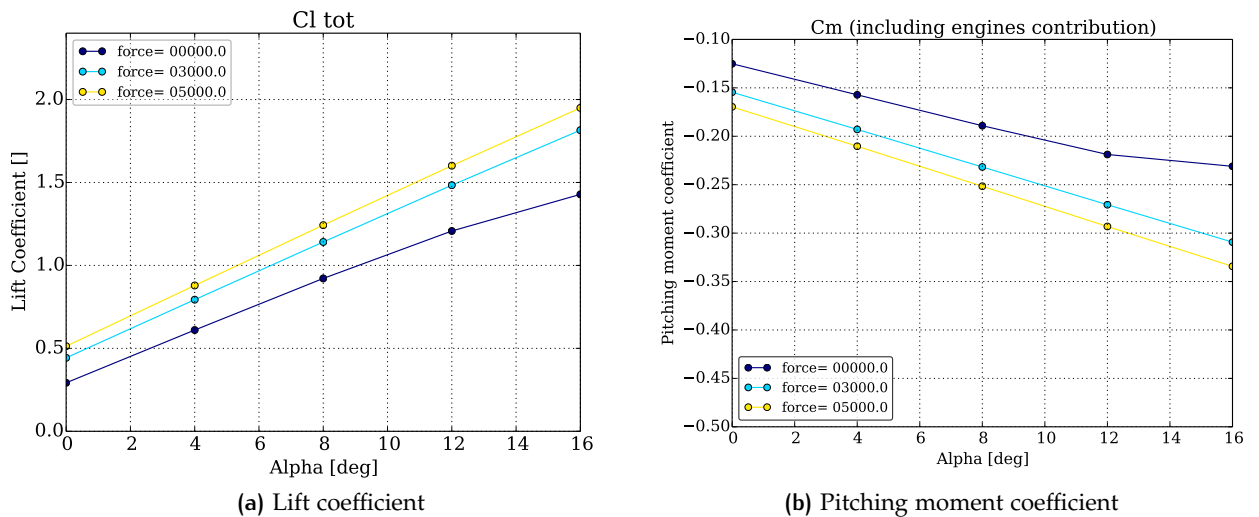
Figure 60: Parametric study of the lift and moment coefficients for different forces and angle of attack. Mach=0.2. Reference surface for calculation of c_L, $S_{ref} = 1.44m^2$

5.3.1 Comparison with 2D model

In this section we will compare the result of the the 2D-model, configuration described in section 3.3 on page 21, with this 3D model. In figure 61a a comparison of is shown, where for the 3D-model the section has been chosen where the chord c=1. Qualitatively there is good agreement between the two solutions, except for some details that are given by the masking and interpolation of multi-block mesh around the engine.

In figure 61b a comparison of the pressure coefficient around the wing profile between the two configurations is shown. The integration of those curves gives the local lift coefficients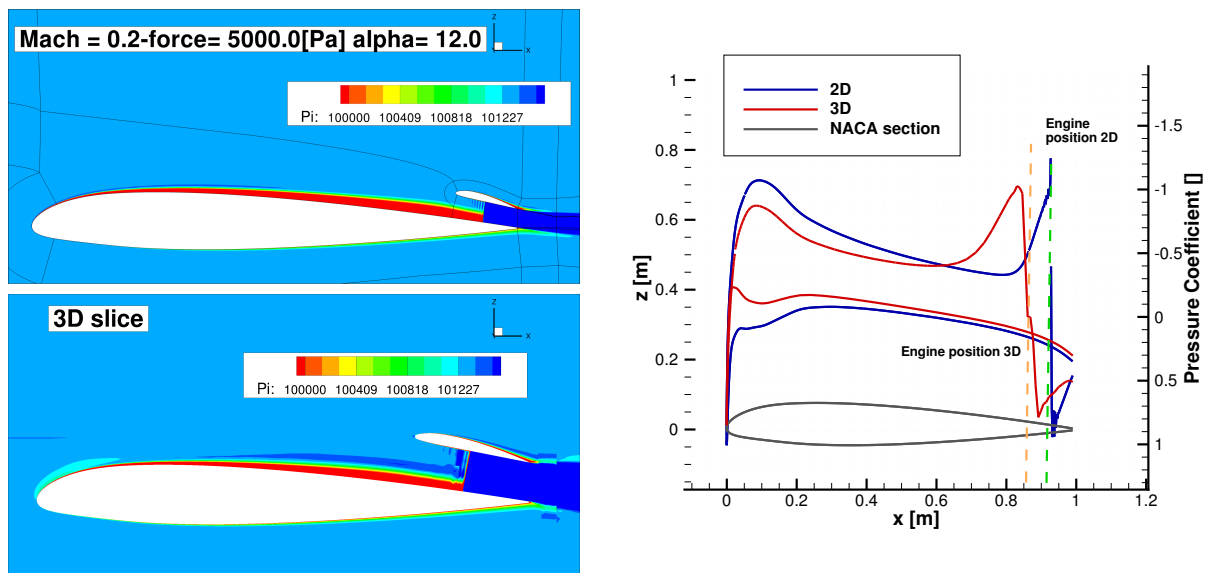, that are close: $c_{L_{3D}} = 0.42$ vs $c_{L_{2D}} = 0.56$, that is realistic because of the induced up-wash in the 3D model. Those figure proves that a very simple 2D model could reproduce very well the aerodynamics of the complete aircraft. In figure 62 on the next page total lift coefficient has been superimposed.

(a) Comparison of the total pressure between the 2D model and the 3D model, Mach=0.2,α = 12°,force=5000 Pa, $P_\infty = 101325Pa$

(b) Comparison of c_p between the 2D and 3D simulation for the wing profile. Simulation M=0.2, force=5000, $\alpha = 0°$, $P_\infty = 101325Pa$

Figure 61: Comparison between 2D and 3D CFD simulation. The section for 3D chosen where the chord $c = 1$.

Again, we observe that the behaviour is very similar between both configurations. The aircraft does not stall in the given simulation (i.e. up to 16°) and the behaviour is linear. The difference is only in slope, given by the 3D effect of up-wash (induced velocities) and by the effect of the different size of the engine that triples the contribution to the lift coefficient. To conclude, in figure 63 on the facing page local lift coefficient and sectional loads are shown for the wing and the nacelle. It is very important to notice that the local lift coefficient over the wing is constant, meaning, again, that a 2D dimensional simulation of a section of an aircraft is valid. On the other side, oscillation of local lift coefficient are observed: those are due to

the local interpolation on the lower part of the nacelle profile due to the Chimera multi-block simulation.
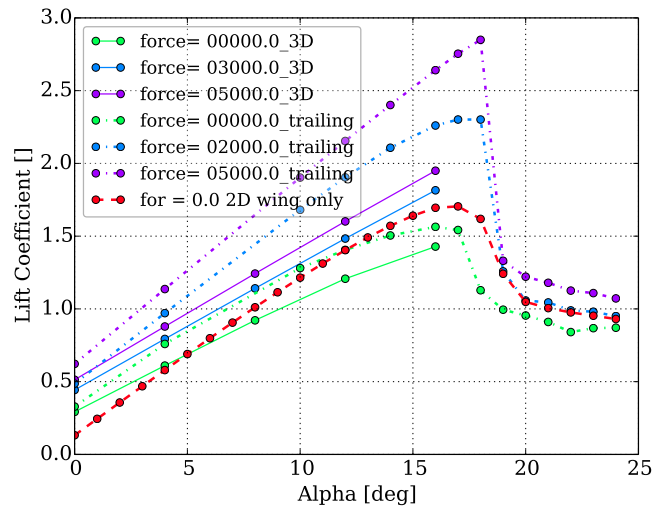
Figure 62: Comparison of c_L between the 2D and 3D simulation for the wing profile. Simulation M=0.2. Reference surface for calculation of c_L, $S_{ref} = 1.44m^2$, $P_\infty = 101325Pa$

(a) Local lift coefficient and loads over the body of the aircraft

(b) Local lift coefficient and loads over the nacelle profile
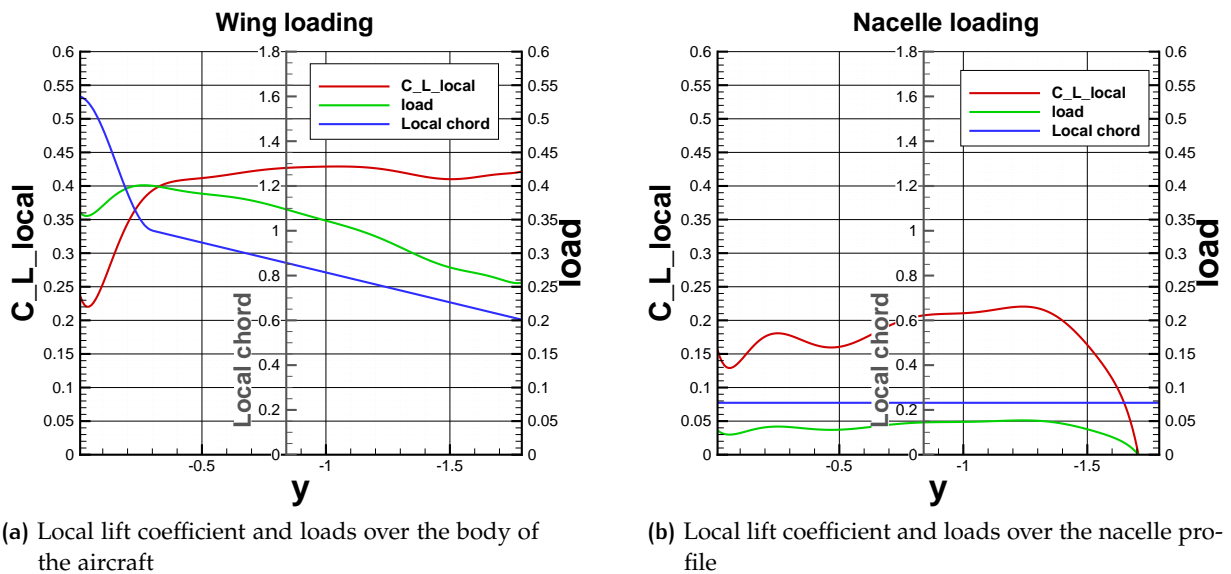
Figure 63: Local lift coefficient and local loads over the sections of the body of the aircraft and the engine profiles, Mach=0.2,$\alpha = 0°$,force=5000 Pa. (Data has smoothed through a polynomial fit)

5.4 CONCLUSION

In this chapter we have analysed a three-dimensional model of an aircraft equipped of a distributed propulsion system. The analysis has led to some significant conclusions:

- Boundary condition works well even for overlapping blocks (with careful attention to masking and interpolation priority);

- 2D sectional model describes adequately the sectional fluid flow of the 3D model, with similar results in terms of lift coefficient.

- The 3D analysis has some limits, that could be overcome by refining the mesh.

In this study, we have done a preliminary analysis of distribute propulsion starting from a simple 1D model up to a 3D more realistic one. We have analyzed in depth the boundary condition "actuator helico" finding some limits inherent to its formulation in elsA code. Even if those limits where not critical for the study, in the future, if we continue with this approach to the model of engines, we will consider to study a new formulation to get rid of non-physical oscillations that are present in this formulation.

The studies of 2D model have enabled us to identify the key aspects of the different models, and to identify the better ones. Further studies could advance on this axis, optimizing the shape of the engine duct to increase performances and better reproduce physical reality, with the confidence that those 2D-model are close to the complete 3D model. Indeed, the use of 2D model has let us simulate a very high number of different configurations in various flight conditions, which will still be an important aspect in those kinds of preliminary studies.

The problem of power estimation in such integrated configurations is of great interest, and it will be necessary to use a different and more precise approach to evaluate propulsive efficiency and performances.

The same applies to 3D models, whereas other boundary conditions could be used to represent the engine interface.

A | SIZING OF THE CONDUCT FOR CFD SIMULATION

Following the notations given in 3 on page 7, and given the following hypothesis we want to determine the dimension of a convergent nozzle that fulfils the given assumptions. Hypothesis:

- $P_0 = 101325\ Pa = P_9$ (adapted nozzle)

- $T_0 = 300K$

- $M_0 = 0.5$

- $M_2 = 0.6$

- $FPR = 1.1$

- $c_D = 0.0250$

- $\eta_f = 1$

Let's define two functions:

$$p(M) = (1 + \frac{\gamma - 1}{2} \cdot M^2)$$
$$q(M) = (1 + \frac{\gamma - 1}{2} \cdot M^2)^{\frac{\gamma}{\gamma - 1}}$$

A fixed point method has been used, that initially assumes a value for the surface of the section 9, and iterates over it. It can be shown that the subsequent values are independent of the initial guess A_0, therefore only one iteration is necessary. For the section 0, we can already calculate:

$$T_{i_0} = p(M_0) * T_0$$
$$P_{i_0} = q(M_0) * P_0$$
$$\rho_0 = \frac{P_0}{r \cdot T_0}$$
$$c_0 = \sqrt{\gamma \cdot T_0 \cdot r}$$
$$v_0 = M_0 * c_0$$

From the definition of the Fan Pressure Ratio we get:

$$\Delta P_i = (FPR - 1) \cdot P_{i_0}$$

Then the exit section (section 9 in the reference figure), remembering that $P_9 = P_0$, and using equations 13 and 10:

$$M_9 = \sqrt{\frac{2}{\gamma - 1} q(M_0) FPR^{\frac{\gamma-1}{\gamma}} - 1}$$

$$T_9 = T0 \cdot FPR^{\frac{\gamma-1}{\gamma \eta_f}} \cdot \frac{p(M_0)}{p(M_9)}$$

$$P_{i_9} = P_9 * q(M_9)$$

$$\rho_9 = \frac{P_9}{r \cdot T_9}$$

$$c9 = \sqrt{\gamma \cdot T_9 \cdot r}$$

$$v_9 = M_9 * c_9$$

From the continuity equation, expressing the density as a function of pressure and temperature we get a relations between the surface in 9 and in 0:

$$A_0 = \frac{M_9}{M_0} \cdot \sqrt{\frac{T_0}{T_9}} \cdot A_9$$

Similarly for the section 2:

$$T_2 = T_0 \cdot \frac{p(M_0)}{p(M_2)}$$

$$T_{i_2} = p(M_2) * T_2$$

$$P_2 = P_0 \cdot q(M_0) / q(M_2)$$

$$P_{i_2} = P_2 \cdot q(M_2)$$

$$A_2 = \frac{P_0}{P_2} \frac{M_0}{M_2} \cdot \sqrt{\frac{T_2}{T_0}} \cdot A_0$$

$$\rho_2 = \frac{P_2}{r \cdot T_2}$$

$$c_2 = \sqrt{\gamma \cdot T_2 \cdot r}$$

$$v_2 = M_2 \cdot c_2$$

To find the Mach number just after the fan (section 13) the conservation of mass flow is imposed between section 2 and section 13. Expressing the quantities as function of the pressure, Mach in section 2, total pressure $P_{i_13} = P_{i_2} + \Delta P_i$ and M_{13} we obtain:

$$\frac{P_{i_13}}{q(M_1 3)} - P_2 \cdot \frac{M_2}{M_{13}} \cdot \sqrt{\frac{p(M_2)}{p(M_{13})}} \cdot FPR^{\frac{\gamma-1}{\gamma \eta_f}} = 0$$

This equation can be solved numerically to obtain the only unknown M_{13}. Again, the rest of the calculation is trivial:

$$P_{13} = \frac{P_{i_13}}{q(M_{13})}$$

$$T_{i_13} = T_{i_2} \cdot FPR^{\frac{\gamma-1}{\gamma \eta_f}}$$

$$T_{13} = \frac{T_{i_13}}{p(M_{13})}$$

The total thrust of this model corresponds to the result of a momentum balance on the entire conduct that for our model yields:

$$F_{tot} = \rho_9 * A_9 * v_9^2 - \rho_0 * v_0^2 * A_0 \tag{49}$$

The thrust generated by the fan is the result of a momentum balance between 2 and 13:

$$F_{fan} = A_{13} * \left(P_{13} + \rho_{13} * v_{13}^2\right) - A_2 * \left(P_2 + \rho_2 * v_2^2\right) \tag{50}$$

and they are in general not equal (for example, for a incompressible flow, it can be shown that $F_{tot} = 2F_{fan}$). It can be assumed that $\frac{c_{Dtot}}{c_{Dfan}} = \frac{F_{tot}}{F_{fan}}$, that let us estimate the drag coefficient (or, equivalently) the thrust required to the fan. With the ratio $\frac{c_{Dtot}}{c_{Dfan}}$ so estimated we can use equation to obtain a new estimation for the initially supposed surface of exit section:

$$\frac{A_9}{A_0} = c_{Dfan} \cdot \left(\frac{M_0}{M_9}\right)^2 \cdot \frac{\beta}{\beta - 1} \tag{45}$$

Iterating over A_9 complete the sizing process of the conduct.

B | SIZING OF THE BIG ENGINE

In section 3.3 on page 21 we have done a parametric study of a configuration that had been designed to fulfil some basics gas dynamics specification (see appendix A) and to satisfy the limits that we have found in the preliminary design analysis in section 2.1 on page 7. What has been neglected so far, is the performance of the entire aircraft and the interaction with the distributed propulsion system. In the next section we will propose a simplified system to analyze the configuration that we have studied so far and to understand if it could be fitted over a real aircraft. Let's fix as objective a short-haul regional airliner, like the ATR 42-320. We therefore assume:

- Maximum take-off weight : $m = 16500 kg$

- Cruise altitude: $h = 6000m$

- Cruise Mach number: $M = 0.6$

- Aspect ratio: 12

- Lift to drag ratio : $\frac{c_D}{c_L} = 20$

- $c_{L,\text{cruise}} = 0.5$

- Take-Off Field Length $TOFL = 1000m$

- $c_{L,\text{stall}} = 2.5$ (first guess)

These values are average values for regional airliners and have been assumed to simplify the model. Following the figure 64 on the next page and under those hypotheses we calculate S_{ref}, i.e., the planform area through:

$$c_{L,\text{cruise}} = \frac{m \cdot g}{\frac{\gamma}{2} P(h) M^2 S_{ref}} \tag{51}$$

Assuming the lift to drag ratio, the calculation of the c_d is trivial, from which we can estimate the ΔP necessary in cruise configuration to flight:

$$c_D = \frac{D}{\frac{\gamma}{2} S_{ref} M^2 P(h)} = \frac{\Delta P \cdot A_{AD}}{\frac{\gamma}{2} S_{ref} M^2 P(h)} \rightarrow \Delta P \simeq 3300 Pa \tag{52}$$

where A is given by the span times the section $b \cdot d$, and b is calculated from aspect ratio= $\frac{b^2}{S_{ref}}$ (in this case $b = 20m$. This value should be compared against CFD values to arrange engine size.

On the other side, we could easily estimate M_{stall} because the maximum lift coefficient have been supposed giving $M_{stall} = 0.168$. From that, we could easily get landing Mach number (from $v_{landing} = 1.3 v_{stall}$) and take-off Mach number
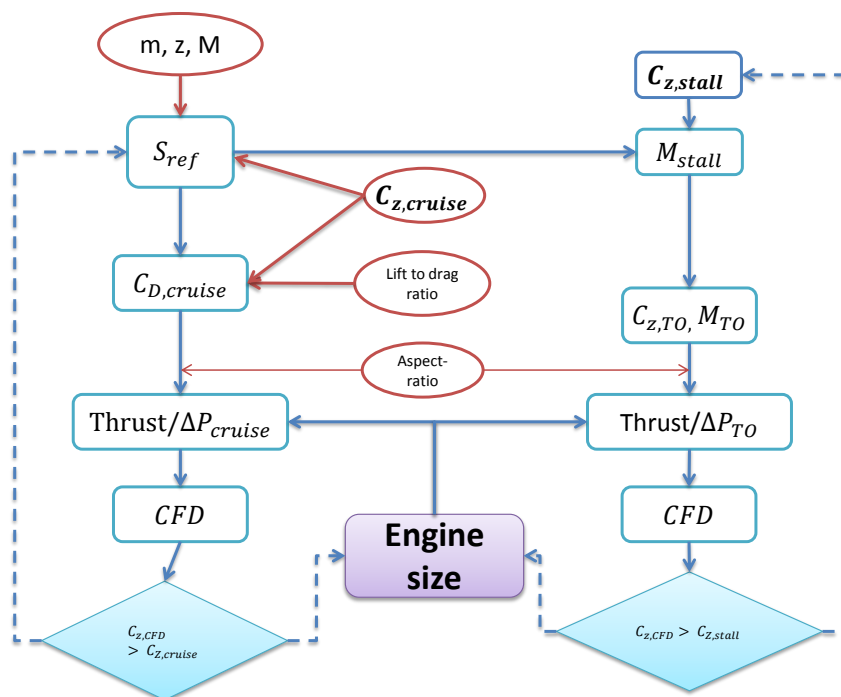
Figure 64: Simplified model for the preliminary design of an aircraft. Red circles: input data

($v_{TO} = 1.2 v_{stall}$). Given take-off speed, and the take-off field length, the acceleration needed to take-off is estimated (basic law of kinematics). For TOFL=1Km, the acceleration is $a = 2.45 m/s^2$. Finally the ΔP needed for take off is given by:

$$\Delta P_{TO} = \frac{m \cdot a}{A} \simeq 50000 Pa \simeq FPR = 1.15 \text{ for a diameter d of 4 cm (first configuration)}$$

(53)

(For ATR propellers, being the diameter d=4m, it yields$\Delta P_{TO} \simeq 1600 Pa$). Considering those values it is clear that the trailing edge configuration (described in section 3.3 on page 21) could not satisfy the requirements given in this section. To obtain a reasonable value (according to figure 6 on page 11), it is immediately necessary to change the diameter to triple the diameter and obtain $\Delta P \simeq 15000 Pa$, i.e. $FPR \simeq 1.15$. This configuration so derived is presented in section 3.5 on page 24. The next step in the design process, following 64, should be the comparison between the maximum lift coefficient obtained from CFD calculations and the maximum lift coefficient that we supposed in the first iteration. If we get a higher $C_{l_{max}}$ than the one we had supposed, the take-off speed would be lower, also the acceleration and the force requested to the propulsive system would be lower, therefore it could be possible to modify the engine accordingly to answer to requirements and to respect cruise configuration calculation.

BIBLIOGRAPHY

Boniface, Jean Christophe
2001 *CHANCE project - Improvement of the actuator disc modeling in the elsA software*, tech. rep. RT 52/01801, Onera DAAP/DSNA.

Drela, Mark
2009 "Power Balance in Aerodynamic Flows", in Fluid Dynamics and Colocated Conferences, American Institute of Aeronautics and Astronautics, http://dx.doi.org/10.2514/6.2009-3762. (Cited on p. 4.)

elsa Theoretical Manual 2007 (ed.), version 3.2.

Felder, James L., Gerald V. Brown, Hyun. DaeKim, and Julio Chu
2011 "Turboelectric Distributed Propulsion in a Hybrid Wing Body Aircraft", in *20th International Society for Airbreathing Engines (ISABE 2011)*, NASA Glenn Research Center.

Felder, James L., Huyn Dae Kim, Gerald V. Brown, and Julio Chu
2011 "An Examination of the Effect of Boundary Layer Ingestion on Turboelectric Distributed Propulsion Systems", in *49th Aerospace Sciences Meetings*, American Institute of Aeronautics and Astronautics. (Cited on p. 6.)

Gibson, Andrew, David Hall, Mark Waters, Philippe Masson, Benjamin Schiltgen, Trevor Foster, and Jonathan Keith
2010 "The Potential and Challenge of TurboElectric Propulsion for Subsonic Transport Aircraft", in *Aerospace Sciences Meetings*, American Institute of Aeronautics and Astronautics.

Hall, Cesare A. and Daniel Crichton
2005 "Engine And Installation Configurations for a Silent Aircraft", in *17th International Society for Airbreathing Engines (ISABE 2005)*, Cambridge University. (Cited on p. 5.)

Kawai, Ronald T., Douglas M. Friedman, and Leonel Serrano
2006 *Blended wing body (BWB) Boundary Layer Ingestion (BLI) Inlet Configuration and System Studies*, NASA.

Kim, Hyoungjin and Meng-Sing Liou
2013 "Optimal Shape Design of Mail-Slot Nacelle on N3-X Hybrid Wing Body Configuration", in *Fluid Dynamics and Co-located Conferences*, American Institute of Aeronautics and Astronautics.

Kim, Hyun Dae
2010 "Distributed propulsion vehicles", in *27th International Congress of the Aeronautical Science*. (Cited on pp. 1, 2, 5.)

Leifsson, L., A. Ko, W.H. Mason, J.A. Schetz, B. Grossman, and R.T. Haftka

2013 "Multidisciplinary design optimization of blended-wing-body transport aircraft with distributed propulsion", *Aerospace Science and Technology*, 25, 1, pp. 16-28, ISSN: 1270-9638.

Pandya, Shishir A., Alejandra Uranga, Alejandro Espitia, and Arthur Huang

2014 , in AIAA SciTech, American Institute of Aeronautics and Astronautics, chap. Computational Assessment of the Boundary Layer Ingesting Nacelle Design of the D8 Aircraft, http://dx.doi.org/10.2514/6.2014-0907.

Schetz, Joseph A., Serhat Hosder, Vance Dippold III, and Jessica Walker

2010 "Propulsion and aerodynamic performance evaluation of jet-wing distributed propulsion", *Aerospace Science and Technology*, 14, 1, pp. 1-10, ISSN: 1270-9638.

Seitz, Arne and Corin Gologan

2013 "Parametric Design Studies for Propulsive Fuselage Aircraft Concepts", in *4th CEAS Air & Space Conference*.

Steiner, Hans-Jörg, Arne Seitz, Kerstin Wieczorek, and Kay Plötner

2012 "Multi-disciplinary deisgn and feasibility study of distributed propulsion systems", in *28th International Congress of the Aeronautical Science*. (Cited on pp. 4, 5, 12.)

Uranga, Alejandra, Mark Drela, Edward Greitzer, Neil Titchener, Michael Lieu, Nina Siu, Arthur Huang, Gregory M. Gatlin, and Judith Hannon

2014 , in AIAA SciTech, American Institute of Aeronautics and Astronautics, chap. Preliminary Experimental Assessment of the Boundary Layer Ingestion Benefit for the D8 Aircraft, http://dx.doi.org/10.2514/6.2014-0906.

Wakayama, Sean R.

2014 , in AIAA SciTech, American Institute of Aeronautics and Astronautics, chap. Revolutionary Configurations for Energy Efficiency, http://dx.doi.org/10.2514/6.2014-1286.